Study of the effects of geometrical parameters of a spiral corrugated convective tube on the heat transfer rate

by
Elianne Schmittinger

Thesis presented in partial fulfilment of the requirements for the degree of Master of Engineering (Mechanical) in the Faculty of Engineering at Stellenbosch University

Supervisor: Prof C Meyer

March 2017

Declaration

By submitting this thesis electronically, I declare that the entirety of the work contained therein is my own, original work, that I am the sole author thereof (save to the extent explicitly otherwise stated), that reproduction and publication thereof by Stellenbosch University will not infringe any third party rights and that I have not previously in its entirety or in part submitted it for obtaining any qualification.

Date: March 2017

Abstract

The single start spiral indentation heat transfer enhancement technique is investigated on a boiler convective tube. It improves the heat transfer rate and increases the pressure drop significantly. This increases the thermal efficiency of the boiler and leads to reduced fuel costs.

Current empirical correlations for calculating the heat transfer rate of the spiral tube require correction factors in order to obtain accurate results. A CFD model is constructed to eliminate the need of a correction factor and to investigate the effects that the geometrical parameters of the spiral indentation have on the heat transfer rate and pressure drop.

The fluid flow characteristics in the CFD model reflect what is expected from theory where higher fluid velocities cause boundary layer thinning and increased pressure drag.

The spiral depth is increased to 2.8 mm. The heat transfer rate increases by an average of 1.4 % and the pressure drop by 31.7 %. The increased spiral depth promotes secondary swirl flow inside the tube, increasing the pressure drag over the indentations and thinning the boundary layer at the wall.

The spiral pitch is decreased to 20 mm and it is found that the pressure drop increases by an average of 5.9 % and the heat transfer rate by 0.3 %. The CFD model results show that a pulse like flow is promoted down the length of the convective tube.

This pulse like flow increases the heat transfer rate and pressure drop over the tube length. It is the result of interference between the indentations in the separation and reattachment zone of the boundary layer.

The spiral pitch is decreased to 22 mm and the depth is increased to 2.4 mm. The heat transfer rate increases by an average of 0.7 % and the pressure drop by 24.0 %. At higher inlet velocity conditions the pulse like flow is promoted again. It is deduced that at the right combination of spiral depth, pitch and fluid velocity, the pulse like flow is promoted.

The spiral pitch-to-depth ratio is investigated and it is found that at ratios below 10, the pressure drop and Nusselt number increases drastically. As the ratio increases beyond 14, the pressure drop and Nusselt number decreases gradually.

It is recommended that the spiral depth of the current spiral tube be increased to 2.4 mm to achieve a spiral pitch-to-depth ratio of 10. This will improve the heat transfer rate by an average of 1.0 % at an acceptable increased pressure drop of an average of 20.7 %.

It is concluded that by changing the geometrical parameters the heat transfer rate is improved and can be used to improve the thermal efficiency of a firetube boiler.

Opsomming

Die tegniek om die warmteoordrag van 'n ketel-konveksiebuis te verhoog deur die aanbring van 'n enkel-begin, spiraal-indentasie word ondersoek. Dit verbeter die warmteoordrag maar verhoog die drukval aansienlik. Die termiese rendement van die ketel word verhoog en dit lei tot 'n vermindering in brandstofkoste.

Huidige numeriese korrelasies vir die berekening van die warmteoordrag van die spiraal-buis gebruik korreksie-faktore wat meer akkurate resultate verseker. ‘n Berekenings-Vloei-Meganika (BVM) model is geskep om die gebruik van die korreksie-faktor te elimineer en om die gevolge van verskillende geometriese parameters van die spiraal-indentasie op die warmteoordrag-tempo en drukval van die buis te ondersoek.

Die vloei-eienskappe in die BVM-model weerspieël die teoretiese verwagting waar hoër vloei-snelhede die grenslaag verdun en die drukval verhoog.

Die spiraal diepte is vermeerder tot 2.8 mm. Die warmteoordrag-tempo verhoog met 'n gemiddeld van 1.4 % en die drukval met 31.7 %. Die verhoogde spiraal-diepte bevorder sekondêre vorteks-vloei binne die buis. Dit verhoog die druk-afhanklike sleurkrag oor die indentasies en verdun die grenslaag aan die wand.

Die spiraal-spasiëring is verminder na 20 mm en daarword bevind dat die drukval verhoog met 'n gemiddeld van 5.9 % en die warmteoordrag-tempo met 'n gemiddeld van 0.3 %. Die resultate van die BVM-model dui daarop dat die vloei pulseer in die lengte van die konveksie-buis. Hierdie pulserende vloei verhoog die warmteoordrag-tempo en drukval oor die buis. Dit is die gevolg van die interaksie tussen die indentasies in die skeiding- en vashegtingsone van die grenslaag.

Die spiraal-spasiëring is verminder na 22 mm en die diepte verhoog tot 2.4 mm. Die warmteoordrag-tempo verhoog met 'n gemiddeld van 0.7 % en die drukval met 24.0 %. Met hoër inlaat-snelhede word die pulserende vloei verder bevorder wat daarop dui dat met die regte kombinasie van spiraal-diepte, spasiëring en vloeistof-snelheid die pulserende vloei bevorder kan word.

Die spiraal-spasiëring tot diepte-verhouding is ondersoek. Die resultate dui daarop dat met ‘n waarde van minder as 10 die drukval en Nusselt-getal drasties verhoog. Met verhogings bo 14, verminder die drukval en Nusselt-getal geleidelik.

Dit word aanbeveel dat die spiraal-diepte van die huidige spiraal-buis verhoog word tot 2.4 mm om 'n spiraal-spasiëring tot diepte-verhouding van 10 te verkry. Dit sal die warmteoordrag-tempo met 'n gemiddeld van 1.0 % verhoog met 'n aanvaarbare drukval verhoging van om en by 20.7 %.

Die gevolgtrekking is dus dat die warmteoordrag-tempo verhoog kan word deur die verandering van die geometriese parameters om sodoende die termiese rendement van 'n ketel te verbeter.

Acknowledgements

The author would like to thank John Thompson for the opportunity to do this Master's degree.

Table of contents

List of figures

List of tables

Nomenclature

A	Heat transfer surface area [m^2]
A_ε	Constant for blending function
C_f	Local skin friction coefficient
C_μ	Variable for turbulent viscosity for realizable k-ε model
C_1	Constant for turbulence transport equations
$C_{1\varepsilon}$	Constant for turbulence dissipation
C_2	Constant for turbulence transport equations
$C_{3\varepsilon}$	Constant for turbulence dissipation
c_p	Specific heat [J/(kg K)]
d	Inside diameter of tube [mm]
d_m	Mean diameter of spiral corrugation [mm]
e	Corrugation depth [mm]
f	Friction coefficient
G_b	Generation of turbulence kinetic energy due to buoyancy [kg/(m s^3)]
G_k	Generation of turbulence kinetic energy due to mean velocity gradients [kg/(m s^3)]
h_f	Frictional head loss [m]
h_g	Heat transfer coefficient of gas [W/(m^2 K)]
h_l	Heat transfer coefficient of water [W/(m^2 K)]
I	Turbulence intensity [%]
I_{in}	Inlet turbulence intensity [%]
I_{out}	Outlet turbulence intensity [%]
k	Instantaneous value of turbulent kinetic energy [m^2/s^2]
k_{air}	Thermal conductivity of air [W/(m K)]
k_t	Thermal conductivity of tube wall [W/(m K)]
L	Tube length [mm]
l_ε	Length scale for turbulence dissipation rate [m]
l_μ	Length scale for turbulent viscosity in viscous sublayer [m]
N	Number of spiral turns
Nu	Nusselt number
P	Pressure [Pa]
Pr	Prandtl number
Pr_t	Turbulent Prandtl number
p	Corrugation pitch [mm]
Q	Heat transfer rate [W]
Re	Reynolds number
Re_{in}	Inlet Reynolds number
Re_{out}	Outlet Reynolds number
Re_t	Turbulent Reynolds number
r	Radial distance in cylindrical coordinates [mm]
r_s	Inside radius of tube [mm]
$\vec{r}$	Position vector at field point
$\overrightarrow{r_w}$	Position vector of the wall boundary
S	Constant for strain equation
S_{ij}	Strain rate tensors
S_k	Source term for turbulent kinetic energy [kg/(m s^3)]

S_ε	Source term for turbulence dissipation rate [kg/(m s^4)]
St	Stanton number
T	Temperature [K]
T_g	Gas temperature [K]
T_{in}	Inlet temperature [K]
T_l	Water temperature [K]
T_{out}	Outlet temperature [K]
T_w	Wall temperature [K]
t_s	Wall thickness of tube[mm]
U	Overall heat transfer coefficient [W/(m^2 K)]
u	Velocity component [m/s]
u^+	Non-dimensional velocity in wall coordinates
u^+_{lam}	Non-dimensional velocity for viscous sublayer
u^+_{turb}	Non-dimensional velocity for fully turbulent region
u_{in}	Inlet velocity [m/s]
u_j	Generalized velocity in tensor notation
u_{out}	Outlet velocity [m/s]
u_τ	Shear velocity [m/s]
u_∞	Velocity in the free stream [m/s]
v	Kinematic viscosity [m^2/s]
x	Entry length [mm]
x_j	Generalized coordinate in tensor notation
Y_M	Contribution of the fluctuating dilatation in compressible turbulence to the overall dissipation rate [kg/(m s^3)]
y	Distance normal to wall in boundary layer [mm]
y	First layer thickness [mm]
y^+	Non-dimensional distance from wall in wall coordinates
$\left(\frac{p}{e}\right)$	Spiral pitch-to-depth ratio
$\left(\frac{x}{d}\right)_{entry}$	Entry length ratio

Greek letters

α	Molecular thermal diffusivity [m^2/s]
β	Corrugation helical angle [°]
Γ	Blending function for non-dimensional velocity
ΔP	Pressure difference/drop [Pa]
ΔRe_t	Turbulent Reynolds number difference
ΔT	Temperature difference [K]
ΔT_m	Mean temperature difference [K]
δ	Spiral correction factor
ε	Turbulence dissipation rate [m^2/s^3]
ε_H	Eddy diffusivity for heat transfer [m^2/s]
ε_M	Eddy diffusivity for momentum transfer [m^2/s]
ξ_{Nu}	Relative deviation on Nusselt number [%]
ξ_P	Relative deviation on pressure [%]
ξ_T	Relative deviation on temperature [%]
κ	Von Kármán mixing length constant

λ_ε	Blending function for turbulent viscosity
μ	Dynamic viscosity [kg/(m s)]
μ_t	Eddy or turbulent viscosity [kg/(m s)]
$\mu_{t,enhanced}$	Turbulent viscosity with blending function [kg/(m s)]
$\mu_{t,viscous}$	Turbulent viscosity in the viscous sublayer for 2 layer approach [kg/(m s)]
ρ	Density [kg/m^3]
σ_k	Schmidt number for diffusion of turbulence kinetic energy
σ_ε	Schmidt number for diffusion of turbulence dissipation
τ_s	Wall shear stress [N/m^2]

1. Introduction

Boilers, and the industrial use of the steam produced by them, has been the norm in the manufacturing industry since the Industrial Revolution in Europe in the 18th and 19th centuries. Steam is utilised in both the saturated and superheated ranges, depending on the process requirement.

Saturated steam is utilised in most textile, food and beverage plants for the mass production of commodities. This means that almost all processed foods and general household items have required the usage of steam, in some or other form, during their fabrication.

In South Africa, saturated steam is also readily used in public works sectors such as prisons and hospitals. It is used in areas such as the kitchens for cooking, in the laundries, and for space and water heating.

Other key industries in South Africa that utilise steam include the sugar, pulp and paper, and oil and gas industries. Dry, high temperature steam is required for their processes and therefore superheated steam is utilised. Superheated steam is also used to drive turbines to generate South Africa's electricity base load.

South Africa as a whole is predominantly dependent on the manufacturing industry where the industry was one of the main contributors to the 3.3 percent GDP growth rate obtained in the second quarter of 2016 (Trading Economics, 2016). One can therefore conclude that without steam, the current industrial infrastructure in South Africa would collapse.

The production of the usable steam however does not come at a clean and cheap price. Increasing fuel costs and the awareness of the environmental impact of burning fossil fuels has increased the demand for more efficient, low emissions boilers. This has driven a change in the approach to designing boilers, emphasizing the improvement of the thermal efficiency and flue gas cleaning systems.

To fully understand how improvements can be made to the steam generation process, the basic fundamentals of a boiler must be understood. A boiler can be described as a vessel that is partially filled with water as shown in Figure 1. Heat is added to the water by means of burning a fuel. The water temperature increases until it reaches the saturation temperature associated with the pressure inside the vessel.

The water evaporates to form steam which then fills the remaining space inside the vessel. When further heat is added the saturated steam will form superheated steam. Water is continually added to the vessel at the same rate the steam is drawn off. This mass balance ensures that the water level inside the boiler remains constant.

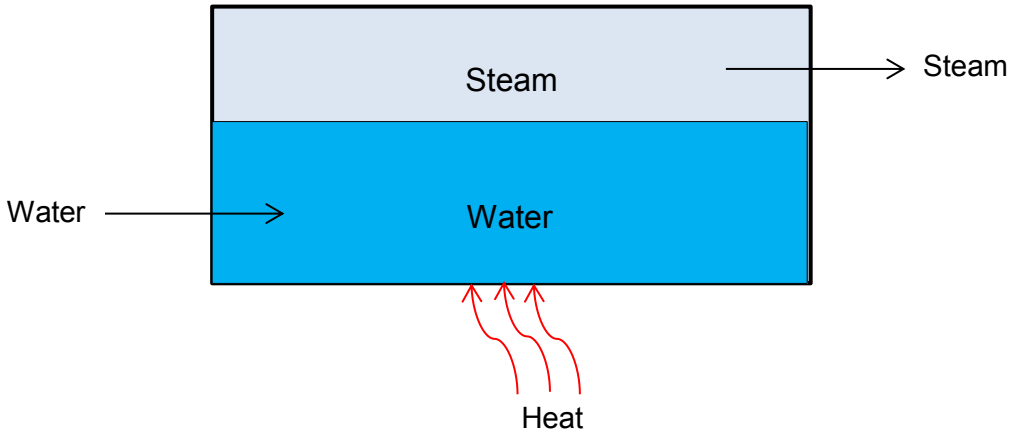

Figure 1: Block diagram of a boiler

Boiler designs can be broken into two main categories namely firetube and watertube boilers. Firetube boilers are predominantly used for the production of saturated steam and watertube boilers typically produce superheated steam.

Watertube boilers, as the name suggests, have tubes filled with water that are heated by the combustion gasses that pass over the outside of the tubes. Firetube boilers on the other hand, have tubes submersed inside the water. The hot combustion gasses pass through the tubes and heat the surrounding water. These two concepts are shown in Figure 2.

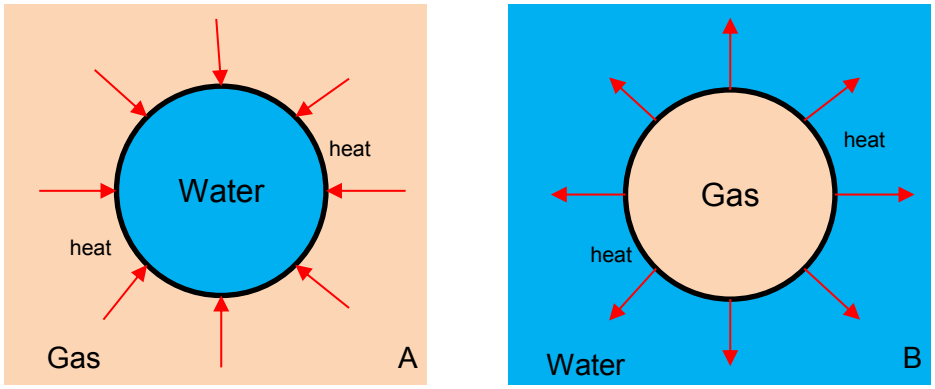

Figure 2: A – Watertube heat transfer diagram. B – Firetube heat transfer diagram

Due to this fundamental difference between the two boiler designs, different approaches are required when conducting design changes to improve the thermal efficiency of the boiler. The focus of this dissertation will therefore only be on improving the thermal efficiency of the firetube boiler design.

The thermal efficiency of the boiler is a measure of how effectively the energy released from burning a fuel is transferred to the water to produce steam. This transfer of energy is expressed by means of the heat transfer rate.

Thermal efficiency should not be confused with boiler efficiency which is affected by the blowdown rates due to water quality, re-stabilisation of the boiler due to fluctuating plant loads and general operation of the boiler.

As the thermal efficiency of the boiler increases so the fuel required to produce the same amount of steam decreases resulting in lower fuel costs. Reducing the running expenses of any company is vitally important and therefore techniques must be investigated to increase the heat transfer rate of the boiler. These techniques are more commonly known as heat transfer enhancement techniques.

The firetube boiler design has been changed significantly over the years. What was once a large heated vessel filled with water became a complex heat exchanger with the introduction of convective tubes inside the boiler vessel in the late 1820s.

Since then additional changes have been made to the design to improve the thermal efficiency. However, with each change the design complexity and cost increased. Difficulty in manufacturing and excessive additional costs reduces the feasibility of some heat transfer enhancement techniques and therefore care should be taken when thermal efficiency design improvements are implemented.

In a firetube boiler approximately 52 % of the heat transfer occurs in the convective tubes. It is therefore feasible to investigate the use of heat transfer enhancement techniques in this area. Currently, various heat transfer enhancement techniques for convective tubes exist. In Chapter 2 these techniques will be discussed and the use of a single start spiral corrugation will be investigated.

The first objective of this thesis will be to determine what effect the heat transfer enhancement technique has on the heat transfer rate and pressure drop across the convective tube length. This is investigated in Chapter 3 by comparing current empirical correlations for plain and spiral tubes.

In addition to this it will be investigated what effects the geometrical parameters of the spiral corrugation have on the heat transfer rate and pressure drop across the tube length. This will be done by constructing CFD models for various spiral pitches and depths.

In Chapter 4 the CFD model will be validated against test results. Chapter 5 will investigate the effect the spiral pitch and depth have on the flow and thereby determine if these changes would result in a feasible option to improve the thermal efficiency of a firetube boiler.

2. Literature review

2.1. John Thompson packaged boiler

The John Thompson packaged boiler is a horizontal three pass wetback firetube boiler. It is used to heat water to produce saturated steam which is utilized in processes such as brewing, packaging, cooking and heating.

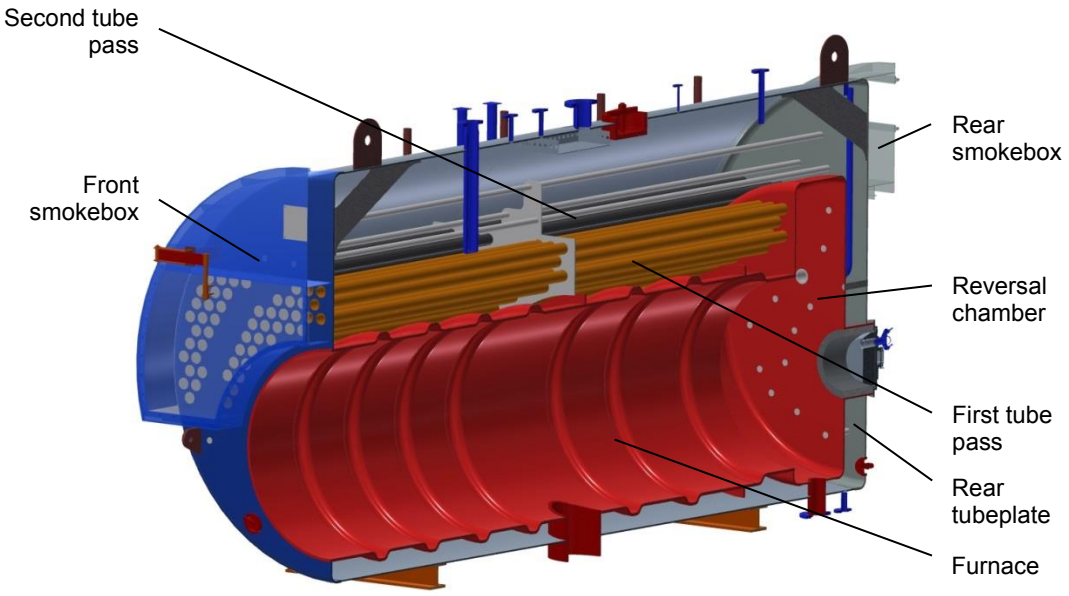

Figure 3: Section through a typical three pass firetube boiler

The boiler has a horizontal cylindrical shell that contains a furnace, a reversal chamber and two sets of tube passes as shown in Figure 3. The lower portion of the shell is filled with water with a normal operating water level that ensures the furnace, reversal chamber and tube passes are submerged in the water. In the upper section of the boiler shell is the steam space which contains the saturated steam produced from heating the water.

This boiler is a wetback boiler which means the whole inside surface of the rear tubeplate is in contact with the water.

The first pass of the boiler is the furnace. This is where the combustion of the fuel occurs. Carbon based fuels react with oxygen in the air. These exothermic reactions release heat that is then utilized to heat the water inside the boiler.

Oil or gas fired boilers are fitted with a burner. In the case of oil the fuel is atomised before it is mixed with air and ignited inside the furnace. The hot combustion gasses are then blown through the boiler by means of the forced draught (FD) fan on the burner.

Solid fuel fired boilers on the other hand are fitted with a chaingrate stoker onto which either coal or biomass is fed. Air is blown into the stoker and through the fuel bed using an FD fan which is fitted to the side of the stoker. A constant negative pressure is maintained inside the furnace by means of an induced draught (ID) fan fitted on the outlet of the boiler. The FD and ID fans work in tandem to balance the draught through the boiler.

The second and third passes consist of a set of tubes each. The second pass transports the hot combustion gas from the reversal chamber to the front smokebox. The third pass then transports the combustion gas from the front smokebox to the rear smokebox where it then exits the boiler and is released into the atmosphere via the stack.

Forced convective heat transfer occurs in these boiler tube passes where the hot combustion gas inside the tubes heat the surrounding water to produce saturated steam.

Each boiler is rated for a specific saturated steam output at a particular operating pressure. To achieve this output a certain amount of energy is required to heat the water from the inlet feedwater temperature in the compressed liquid region to a saturated vapour at the operating pressure.

2.2. Heat transfer rate

The forced convective heat transfer rate, Q, in a tube as defined by Çengel (2006) in the following equation can be expressed in terms of the overall heat transfer coefficient, U, the heat transfer surface area, A, and the mean temperature difference between the two fluids, ΔT_m.

$$Q = UA\Delta T_m \tag{1}$$

The heat transfer rate of the boiler is dependent on mainly three factors. The first is the temperature differential between the combustion gas inside the tubes and the surrounding water. The higher the differential, the greater the heat transfer rate will be.

The second factor is the heat transfer surface area. The greater the area, the greater the amount of heat transferred to the water. The third factor is the thermal resistance of the fluid boundary layer near the heat transfer surface. The thinner the boundary layer, the higher the heat transfer rate will be.

Due to the nature of operation of a boiler the differential temperature cannot be altered. The enhancement technique must therefore either increase the surface area; reduce the thermal boundary layer thickness or achieve both.

The simplest method is to increase the surface area which can be done by increasing the tube length and/or the number of tubes. Too much additional material however will increase the cost of the boiler and could ultimately reduce

the feasibility of the increased heat transfer rate. Any changes done should therefore minimize additional costs and should take ease of manufacture into consideration.

2.3. Enhancement techniques

There are two types of heat transfer enhancement techniques, namely active and passive techniques. The former uses external power such as surface vibration, electrostatic fields or fluid vibration. Passive techniques on the other hand require no external power and instead use extended surfaces, surface roughness or fluid additives.

Due to the nature of operation of a boiler, the enhancement technique will need to be passive.

Ji et al. (2015) summarized previous research done for various enhancement techniques. These included the addition of twisted tape, coil inserts, internal integral fins, dimpled tubes and corrugated tubes. Combinations of the different enhancement techniques were also investigated. Each method showed an increase in the heat transfer rate and pressure drop at different Reynolds number ranges for various fluids.

Garcia et al. (2012) investigated the use of corrugated tubes, dimpled tubes and wire coils for a Reynolds number range of 20 to 20000. It was concluded that for Reynolds numbers below 200, the use of enhancement techniques did not improve the heat transfer rate. For Reynolds numbers between 200 and 2000 it was established that the use of wire coils would be the most beneficial to improve the heat transfer rate. The use of dimpled and corrugated tubes resulted in the greatest improvement in the heat transfer rate for Reynolds numbers greater than 2000.

Zimparov (2002, 2004a, 2004b) studied the addition of twisted tape inserts into corrugated tubes for single phase flow. It was concluded that the heat transfer rate has the greatest improvement at a corrugation depth, e, to inside diameter, d, ratio of 0.044.

It can be seen that there are many different techniques available, each with their own advantages and disadvantages.

The combustion of coal, biogas and heavy furnace oils result in sooty deposits on the gas side surface areas. This is due to their composition and cannot be prevented. It is therefore important that any indentations in the tube surface are large enough so that they do not clog up easily and result in nullifying any heat transfer improvement that they would have provided.

John Thompson previously used twisted tape inserts as a heat transfer enhancement technique (Sharwood, 2016). These inserts however increase the risk of the tubes becoming blocked more readily as the tape divides the cross sectional flow area into smaller areas.

Additional problems experienced included burning of the tape at the inlet of the first tube pass and difficulty in installation of replacement twisted tape inserts (Sharwood, 2016).

It is therefore decided to use a single start concave spiral corrugation as an enhancement technique for the boiler tubes.

2.4. Single start concave spiral corrugation

Spiral corrugations are defined by the pitch, p, depth, e, helical angle, β, and inside tube diameter, d, of the tube as per Figure 4.

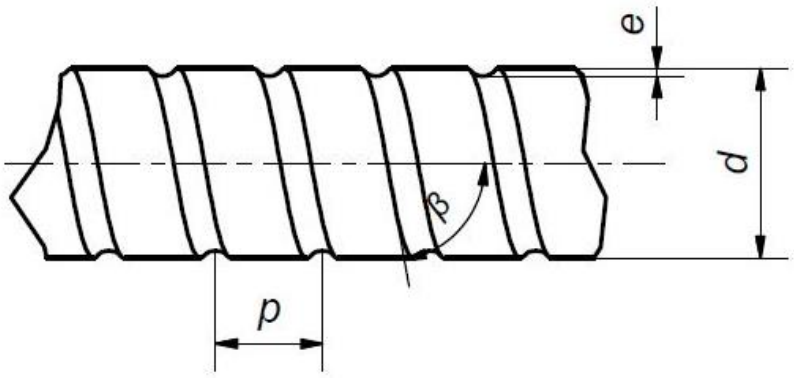

Figure 4: Spiral corrugation geometric parameters

The helical angle is a function of the pitch and the mean diameter of the spiral corrugation, d_m, as defined by Budynas et al. (2008) in Equation 2.

$$\beta = \tan^{-1}\left(\frac{p}{\pi d_m}\right) \tag{2}$$

Various numerical analyses have been done to determine the friction coefficient, Nusselt number and heat transfer coefficient equations for spirally corrugated tubes for single phase flow. Spiral corrugated tubes are often used in heat exchangers and thereby most of the current available numerical models are for liquid flow.

Dong et al. (2001) developed a numerical model to determine the performance of a spirally corrugated tube for water and oil flow for Reynolds numbers ranging from 6000 to 93000, and from 3200 to 19000 respectively.

Pethkool et al. (2011) determined a correlation for the Nusselt number, friction coefficient and efficiency in relation to the pitch-to-diameter and corrugation depth-to-diameter ratios. These equations are valid for water flow for Reynolds numbers ranging from 5500 to 60000.

Vicente et al. (2004) investigated the flow of water and ethylene glycol for Reynolds number ranging from 2000 to 90000 and Prandtl numbers from 2.5 to 100. Expressions for the Nusselt numbers and Fanning friction factor are obtained as functions of the heat transfer roughness and the flow conditions.

Laohalertdecha and Wongwises (2011a, 2011b) presented that the Nusselt number increased with increasing corrugation depth and decreasing corrugation pitch. Ji et al. (2015) stated that corrugated tubes with higher e/d and lower p/d ratios had higher pressure drops.

Kathait and Patil (2014) concluded that the friction factor and Nusselt number increased with decreased p/e ratio below 10. At a ratio greater than 14, both values decreased.

Kays et al. (2005) stated that by ensuring that the protrusion is small enough to be primarily in the sublayer region will prevent the pressure drop from increasing disproportionately to the heat transfer rate. This is called dynamically smooth flow.

This shows that by changing the spiral corrugation characteristics, the most advantageous values can be found for the greatest improvement in the heat transfer rate, but at an acceptable increase in the pressure drop across the tube.

The addition of the spiral also increases the heat transfer surface area of the tube.

2.5. Turbulent pipe flow

To fully understand what effect the spiral corrugation will have on the momentum and heat transfer of the fluid inside the pipe, the characteristics of turbulent fluid flow needs to be understood.

2.5.1. Turbulent boundary layer

The boundary layer for fully developed turbulent pipe flow is divided into three regions, namely, the viscous sublayer, the buffer region and the fully turbulent core as shown in Figure 5.

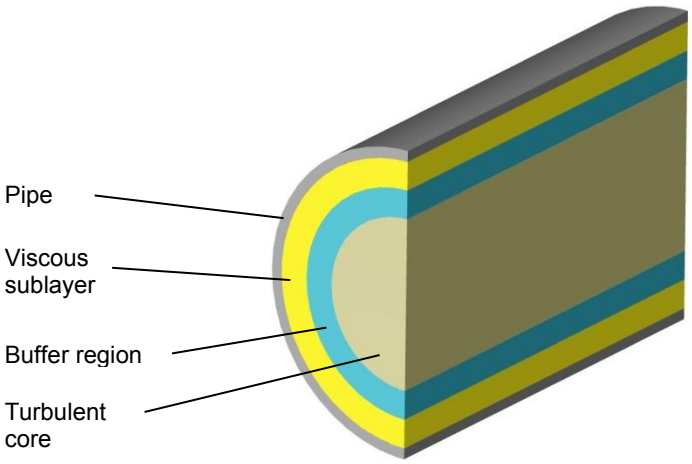

Figure 5: Boundary layer regions for fully developed turbulent pipe flow

In the viscous sublayer the kinematic viscosity, ν, is much larger than the eddy diffusivity for momentum, ε_M. This means that the viscous shear stress, τ_s, dominates over the momentum transfer and thereby dampens out turbulent fluctuations in this region.

Due to the high shear stress the velocity in this region is low compared to the fully turbulent core, with a velocity of zero at the wall for the no-slip condition. The velocity profile for fully developed turbulent flow is fairly flat. The velocity and shear stress profiles across the pipe diameter are shown in Figure 6.

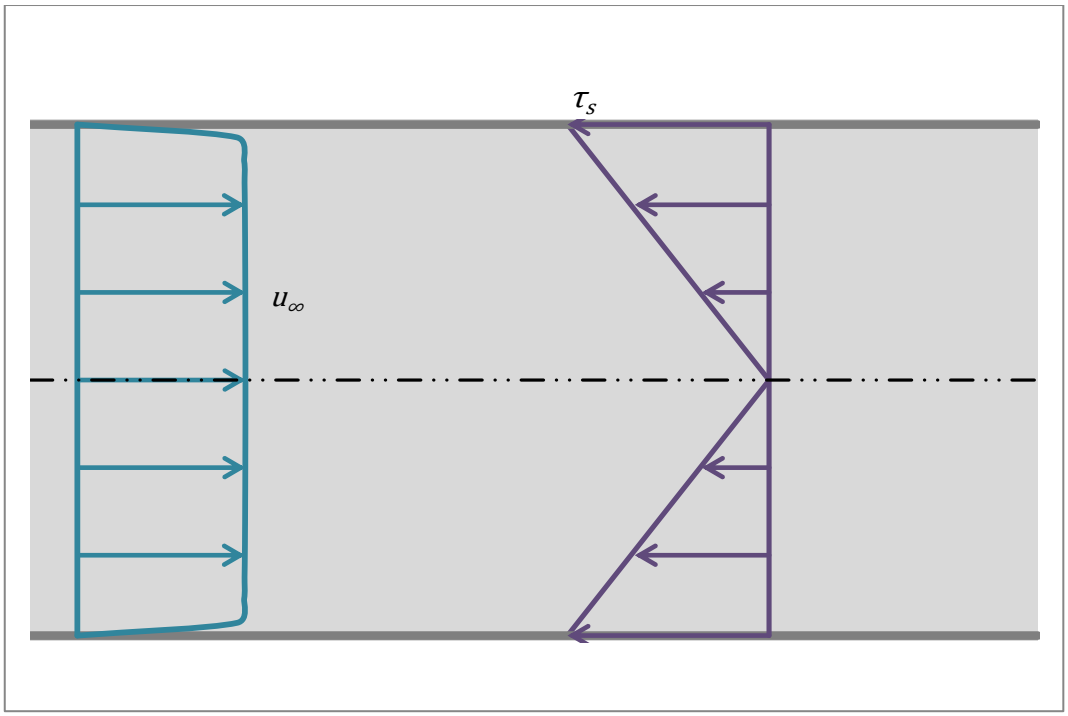

Figure 6: Velocity and shear stress profiles for fully developed turbulent pipe flow

Similarly in the viscous sublayer region the eddy diffusivity for heat transfer, ε_H, is much smaller than the thermal diffusivity, α, which means thermal conductivity is dominant in this region. When referring to heat transfer the viscous sublayer is also known as the conduction sublayer. The temperature profile is similar to the velocity profile and has a fairly flat contour.

In the fully turbulent core the eddy diffusivity for momentum and heat transfer are much greater than the kinematic viscosity and thermal diffusivity, respectively. This means that in this region turbulent fluctuations are promoted.

The buffer region is in between the viscous sublayer and the fully turbulent core. In this region the fluid transfers between the viscous sublayer and the fully turbulent core. This transfer is termed “bursts” in which low-speed fluid near the wall is forcefully ejected into the fully turbulent core and high-speed fluid from the inner fully turbulent region back towards the wall, as discussed by Landahl (1975).

This action is driven by two mechanisms namely the Orr and Lift-up mechanisms. The Orr mechanism originally described by Orr (1907) amplifies the cross-shear velocity when backward leaning vortices are tilted forward by the shear stress until they are normal to the wall surface and dampens it when the vortices tilt past the normal.

The Lift-up mechanism identified by Ellingsen and Palm (1975) on the other hand results in the formation of streamwise-velocity streaks. This is due to the deformation of the mean velocity profile by the cross-shear velocities as discussed by Brandt (2014).

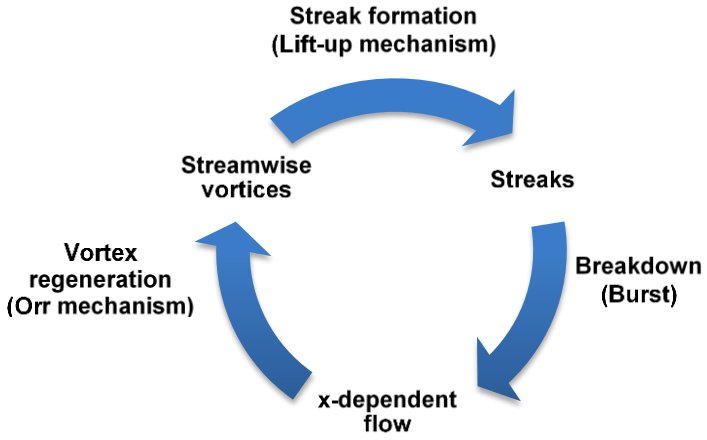

Figure 7: Sketch of the regeneration cycle of wall turbulence (Brandt, 2014)

The combination of the two mechanisms allows for the generation of streaks that grow until instability occurs which in turn allows for the creation of new vortices.

As discussed by Jiménez (2013) damping the vortices dampens the streaks but not vice versa. This is due to the “bursts” obtaining energy directly from the mean shear which allows for the normal velocities of the vortices to be maintained and amplified even when the streak has been dampened. The amplified normal velocities will eventually restart the streak resulting in the regeneration cycle of wall turbulence shown in Figure 7 where the x axis is along the length of the pipe.
.

2.5.2. Flow separation

Flow separation occurs around the spiral indentation similar to what is seen in flow around a cylinder. On the leading edge of the indentation there is favourable pressure gradient where the pressure decreases in the direction of flow. The velocity of the fluid will therefore increase at this point and decrease the viscous sublayer thickness as shown in Figure 8.

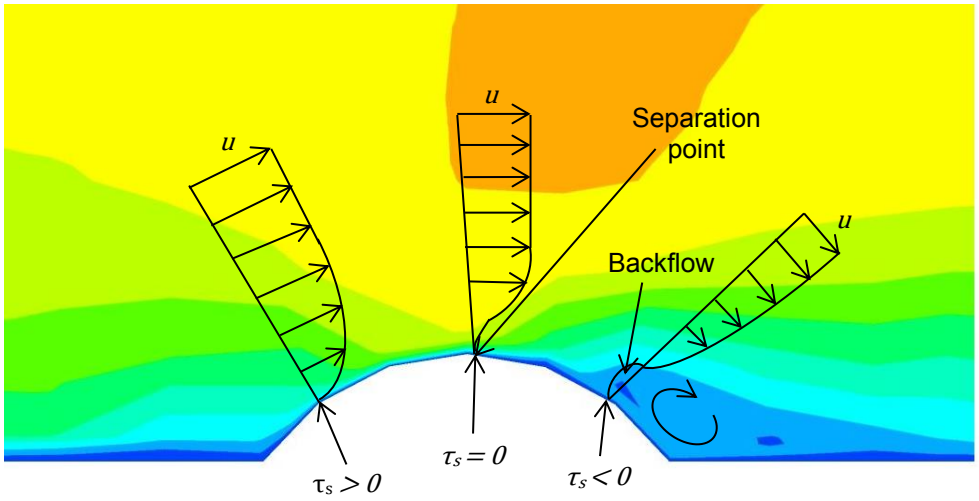

Figure 8: Effect of pressure gradients on the boundary layer velocity profile

On the trailing edge of the indentation an adverse pressure gradient occurs where the pressure increases in the direction of flow. This decreases the velocity of the fluid and increases the boundary layer thickness.

Near the point on the indentation where the wall boundary diverges away from the direction of the mean flow, the boundary layer separates from the wall boundary. This is called the separation point where the viscous shear stress at the wall is zero. Beyond this point the viscous shear stress becomes negative and causes the flow to change direction and recirculate behind the indentation. This recirculated flow is more commonly known as an eddy and has an unsteady strong-shear surface.

The reverse flowing fluid pushes the boundary layer away from the wall resulting in boundary layer separation. The higher velocity fluid moves over the high shear surface of the eddy, which due to its unsteady nature becomes unstable and is broken down shortly after the indentation. This breakdown results in turbulence

which is dampened out again by the viscous shear stress downstream of the indentation. Reattachment of the boundary layer occurs and the fluid flow becomes stable again.

This thinning of the sublayer and high level of turbulence near the wall will allow higher temperature fluid from the fully turbulent core closer to the pipe wall surface and thereby increase the heat transfer rate.

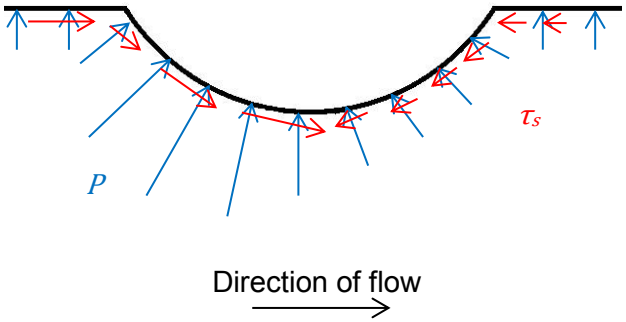

Figure 9: Pressure and viscous shear forces on indentation

The protrusion of the spiral corrugation on the inner surface however also increases the pressure drop along the tube length. As described by MIT OpenCourseWare (2006) there is a local pressure force normal to the wall surface and a viscous shear force tangential to the wall surface.

As described above both forces have an adverse effect on the flow of the fluid around the indentation where the local pressure force is greater on the upstream than the downstream side seen in Figure 9. The resultant local pressure force around the indentation is therefore in the direction of flow and is called the pressure drag of the indentation.

A large increase in the pressure drop across the tube length means that the power rating of the boiler fan motors will need to be increased to be able to overcome the total increased pressure drop across the boiler. This has cost implications and care should be taken with the addition of the spiral corrugation.

3. Empirical correlation

3.1. Spiral corrugated tube

3.1.1. Introduction

A one-dimensional empirical correlation is currently used by John Thompson to determine the temperature and pressure drop across a boiler. With the introduction of the single start concave spiral corrugated tubes, a validation of the formulae below obtained from Warren (2000) for the Stanton number, St, and friction coefficient, f, had to be done. These equations, along with the spiral tube technology, were obtained through a technology transfer (Warren, 2000).

$$St = \frac{\left(\frac{f}{8}\right)^{0.5}}{2.5\ln\left(\frac{d}{2e}\right)+10.77\left(\frac{e}{d}\right)^{0.33}\left(\frac{p}{e}\right)^{0.096}\left[\left(\frac{e}{d}\right)Re\left(\frac{f}{8}\right)^{0.5}\right]^{0.273}Pr^{0.5}-3.75} \quad (3)$$

$$f = \frac{8}{\left[2.5\ln\left(\frac{d}{2e}\right)+0.868\left(\frac{e}{d}\right)^{-0.33}\left(\frac{p}{e}\right)^{0.366}[1+0.0296(\ln(Re)-9.48)^2]exp^{\frac{-0.005p}{e}}-3.75\right]^2} \quad (4)$$

This was achieved through testing done by du Toit (2002) where the pressure and temperature drop across a spiral corrugated test tube was recorded for a Reynolds number range of 3000 to 16000.

These test results were then compared to the empirical results obtained from Equations 3 and 4 and adjustments to the equations were made where required.

3.1.2. Test rig setup

The test rig shown in Figure 10 consisted of 3 sections. The first section, shown in Figure 11, comprised of a fan, an electrical element air heater, a radiation shield and an inlet sealing box which contained a thermocouple and a pressure tapping point.

The air was blown into the test rig via the fan and heated up to 600 °C by the air heater. A radiation shield consisting of two bends was used to prevent radiation error at the inlet temperature thermocouple measuring point. The bends also ensured that the heated air was mixed before entering the spiral tube for equal temperature distribution. Temperature readings were taken with the thermocouple across the pipe diameter to confirm no significant temperature variation was present across the pipe width.

The inlet sealing box of the test rig consisted of a straight length of pipe and a reducer, reducing from the radiation shield diameter to the spiral tube diameter. To ensure the flow at the inlet of the spiral tube is fully developed, the straight length of pipe of the inlet sealing box was made longer than the required length

of $7d$ (Latzko, 1921). This ensured that the condition of the air entering the spiral tube section of the test rig was free from any flow structures caused by the heater or radiation shield.

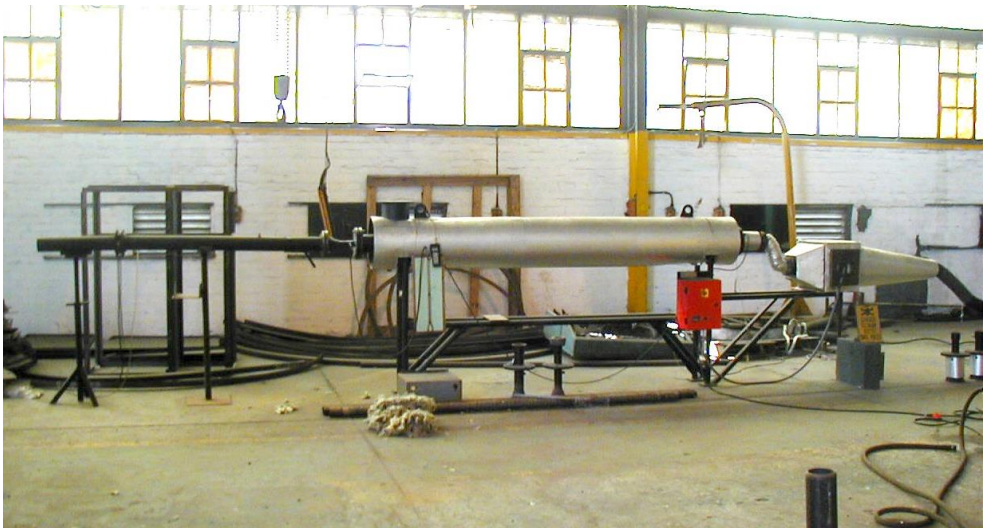

Figure 10: Spiral tube test rig (du Toit, 2002)

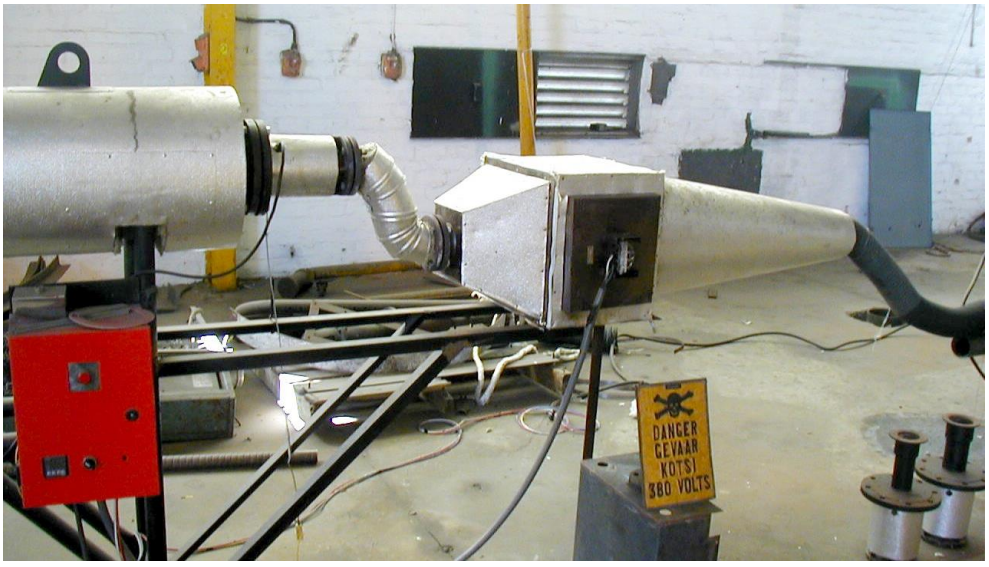

Figure 11: Heater, radiation shield and inlet sealing box (du Toit, 2002)

The second section, shown in Figure 12, consisted of an insulated tank inside which the spiral corrugated tube was fitted. The tank was filled with water and was kept at a constant temperature of 100 °C.

Figure 13 shows the third section which consisted of an outlet sealing box with a thermocouple and a pressure tapping point; a tube bundle flow rectifier and an orifice plate.

Figure 12: Insulated tank with spiral tube inside (du Toit, 2002)

Figure 13: Outlet sealing box, tube bundle flow rectifier and orifice plate (du Toit, 2002)

The air that was heated in the first section was passed through the spiral tube in Section 2. Temperature and pressure readings were taken at the inlet and outlet sealing boxes.

The mass flow rate of the air was measured using the orifice plate, a photohelic pressure cell and a thermocouple. The tube bundle flow rectifier was used to eliminate any swirl of the airflow from the spiral corrugation before the flow measurement was taken at the orifice plate.

3.1.3. Results

Du Toit (2002) found that the empirical results obtained for the pressure drop across the tube length using the friction coefficient from Equation 4 (Warren, 2000) correlated fairly accurately to the results obtained from the experimental test rig. This can be seen in Figure 14 where the pressure drops obtained from the empirical calculations are higher than those obtained from the experimental test rig. An average relative deviation of 12 % was achieved.

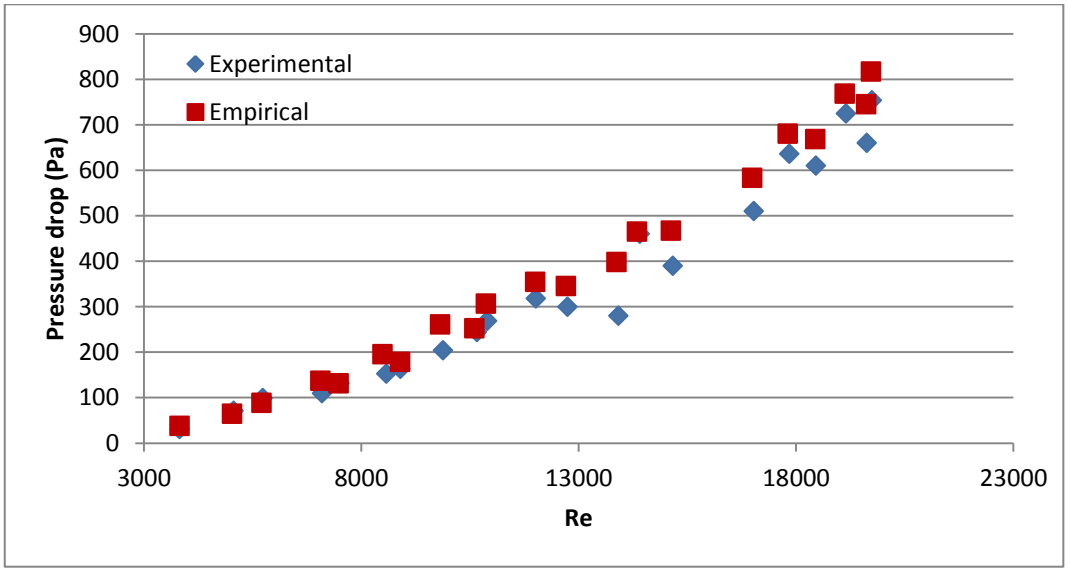

Figure 14: Pressure drop versus Reynolds number for experimental and empirical results

The Nusselt number is calculated using Equation 5 where the Stanton number is calculated using Equation 3 (Warren, 2000).

$$Nu = StPrRe \tag{5}$$

These empirical results for the Nusselt numbers are higher than those obtained from the experimental results with an average relative deviation of 15 %. A correction factor, δ, was added to Equation 5 by du Toit (2002) to adjust the results to suit those obtained from the experimental test setup.

The new equation for the Nusselt number is shown in Equation 6. This is to ensure that fairly accurate results are achieved when doing the one dimensional empirical correlations.

$$Nu = \delta StPrRe \tag{6}$$

The Nusselt number is plotted against the Reynolds number for the experimental results, Equation 5 (Warren, 2000) and Equation 6 (du Toit, 2002) in Figure 15. It can be seen that Equation 6's results, with the correction factor, correlate better with the experimental results than Equation 5's results.

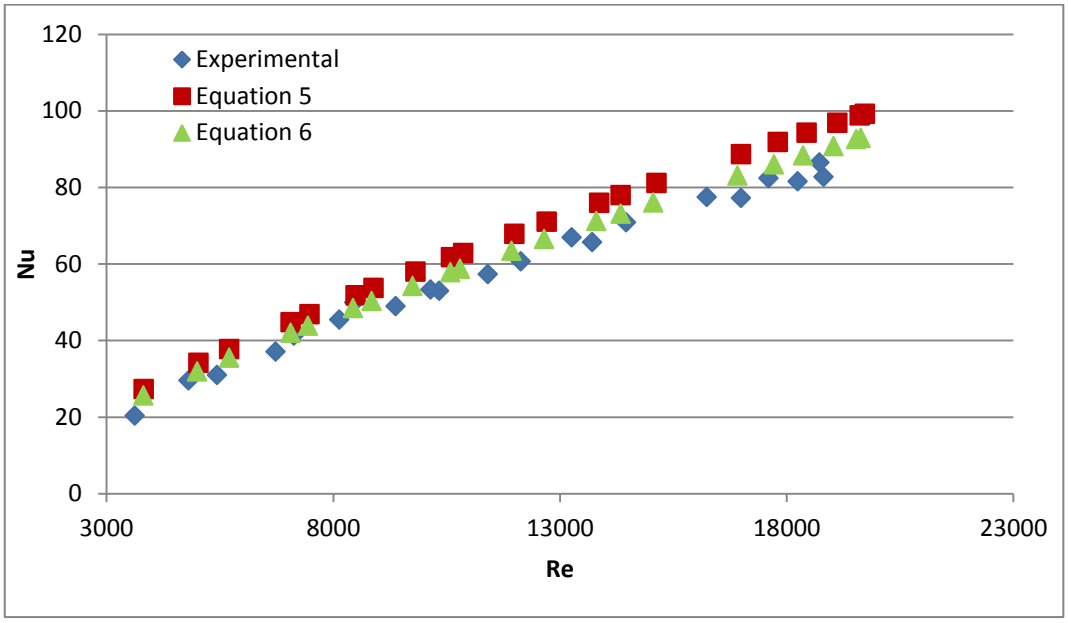

Figure 15: Nusselt number versus Reynolds number for experimental and empirical results

3.2. Plain and spiral corrugated tubes

With the validation of Equations 3 and 4, an empirical comparison can be done of a plain tube versus the new spiral corrugated tube.

The Nusselt number for turbulent flow inside a plain tube is calculated using the following equation. The equation was formulated by Kitto and Stultz (2005) for turbulent gas flow inside smooth tubes for shell boilers.

$$Nu = 0.023Re^{0.785}Pr^{0.45}\left[1 + \left(\frac{d}{L}\right)^{\frac{2}{3}}\right] \tag{7}$$

The Nusselt number is plotted against the Reynolds number for a plain tube and a spiral tube in Figure 16. The spiral tube Nusselt number is calculated using Equation 6 (du Toit, 2002) and the plain using Equation 7 (Kitto and Stultz, 2005).

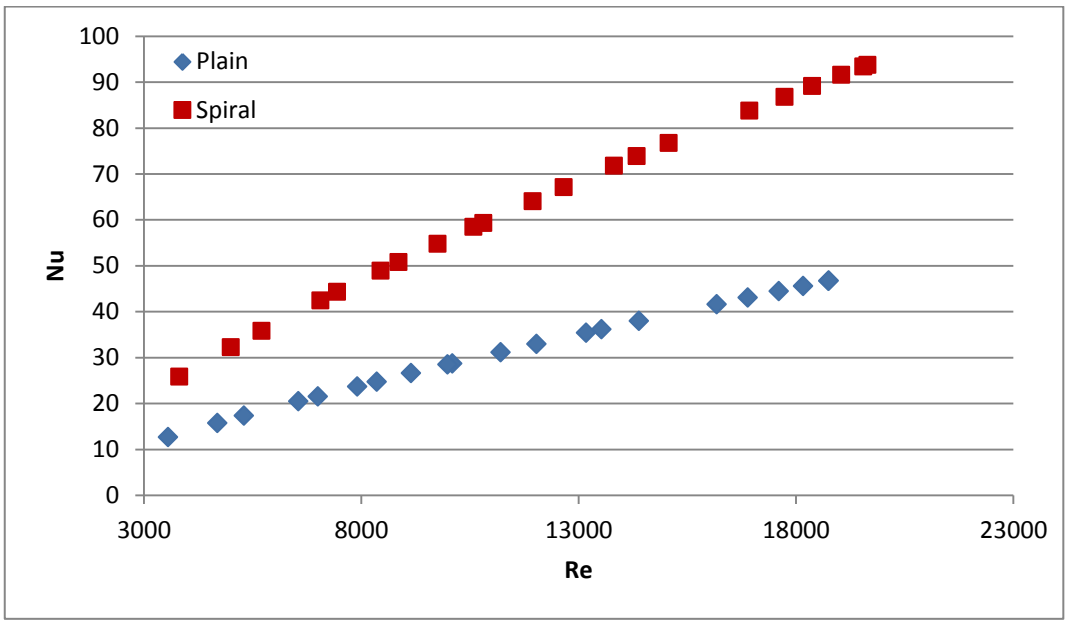

Figure 16: Nusselt number versus Reynolds number for plain and spiral corrugated tubes

As seen in Figure 16 the addition of the spiral corrugation increases the Nusselt number significantly. From the outlet gas temperatures in Table 1 it is seen that a significant amount of additional heat is absorbed along the length of the spiral corrugated tube than in the plain tube.

Table 1: Inlet & outlet gas temperatures for plain and spiral corrugated tubes

Test point	T_{in} K	T_{out} K		ΔT K
		Plain	Spiral	
1	837	490	408	82
2	825	502	413	90
3	817	508	416	92
4	794	506	424	82
5	785	508	427	81
6	764	507	422	85
7	733	497	419	78
8	675	487	415	71
9	649	477	418	60
10	639	475	417	57
11	638	475	418	57
12	803	489	413	76
13	733	481	408	73
14	704	475	408	68
15	682	481	412	69
16	656	472	412	60
17	639	467	411	57
18	631	466	411	55
19	624	466	412	54
20	613	460	410	50
21	606	458	410	49

To calculate the friction factor for the plain tubes, the Blasius equation shown below is used.

$$f = 0.316Re^{-0.25} \tag{8}$$

The friction factor for the spiral tube is calculated using Equation 4 (Warren, 2000).

The pressure drop across the tube length is calculated using Equations 9 and 10 for the 21 inlet flow conditions used in the test rig for the spiral and plain tubes.

$$\Delta P = \rho g h_f \tag{9}$$

$$h_f = f \frac{L}{d} \frac{u^2}{2g} \tag{10}$$

This pressure drop is plotted against the Reynolds number in Figure 17. It is seen that the pressure drop across the tube length increases significantly with the addition of the spiral corrugation.

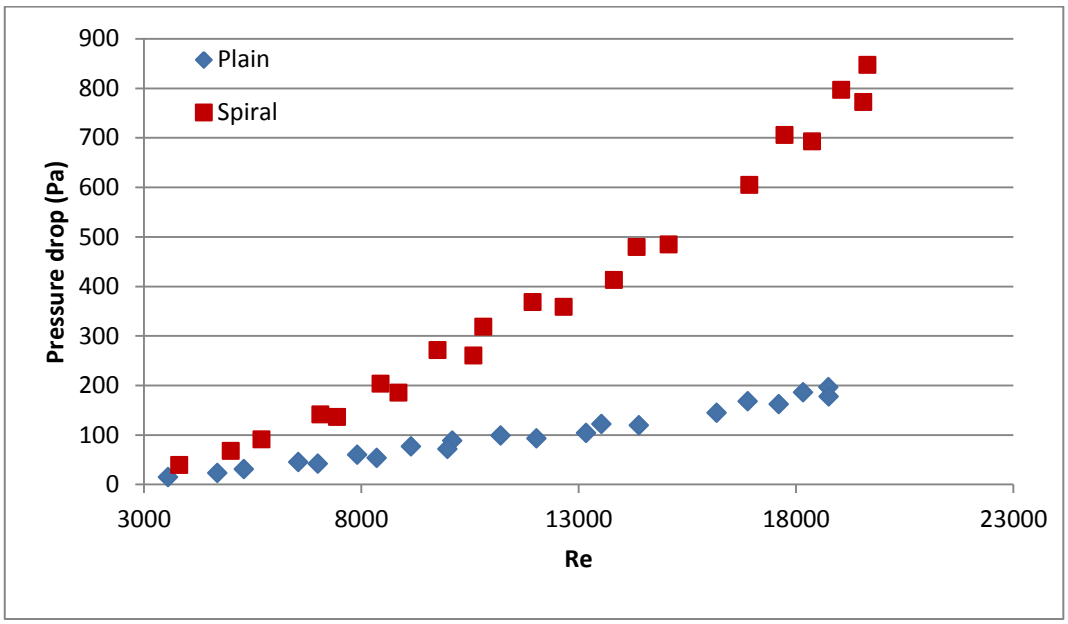

Figure 17: Pressure drop versus Reynolds number for plain and spiral corrugated tubes

3.3. Conclusion

The empirical correlations for the friction coefficient and Nusselt number for the spiral corrugated tube were validated against test results by du Toit (2002). It was found by du Toit (2002) that a correction factor was required for the Nusselt number equation in order to obtain accurate results.

It is however assumed that the correction factor added to the Nusselt equation is valid for all Reynolds numbers across the total temperature range of the combustion gas inside the boiler.

The addition of the spiral corrugation to the plain convective tube improves the heat transfer rate by an average of 104 % and increases the pressure drop by an average of 270 %.

It is therefore concluded that the addition of the spiral corrugation is beneficial and improves the heat transfer rate, however a more accurate means is required to predict the heat transfer rate without the use of a correction factor.

The use of a CFD model can therefore eliminate the requirement of the correction factor which would possibly have to change depending on the pitch, depth and inside tube diameter of the spiral corrugation.

4. CFD model validation

4.1. Introduction

A single start spiral corrugated tube is modelled in FLUENT version 17.0. The geometry of the test tube used in the test rig in Section 3 is used in the model.

In this section a comparison will be done of the experimental results obtained from the test rig in Section 3 and the results from the CFD model.

4.2. Geometry

The dimensions of the spiral tube are as per Figures 18 and 19. To reduce the mesh size only the internal gas side fluid volume is modelled.

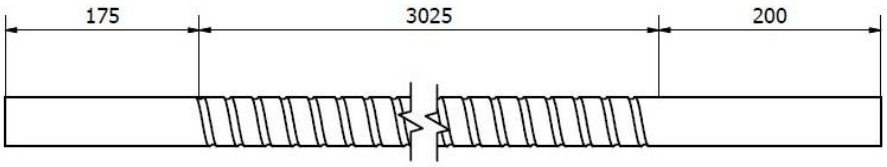

Figure 18: Dimensions of spiral and plain sections of test tube

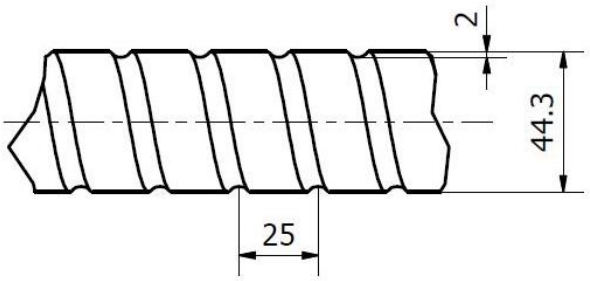

Figure 19: Dimensions of fluid side spiral corrugation geometric parameters

The geometry is sub-divided into twelve bodies with ten of these sweepable. This is not only done for ease of meshing but to also ensure that a good quality mesh can be obtained. A better quality mesh will reduce the number of numerical errors obtained due to mesh inaccuracies.

The better the quality of the mesh is, the more accurate results can be acquired.

Additional settings and dimensions of the geometry can be seen in Appendix A.

4.3. Mesh

The geometry is meshed using the curvature advanced size function. All sweepable bodies are swept using quadrilateral and triangular elements and a tetrahedron mesh is used for the three non-sweepable bodies.

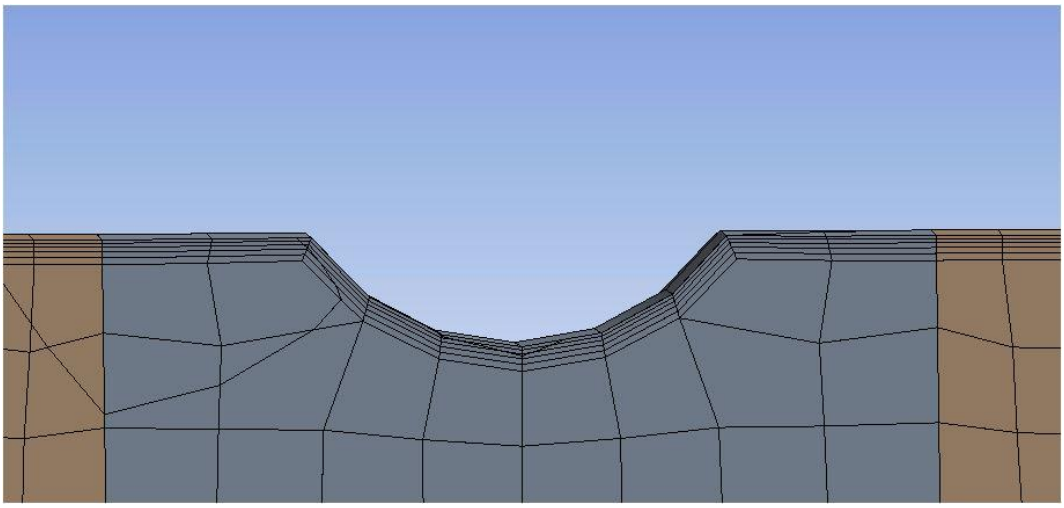

Figure 20: Inflation layer on wall boundary

To ensure that the boundary layers close to the wall are accurately modelled, an inflation layer is added to the wall boundary as shown in Figure 20. The first layer thickness option is used to model this.

The required first layer thickness, y, is determined by the y^+ value desired at the wall by the turbulence near-wall treatment model used in FLUENT. For example, for the enhanced wall treatment model a y^+ value near 1 yields more accurate results.

$$C_f = 0.078Re^{-0.25} \tag{11}$$

$$\tau_s = \frac{C_f}{2}\rho u_\infty^2 \tag{12}$$

$$u_\tau = \sqrt{\frac{\tau_s}{\rho}} \tag{13}$$

$$y = r_s - r = \frac{\mu y^+}{\rho u_\tau} \tag{14}$$

The first layer thickness is calculated using Equations 11 through to 14 where C_f is the skin friction coefficient, τ_s, the wall shear stress and u_τ, the shear velocity.

The skin friction coefficient equation is described by Kays et al (2005) for turbulent internal flow of smooth pipes and gives accurate results for a Reynolds number range of 10000 to 50000.

The required thicknesses for a y^+ value of 1 are calculated for each test condition and an average of 0.06 mm is obtained. It is decided to use a first layer thickness of 0.06 mm for the inflation layer for the enhanced wall treatment.

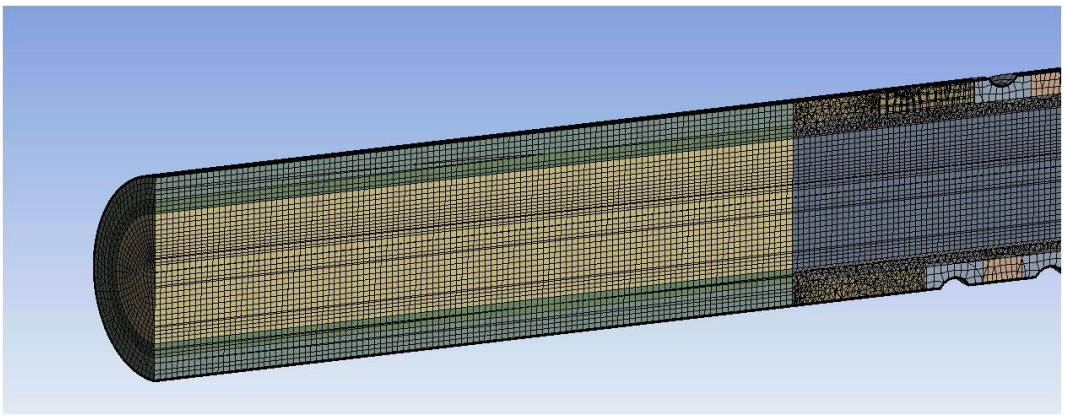

Figure 21: Sectional view of mesh

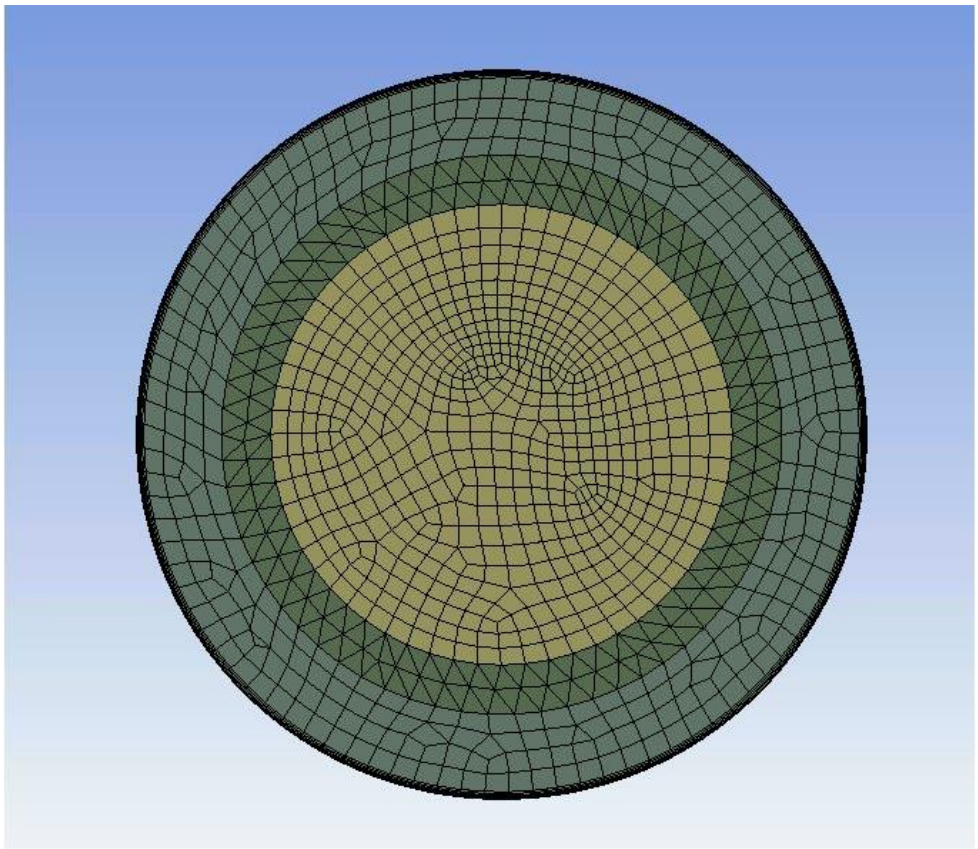

Figure 22: Mesh on Inlet boundary

The final mesh, mesh A, is shown in Figures 21 and 22 with a mesh size of 5 471 249 elements. Due to the size of the spiral corrugation and the first layer thickness, a very fine mesh is obtained.

A second finer mesh is solved to determine what effect a finer mesh will have on the accuracy of the results. The mesh sizing is changed as per Appendix A resulting in mesh B with 7 122 886 elements. Mesh B has thirty percent more cells than mesh A which results in a longer simulation run time.

Simulations are run for seven of the twelve test points to ensure the full inlet velocity range is compared.

The results from mesh A and B are each compared against the experimental results and these relative deviation on pressure, ξ_P and temperature, ξ_T are tabulated in Table 2. From the results for the two meshes it is seen that increasing the mesh size by thirty percent does not yield significantly more accurate results. It can therefore be concluded that the mesh size chosen, mesh A, will ensure fairly accurate results.

Table 2: Mesh refinement results

Test point	u_{in} m/s	T_{in} K	T_{out} K		ΔP Pa		ξ_P %		ξ_T %	
			A	B	A	B	A	B	A	B
1	14.6	764	411	411	309	305	12.8	11.9	0.5	0.4
2	15.2	733	411	411	355	350	10.3	9.0	0.3	0.2
3	16.4	675	410	409	456	460	0.8	0.1	0.1	0.2
4	19.3	649	411	411	663	665	4.0	4.3	0.1	0.1
5	20.3	639	411	411	746	744	2.8	2.5	0.0	0.0
7	12.2	682	403	403	260	258	6.2	5.4	0.4	0.3
8	13.9	656	404	405	353	349	15.0	14.0	0.2	0.1

To ensure that a good quality mesh has been obtained the mesh orthogonal quality and skewness is checked. An average skewness of 0.20 and average orthogonal quality of 0.89 is attained. Elements with high skewness and low orthogonal qualities are found at the start and end of the spiral corrugation.

The spiral corrugation start and end faces, as shown in Figure 23, are sharp and small in size therefore low quality elements in these regions can be expected. However the percentage of these low quality elements is insignificant when compared to the number of high quality elements.

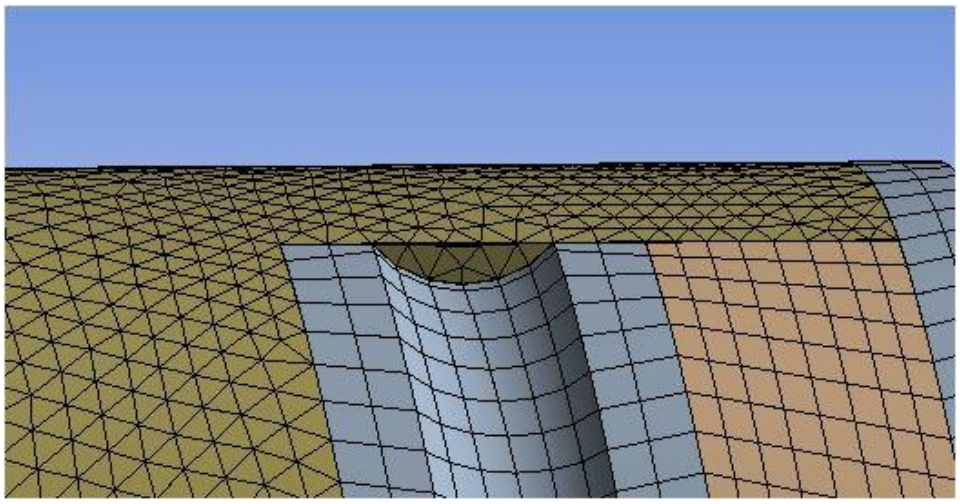

Figure 23: Start of spiral corrugation

All additional settings can be found in Appendix A.

4.4. Boundary conditions

There are three boundary types in this model namely the inlet, outlet and the wall as shown in Figure 24. These boundaries will be specified as per Table 3.

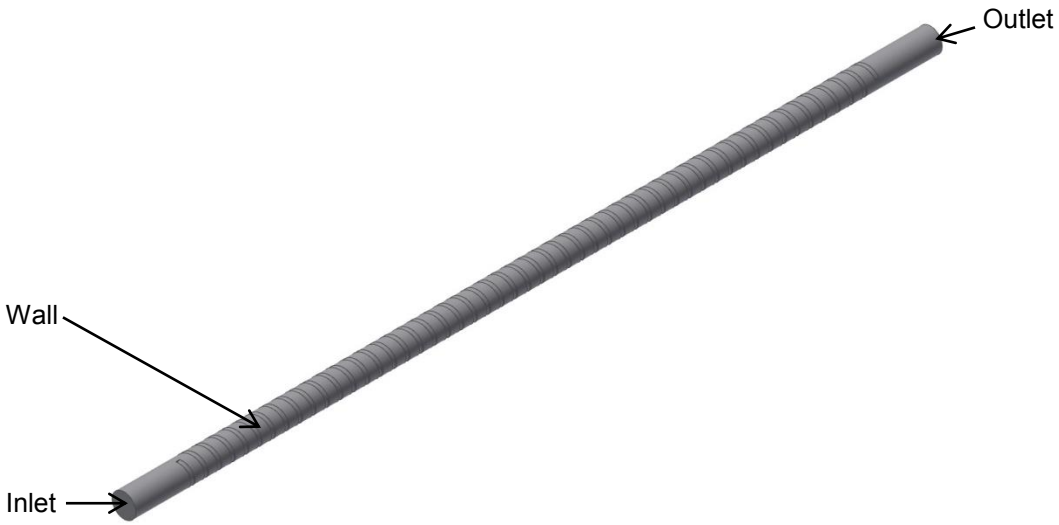

Figure 24: Boundaries of model

Table 3: Boundary types

Boundary	Type
Inlet	Velocity inlet
Outlet	Pressure outlet
Wall	Wall

4.4.1. Inlet

To ensure that the inlet boundary conditions are in the turbulent flow regime the Reynolds number for all the test points are calculated. Twelve of these test points are thereby selected as inlet conditions for the CFD model as shown in Table 4.

Table 4: Inlet boundary conditions

Test point	u_{in} m/s	T_{in} K	Re_{in}	x	I %
1	14.6	764	8783	$6d$	5
2	15.2	733	9818	$6d$	5
3	16.4	675	12097	$7d$	5
4	19.3	649	15207	$7d$	5
5	20.3	639	16411	$7d$	5
6	20.9	638	16948	$7d$	5
7	12.2	682	8867	$6d$	5
8	13.9	656	10756	$6d$	5
9	15.7	631	12967	$7d$	5
10	17.4	624	14636	$7d$	5
11	18.4	613	15959	$7d$	5
12	19.3	606	17042	$7d$	5

Latzko (1921) states that the entry length ratio, $(x/d)_{entry}$, can be calculated using the Reynolds number as shown in Equation 15 below. The maximum entry length, x, calculated is $7d$ for the twelve test points.

$$\left(\frac{x}{d}\right)_{entry} = 0.623Re^{0.25} \tag{15}$$

The straight length of pipe upstream of the spirally corrugated test tube in the test rig is greater than $7d$ as calculated from Equation 15. It can therefore be assumed that the flow at the inlet of the corrugated tube is fully developed.

The Prandtl number is the ratio between the eddy diffusivity for momentum and heat transfer as defined in the following equation. Therefore for fluids with a Prandtl number equal to 1, momentum and heat diffuse through the fluid at the

same rate. This means that the velocity and temperature profiles develop simultaneously.

$$Pr_t = \frac{\epsilon_M}{\epsilon_H} \tag{16}$$

The test fluid, air, has a Prandtl number of less than 1. In this instance the temperature profile develops faster than the velocity profile. It can therefore be assumed that the temperature profile is also fully developed at the inlet of the spirally corrugated tube.

In fully developed turbulent flow the velocity and temperature profiles across the tube are fairly flat. It is therefore assumed that both profiles across the inlet boundary are constant and the velocity is normal to the boundary.

Fully developed internal flow also allows the use of the Intensity and hydraulic diameter turbulence method.

$$I = 0.16Re^{-\frac{1}{8}} \tag{17}$$

An intensity, I, of 5 % is used, as calculated from Equation 17 (Fluent, 2015) and shown in Table 4. This is classified as medium intensity.

4.4.2. Wall

The water surrounding the tube has a much higher heat transfer coefficient than that of the gas flowing through the tube. This allows the assumption that the surface temperature remains constant along the length of the tube.

A thin-wall thermal resistance is used to model the wall thickness of the tube. Using this option will calculate the conduction for the wall in the normal direction only.

$$Thermal\ resistance = \frac{t_s}{k_t} \tag{18}$$

The thermal resistance of the wall is calculated using the wall thickness, t_s, divided by the thermal conductivity of the wall material, k_t, as per Equation 18 (Fluent, 2015).

To allow for heat transfer at the wall, two different types of thermal boundary conditions could be used. They are the temperature and the convective heat transfer boundary conditions.

$$Q = h_g(T_w - T_g) \tag{19}$$

$$Q = h_l(T_l - T_w) \tag{20}$$

The temperature boundary condition uses Equation 19 and requires a user input for the wall temperature, T_w (Fluent, 2015).

Equation 20 (Fluent, 2015) is used for the convective heat transfer boundary condition where both the water side heat transfer coefficient, h_l, and water temperature are user defined. In the current one dimensional thermal calculation from Section 3 a heat transfer coefficient for the water side of 11500 W/m^2.K is used (du Toit, 2002).

To determine which boundary condition model will result in the most accurate solution a comparison is done using the two models for seven of the test inlet conditions. The test points selected ensure that the full inlet velocity range is compared.

Table 5: Comparison of temperature and convective heat transfer boundary condition models

Test point	u_{in} m/s	T_{in} K	T_{out} K		ΔP Pa	
			Temperature BC	Convective BC	Temperature BC	Convective BC
1	14.6	764	411	411	309	308
2	15.2	733	411	411	355	356
3	16.4	675	410	410	456	456
4	19.3	649	411	411	663	664
5	20.3	639	411	411	746	745
7	12.2	682	403	403	260	260
8	13.9	656	404	405	353	352

It can be seen from the results in Table 5 that the two models yield almost identical results. As previously noted the temperature boundary condition requires one user input whereas the convective boundary condition requires two user inputs. The h_l user input for the convective boundary condition is assumed to be 11500 W/m^2.K. Therefore to reduce the quantity of assumed values the temperature boundary condition model will be used.

4.4.3. Outlet

The outlet boundary condition is set as a pressure outlet with a zero gauge pressure. It is expected that the flow will only be leaving this boundary and that there will be no recirculation of flow at the boundary.

4.5. Material

The spirally corrugated tube is made from EN10216-2 P235GH. Due to the wall being modelled as a thin-wall thermal resistance the material properties cannot vary with temperature. Values for thermal conductivity and specific heat at the free stream temperature is therefore used as per Table 6.

Table 6: Properties of P235GH

T		ρ	k_t	c_p
K	°C	kg/m^3	W/m.K	J/kg.K
373	100	7850	55.7	479

The fluid in this model is air. The density properties are changed to that of an incompressible ideal gas as the velocities are far below those required to induce compressible flow. The specific heat is set to a piecewise polynomial dependent on temperature.

Table 7: Thermal conductivity of air

T		k_{air}
K	°C	W/m.K
373	100	0.03095
393	120	0.03235
413	140	0.03374
433	160	0.03511
453	180	0.03646
473	200	0.03779
523	250	0.04104
573	300	0.04418
623	350	0.04721
673	400	0.05015
773	500	0.05572
873	600	0.06093

Thermal conductivity is set to a piecewise linear function with values ranging from the wall temperature to the maximum inlet gas temperature as shown in Table 7.

All additional settings can be found in Appendix A.

4.6. Turbulence model

The spiral corrugated tube is modelled in FLUENT using the k-ε realizable turbulence model where k is the turbulent kinetic energy and ε is the dissipation rate of the turbulent energy.

$$\frac{\partial}{\partial t}(\rho k) + \frac{\partial}{\partial x_j}(\rho k u_j) = \frac{\partial}{\partial x_j}\left[\left(\mu + \frac{\mu_t}{\sigma_k}\right)\frac{\partial k}{\partial x_j}\right] + G_k + G_b - \rho\varepsilon - Y_M + S_k \tag{21}$$

$$\frac{\partial}{\partial t}(\rho\varepsilon) + \frac{\partial}{\partial x_j}(\rho\varepsilon u_j) = \frac{\partial}{\partial x_j}\left[\left(\mu + \frac{\mu_t}{\sigma_\varepsilon}\right)\frac{\partial \varepsilon}{\partial x_j}\right] + \rho C_1 S\varepsilon - \rho C_2 \frac{\varepsilon^2}{k + \sqrt{v\varepsilon}} + C_{1\varepsilon}\frac{\varepsilon}{k}C_{3\varepsilon}G_b + S_\varepsilon \tag{22}$$

These two transport equations are defined as per Equations 21 and 22 by Shih et al. (1994).The 2 transport equations are solved using the constants for strain, S, and turbulence transport, C_1, as defined by Shih et al. (1994) in the following two equations.

$$C_1 = max\left(0.43, \frac{S\frac{k}{\varepsilon}}{S\frac{k}{\varepsilon} + 5}\right) \tag{23}$$

$$S = \sqrt{2S_{ij}S_{ij}} \tag{24}$$

This turbulence model has been used in similar corrugated tube models previously done by Mohammed et al. (2013), Ahsan (2014), Han et al. (2012), Ağra et al. (2011) and Li et al. (2012). All of these models corresponded accurately to test and/or empirical correlations. It is therefore expected that the use of the k-ε realizable turbulence model will yield accurate solutions.

The realizable model solves the eddy viscosity, μ_t, as defined by the following equation. However, unlike the standard k-ε model the variable for turbulent viscosity, C_μ, becomes a function of the mean strain and the rate of rotation of the fluid instead of remaining a constant (Shih et al., 1994)

$$\mu_t = \rho C_\mu \frac{k^2}{\varepsilon} \tag{25}$$

This prevents the development of negative normal Reynolds stresses which in reality are physically impossible to obtain. The realizable model therefore should allow for a more accurate result for flow separation and swirling fluid flow as stated by Shih et al. (1994).

The Enhanced Wall Treatment option is used as the near-wall modelling method. This method combines enhanced wall functions with the two-layer approach. For

the two-layer approach the fluid domain is divided into two regions namely the viscous sublayer region and the fully-turbulent region.

The turbulent Reynolds number, Re_t, as defined by Fluent (2015) in Equation 26 demarcates the two regions with y being the distance to the nearest wall as defined by Equation 27 and is independent to the mesh topology.

$$Re_t \equiv \frac{\rho y \sqrt{k}}{\mu} \tag{26}$$

$$y \equiv \min_{\vec{r_w} \epsilon \Gamma_w} \|\vec{r} - \vec{r_w}\| \tag{27}$$

The fully turbulent region is solved using transport Equations 21 and 22 when the turbulent Reynolds number is greater than 200.

In the viscous sublayer when the turbulent Reynolds number is less than 200, transport Equation 21 is used to calculate the turbulent kinetic energy. The dissipation rate is calculated using Equation 28 with Equation 29. The turbulent viscosity, $\mu_{t,viscous}$, is calculated from Equation 30 using Equation 31 and not Equation 25 as in the fully turbulent region.

$$\varepsilon = \frac{k^{\frac{3}{2}}}{l_\varepsilon} \tag{28}$$

$$l_\varepsilon = y\kappa C_\mu^{-\frac{3}{4}} \left(1 - exp^{\frac{-Re_t}{2\kappa C_\mu^{-\frac{3}{4}}}} \right) \tag{29}$$

$$\mu_{t,viscous} = \rho C_\mu l_\mu \sqrt{k} \tag{30}$$

$$l_\mu = y\kappa C_\mu^{-\frac{3}{4}} \left(1 - exp^{\frac{-Re_t}{70}} \right) \tag{31}$$

A blending function, λ_ε, is then used to combine the results of the two regions and is calculated from Equations 32 and 33. This is to ensure that the solution converges even if the turbulent viscosity calculated with Equations 25 and 30 are not identical at a point on the border between the two regions.

$$\lambda_\varepsilon = 0.5 \left[1 + \tanh \frac{Re_t - 200}{A_\varepsilon} \right] \tag{32}$$

$$A_\varepsilon = \frac{|\Delta Re_t|}{\tanh^{-1}(0.98)} \tag{33}$$

The turbulent viscosity with blending function, $\mu_{t,enhanced}$, is calculated using Equation 34 as defined by Fluent (2015).

$$\mu_{t,enhanced} = \lambda_\varepsilon \mu_t + (1 - \lambda_\varepsilon)\mu_{t,viscous} \tag{34}$$

The non-dimensional velocity is also blended using the Equations 35 and 36. This blending function ensures a smooth transition between the viscous sublayer and the fully turbulent regions and gives a fairly accurate representation of the velocity profile in the buffer region.

$$u^+ = exp^{\Gamma} u^+_{lam} + exp^{\frac{1}{\Gamma}} u^+_{turb} \tag{35}$$

$$\Gamma = -\frac{0.01(y^+)^4}{1 + 5y^+} \tag{36}$$

To ensure that the correct turbulence model is selected a comparative study is done using the standard and realizable k-ε models for the enhanced, standard and Menter-Lechner wall functions (Fluent, 2015).

Figures 25 and 26 show that for both the realizable and standard k-ε turbulence models, the enhanced wall treatment results for the pressure drop are nearest to the experimental results obtained from the test rig and therefore render the most accurate results.

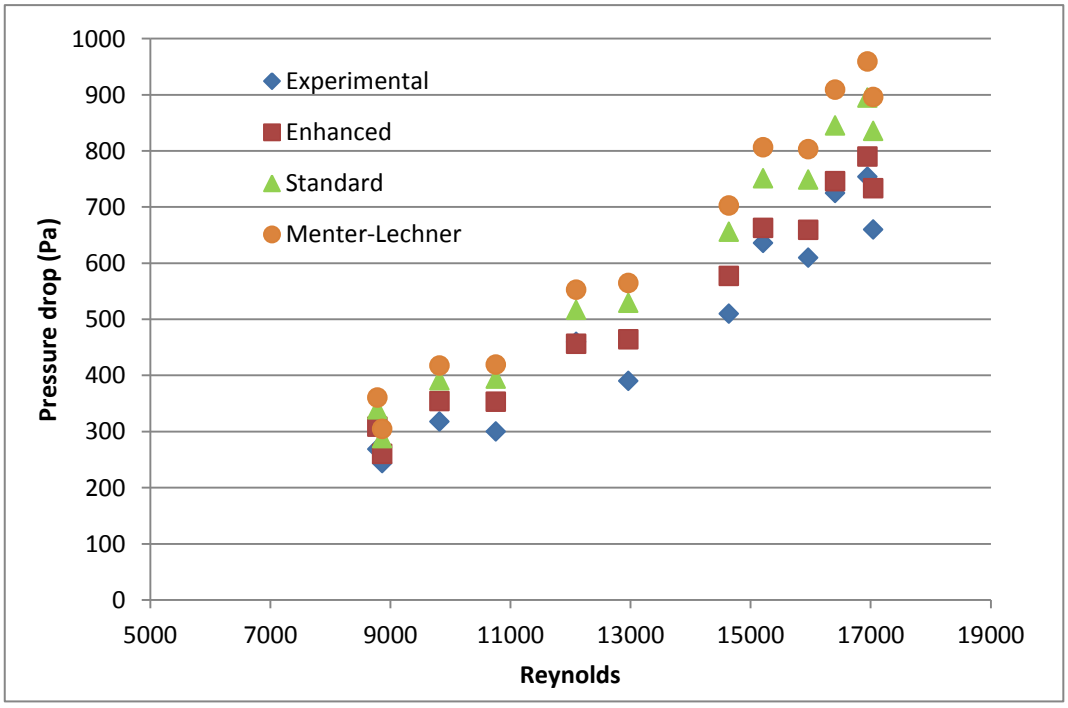

Figure 25: Pressure drop versus Reynolds number using the realizable k-ε model for various wall treatments

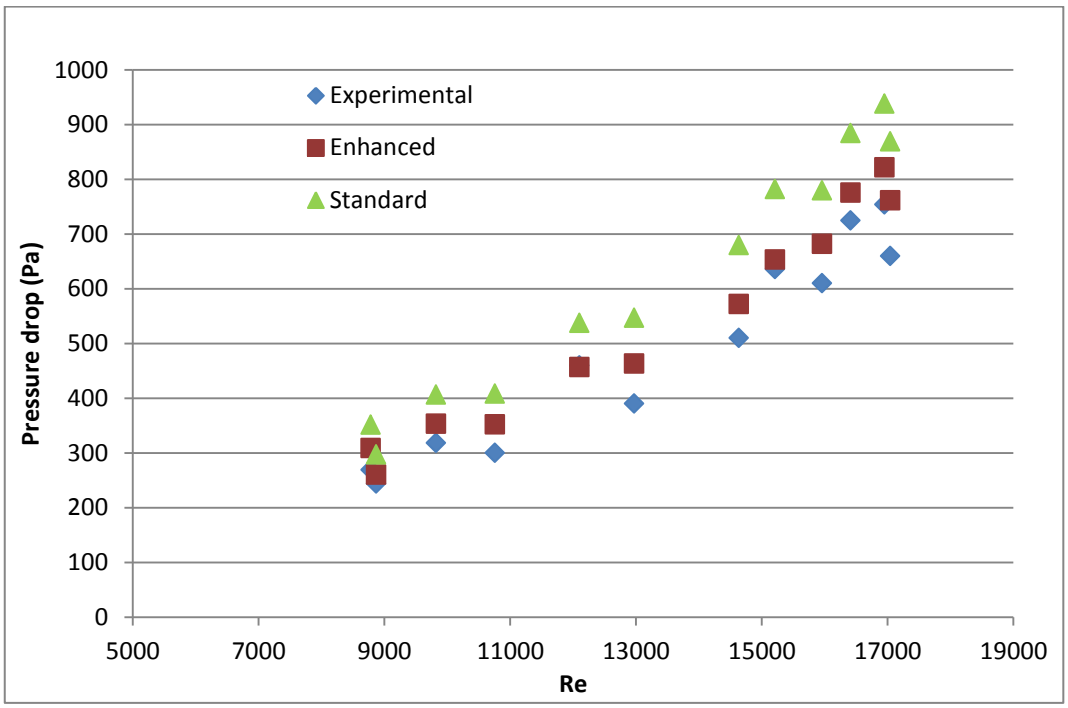

Figure 26: Pressure drop versus Reynolds number using the standard k-ε model for various wall treatments

Tables 8 and 9 depict that the relative deviation on outlet temperature is the least for the enhanced wall treatment for both the realizable and standard k-ε turbulence models.

Table 8: Relative deviation on outlet temperature using the realizable k-ε model

Test point	u_{in} m/s	T_{in} K	ξ_T %		
			Enhanced	Standard	Menter-Lechner
1	14.6	764	0.5	8.1	8.0
2	15.2	733	0.3	7.8	7.8
3	16.4	675	0.1	7.3	7.3
4	19.3	649	0.1	7.4	7.5
5	20.3	639	0.0	7.4	7.4
6	20.9	638	0.1	7.6	7.6
7	12.2	682	0.4	6.2	6.1
8	13.9	656	0.2	6.3	6.3
9	15.7	631	0.3	6.0	6.0
10	17.4	624	0.3	6.1	6.2
11	18.4	613	0.3	6.1	6.1
12	19.3	606	0.4	6.0	6.1
Average			**0.3**	**6.9**	**6.9**

Table 9: Relative deviation on outlet temperature using the standard k-ε model

Test point	u_{in} m/s	T_{in} K	ξ_T %	
			Enhanced	Standard
1	14.6	764	0.5	8.4
2	15.2	733	0.3	8.1
3	16.4	675	0.0	7.6
4	19.3	649	0.3	7.7
5	20.3	639	0.4	7.8
6	20.9	638	0.5	7.9
7	12.2	682	0.3	6.3
8	13.9	656	0.2	6.5
9	15.7	631	0.4	6.2
10	17.4	624	0.6	6.3
11	18.4	613	0.1	6.3
12	19.3	606	0.1	6.3
Average			**0.3**	**7.1**

When comparing the relative deviation in Table 10 for the standard and realizable turbulence models using the enhanced wall treatment, it is seen that both models produce relatively similar results for the outlet temperature.

Table 10: Relative deviation on outlet temperature and pressure for the realizable and standard k-ε turbulence models using the enhanced wall treatment

Test point	u_{in} m/s	T_{in} K	ξ_T %		ξ_P %	
			Realizable	Standard	Realizable	Standard
1	14.6	764	0.5	0.5	12.8	12.9
2	15.2	733	0.3	0.3	10.3	10.0
3	16.4	675	0.1	0.0	0.8	0.7
4	19.3	649	0.1	0.3	4.0	2.6
5	20.3	639	0.0	0.4	2.8	6.5
6	20.9	638	0.1	0.5	4.6	8.3
7	12.2	682	0.4	0.3	6.2	6.3
8	13.9	656	0.2	0.2	15.0	14.8
9	15.7	631	0.3	0.4	16.0	15.8
10	17.4	624	0.3	0.6	11.7	10.8
11	18.4	613	0.3	0.1	7.5	10.5
12	19.3	606	0.4	0.1	10.0	13.4

The relative deviation for the pressure drop for both turbulence models yield almost identical results for the lower velocity inlet range. However, at the higher velocity range of around 18 m/s and above, the realizable turbulence model is more accurate.

Based on this it is shown that the realizable turbulence model chosen is the most suitable for the spiral corrugated tube model.

All additional FLUENT settings can be found in Appendix A.

4.7. Solution methods

The model of the spirally corrugated tube is solved using the pressure-based coupled algorithm. This solution method solves the momentum and pressure-based continuity equations together.

Second order upwind is used as the spatial discretization scheme for momentum, turbulent kinetic energy, turbulent dissipation rate and energy.

4.8. Monitors

Three monitors are used to ensure that a steady-state solution is obtained. An area weighted average is taken of pressure at the inlet boundary and of the temperature and pressure at the outlet boundary.

To ensure that mass is conserved the net mass flow rate over the inlet and outlet boundaries are calculated. For energy conservation, the net total heat transfer rate at the inlet, outlet and wall boundaries is calculated.

4.9. Results

4.9.1. Y+ value

The average y^+ value at the wall was calculated at the three test points with the highest, lowest and average inlet velocities. It is seen in Table 11 that a y^+ value near one is obtained for all three test points as is required for the enhanced wall treatment model for accurate results.

Table 11: Average y+ values at the wall

Test point	u_{in} m/s	y^+
7	12.2	0.7
3	16.4	0.9
5	20.3	1.1

4.9.2. Flow characteristics

4.9.2.1. Inlet straight boundary layers

The velocity and temperature profiles near the wall on the inlet straight section upstream of the spiral corrugation are plotted for test points 7 and 5 at 100 mm from the inlet boundary. These are the two test points with the minimum and maximum inlet velocity conditions. The velocity profiles are shown in Figure 27 and the temperature profiles in Figure 28.

The temperature and velocity profiles are fairly flat as is expected for fully developed turbulent flow.

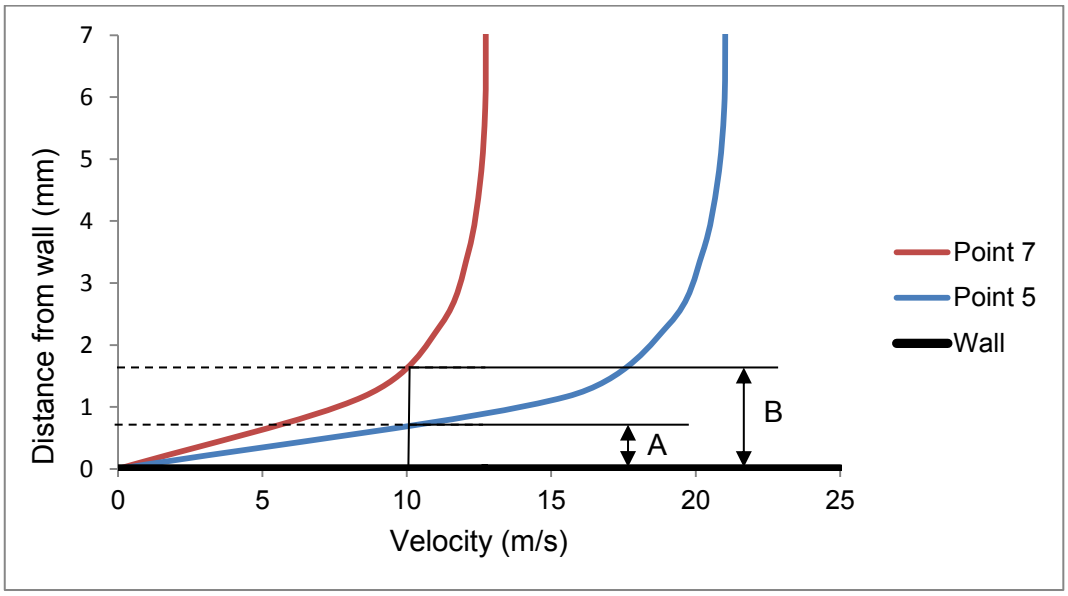

Figure 27: Velocity profiles for test points 5 and 7 on straight inlet section

The velocity boundary layer close to the wall is thinner for test point 5, with the higher inlet velocity condition, than for test point 7. These two thicknesses are indicated as ‘A’ and ‘B’ in Figure 27 respectively.

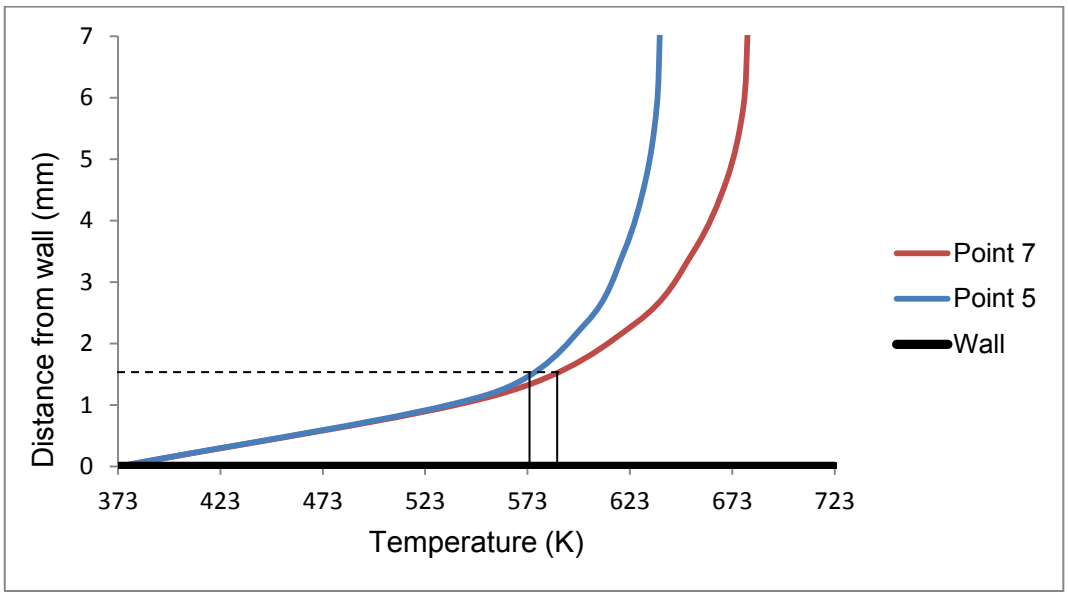

Figure 28: Temperature profiles for test points 5 and 7 on straight inlet section

In Figure 28 it is seen that the temperature reduces faster at test point 5 at the higher velocity than at test point 7. This indicates that the heat transfer rate is higher at the increased velocity.

It can therefore be said that the heat transfer rate will increase as the velocity of the fluid increases.

4.9.2.2. Spiral indentation boundary layers

The velocity contours at the spiral indentation for the three test points from Section 4.9.1 are shown in Figures 29 to 31. It is seen that the corrugated indentation disrupts the velocity profile. The higher the inlet velocity of the fluid is, the thinner the low velocity layer is on the trailing side of the indentation.

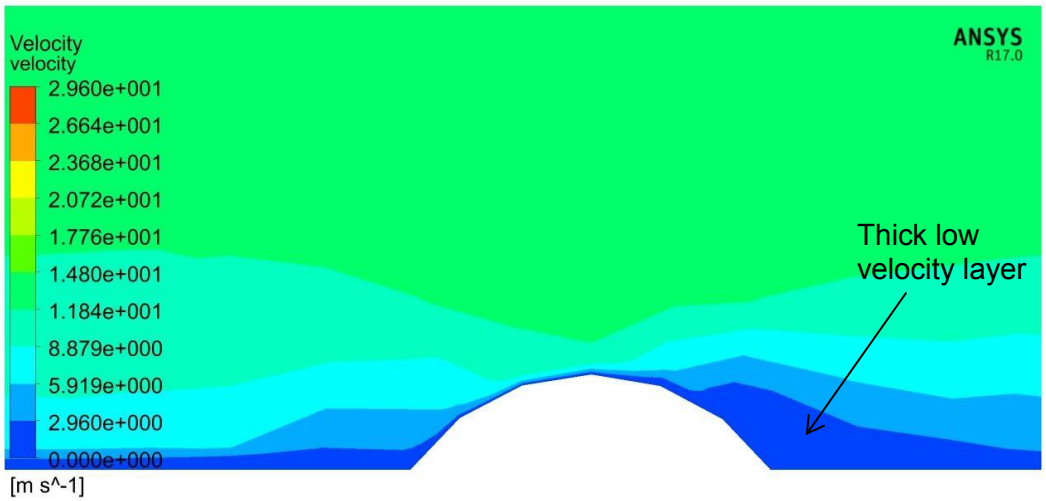

Figure 29: Velocity contours for test point 7 over spiral indentation – Inlet velocity: 12.2 m/s

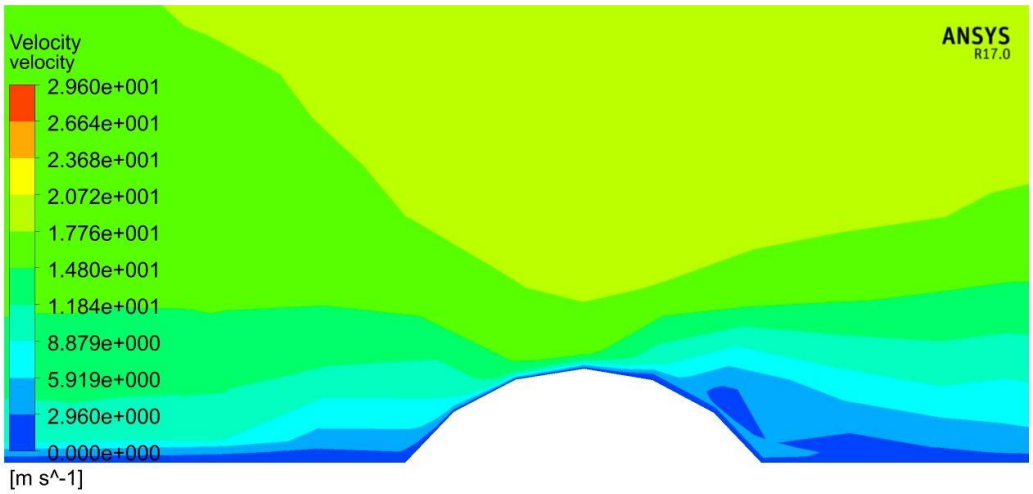

Figure 30: Velocity contours for test point 3 over spiral indentation – Inlet velocity: 16.4 m/s

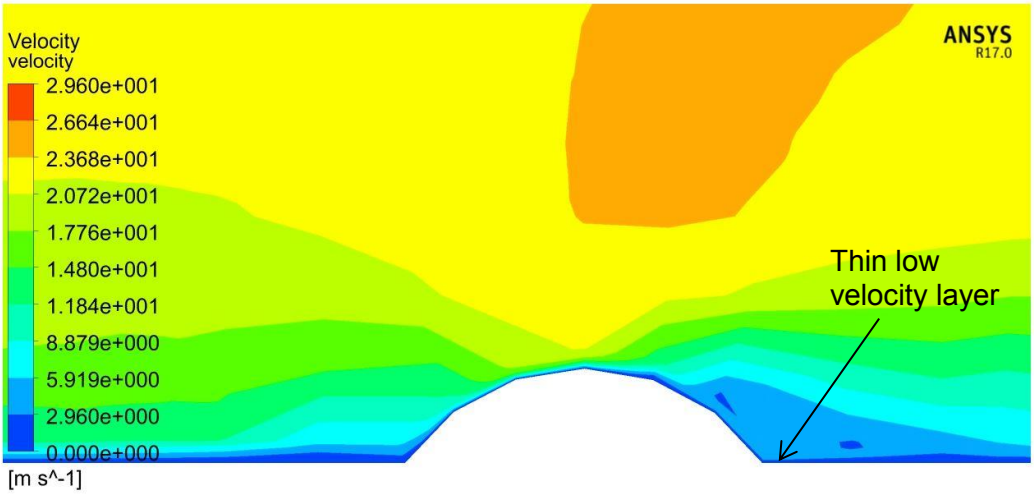

Figure 31: Velocity contours for test point 5 over spiral indentation – Inlet velocity: 20.3 m/s

The velocity vectors around the spiral indentation are plotted in Figure 32. A low velocity recirculation zone, also known as an eddy, is seen on the trailing edge of the indentation. Higher velocity fluid is pushed away from the wall and over the eddy. This corresponds to boundary layer separation and reattachment as described in Section 2.5.2.

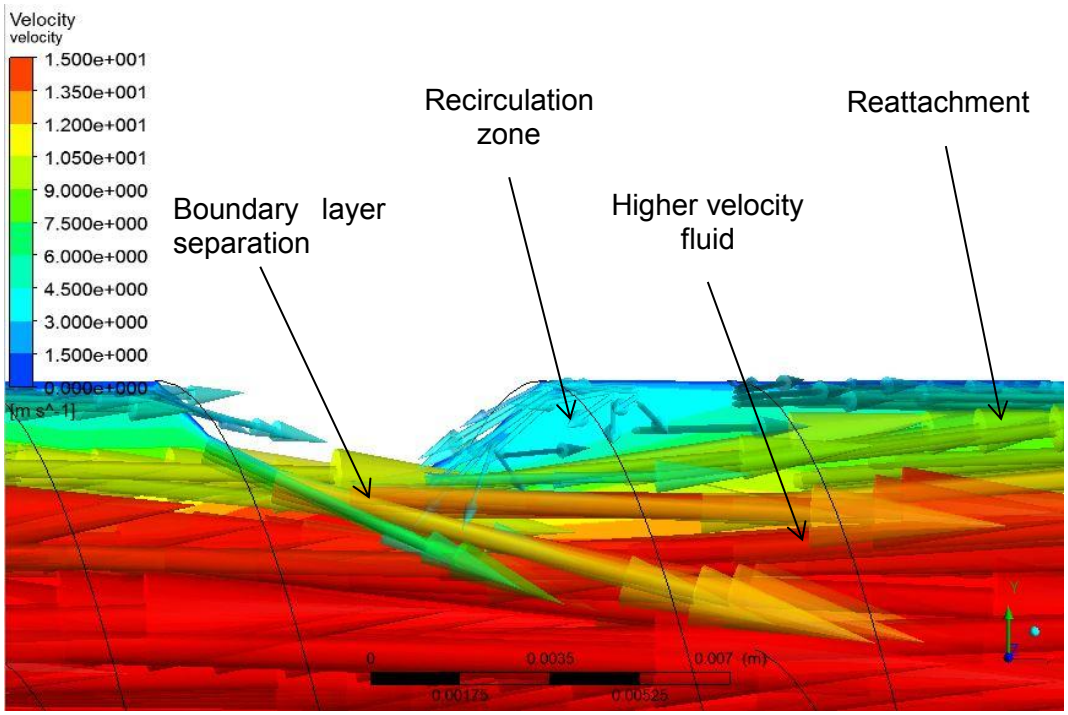

Figure 32: Velocity vectors around spiral indentation

The low pressure zone on the trailing edge of the indentation can be seen in Figures 33 to 35. The differential pressure between the leading and trailing edge of the indentation is significantly higher for test point 5 (Figure 35) of around 120 Pa than for test point 7 of roughly 35 Pa (Figure 33).

This shows that even though the velocity profile stabilises faster again with an increased velocity, the pressure drag of the indentation increases with increasing velocity.

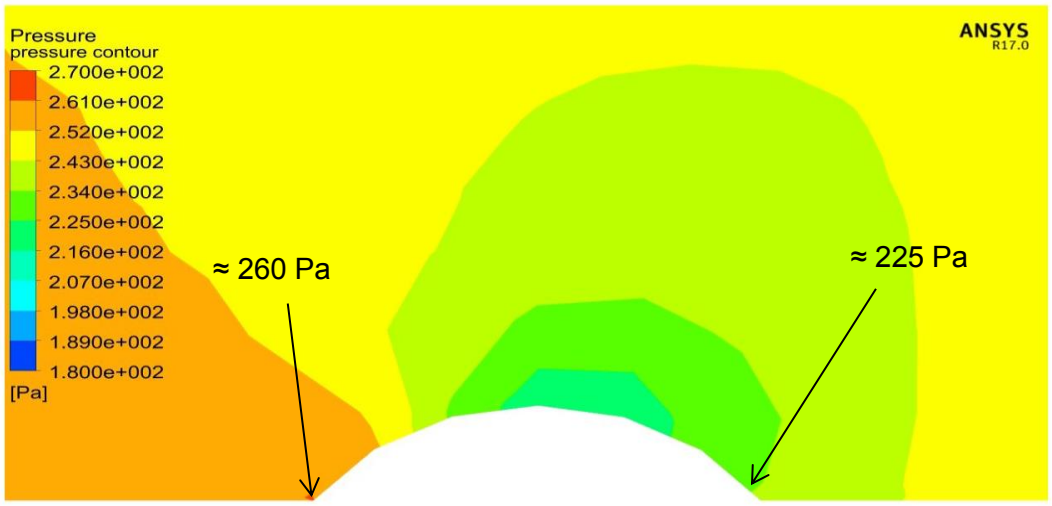

Figure 33: Pressure contours for test point 7 over spiral indentation – Inlet velocity: 12.2 m/s

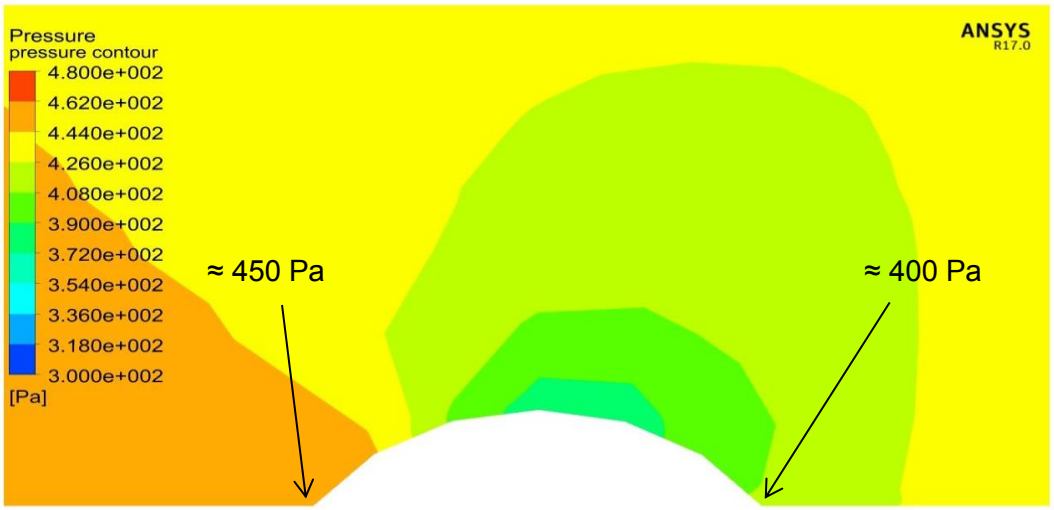

Figure 34: Pressure contours for test point 3 over spiral indentation – Inlet velocity: 16.4 m/s

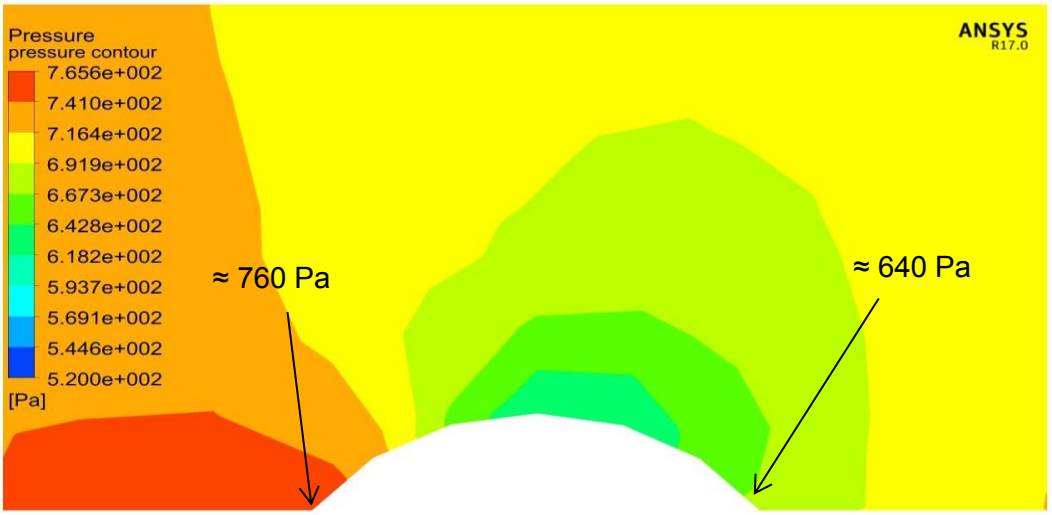

Figure 35: Pressure contours for test point 5 over spiral indentation – Inlet velocity: 20.3 m/s

4.9.2.3. Secondary swirl flow

The spiral corrugation does not only cause flow disruptions close to the wall along the length of the tube but it also initiates a secondary swirling flow around the centre line of the tube length.

The velocity streamlines are plotted and this swirling flow can be seen in Figure 36 where a high velocity central core is maintained and a lower velocity band of fluid rotates around this core. This swirling action promotes turbulence of the fluid.

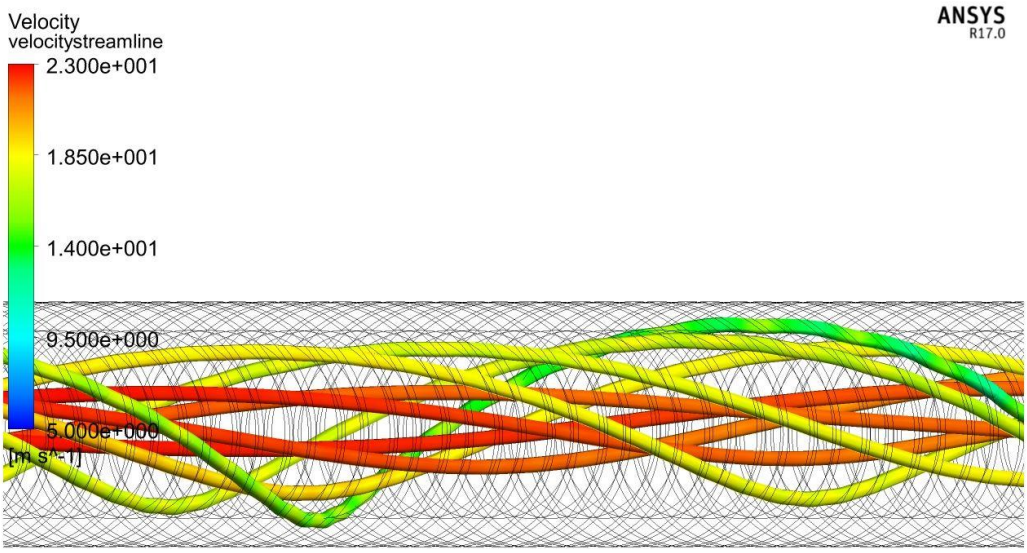

Figure 36: Velocity streamlines showing secondary swirl flow

4.9.3. CFD and experimental results comparison

The results obtained from the CFD simulations and the empirical correlations in Chapter 3 are compared to those obtained from the experimental results from the test rig (du Toit, 2002). These results are tabulated in Table 12. The average relative deviation for the pressure drop across the tube length, $\xi_{P,}$ between the CFD and experimental results is 8.5 %. This is lower than ξ_P of 10.3 % attained between the empirical correlation in Section 3 and experimental results.

Table 12: Average relative deviation on pressure drop and Nusselt number

Test point	u_{in} m/s	T_{in} K	ξ_{Nu} %		ξ_P %	
			CFD & Experimental	Empirical & Experimental	CFD & Experimental	Empirical & Experimental
1	14.6	764	3.6	7.1	12.8	14.0
2	15.2	733	5.9	7.0	10.3	11.5
3	16.4	675	2.8	7.0	0.8	1.1
4	19.3	649	5.8	6.9	4.0	7.0
5	20.3	639	6.6	6.9	2.8	6.0
6	20.9	638	6.8	6.9	4.6	8.4
7	12.2	682	0.5	7.2	6.2	3.4
8	13.9	656	4.1	7.0	15.0	15.2
9	15.7	631	7.3	7.0	16.0	19.9
10	17.4	624	7.3	6.9	11.7	14.4
11	18.4	613	10.1	6.8	7.5	9.6
12	19.3	606	11.0	6.8	10.0	12.9
Average			**6.0**	**7.0**	**8.5**	**10.3**

The pressure drop results obtained from the CFD simulations, experimental and empirical correlations are plotted against the Reynolds number at the log mean temperature difference (LMTD) in Figure 37.

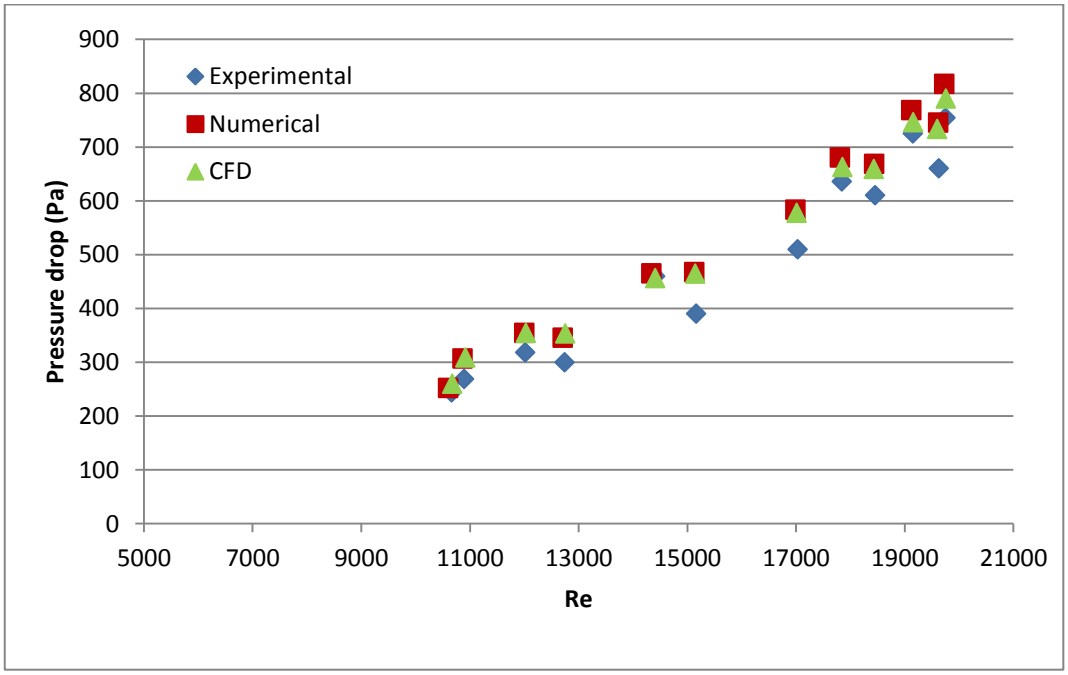

Figure 37: Pressure drop versus Reynolds number for CFD, experimental and empirical results

An average relative deviation for the Nusselt number, ξ_{Nu}, of 6.0 % is calculated between the experimental results and the CFD results. This is similar to the 7.0 % obtained between the experimental results and Equation 6 from Section 3. This means that the CFD model nullifies the requirement of the correction factor added in the Nusselt number empirical correlation.

The results are plotted in Figure 38 where both the Nusselt and Reynolds numbers are calculated at the LMTD.

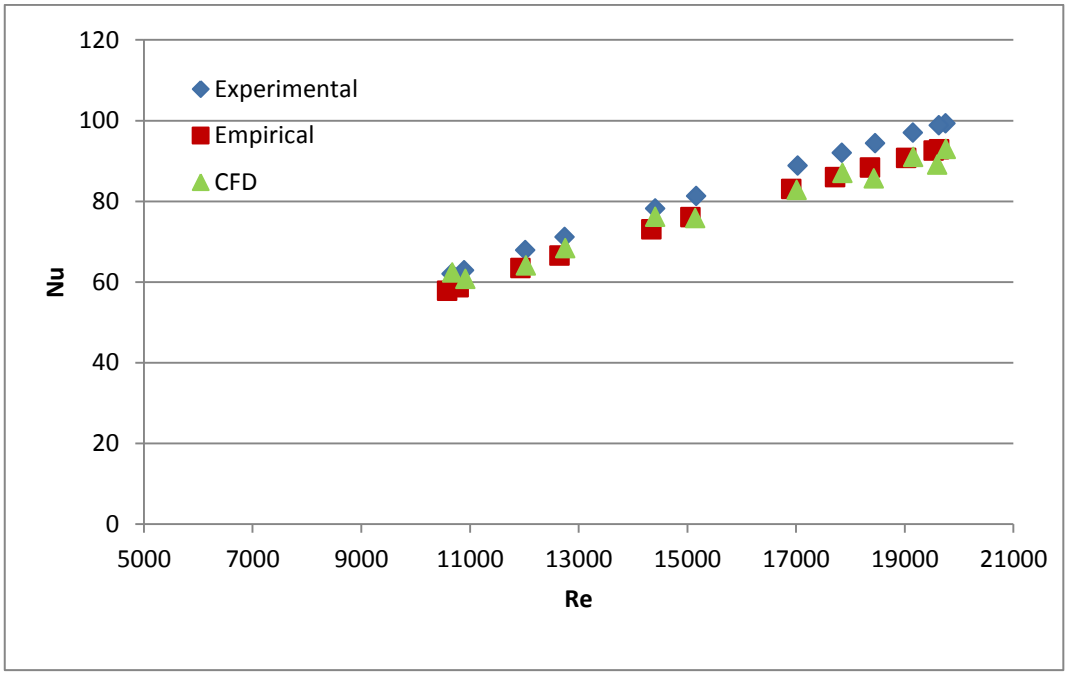

Figure 38: Nusselt number versus Reynolds number for CFD, experimental and empirical results

4.10. Conclusion

The results obtained from the CFD model correlate fairly accurately to the experimental results obtained from the test rig where the average ξ_P of 8.5 % and average ξ_{Nu} of 6.0 % is attained.

The average relative deviation on the outlet gas temperature, ξ_T, between the experimental results and CFD results is 0.3 %.

The CFD model has therefore been validated against the test results and can be used to determine what effects the spiral corrugation geometrical parameters have on the heat transfer rate.

The investigation of the flow characteristics in the CFD simulations show that the higher the velocity of the fluid is, the thinner the boundary layer at the wall becomes, thereby increasing the heat transfer rate. The pressure drag over the

indentations also increases with increased inlet velocity thereby resulting in a greater pressure drop across the tube length.

These two observations correlate to the theory of turbulent flow discussed in Section 2 and therefore it can be said that the flow characteristics observed in the CFD simulations reflect fairly accurately the actual flow patterns expected inside a spirally corrugated tube.

5. Spiral corrugation geometric parameters

5.1. Introduction

The heat transfer rate and pressure drop across the spiral tube length is affected by the spiral corrugation characteristics. By changing the pitch and depth of the corrugation the heat transfer rate can be improved.

In this section the effects of changing individual geometric parameters will be investigated as well as combinations of the parameters.

5.2. Effects of change of spiral pitch and depth individually

Two models, namely A and B, were run to determine what effects the spiral pitch and depth have on the heat transfer rate and pressure drop of the corrugated tube.

Table 13: Geometrical variations for models A and B

Model	p mm	e mm
Current	25	2.0
A	25	2.8
B	20	2.0

The spiral depth is increased for model A and the spiral pitch is decreased for model B as per Table 13 above. All mesh and solver settings from Section 4 are used for the two new models and can be found in Appendix B.

5.2.1. Y+ value

The average y^+ value at the wall is calculated for the 3 models at test point 5 and 7. These are the two test points with the minimum and maximum inlet velocity condition respectively. Should the y^+ values be acceptable at these two points, it can be assumed that it will be acceptable for the remaining other ten test points.

The y+ values for all the models at the two test points approach one as shown in Table 14. This is the requirement for the enhanced wall treatment model for accurate results.

Table 14: Average y+ values at the wall

Model	Test point	u_{in} m/s	y^+
Current	5	12.2	0.7
	7	20.3	1.1
A	5	12.2	0.8
	7	20.3	1.3
B	5	12.2	0.7
	7	20.3	1.1

5.2.2. Results

The pressure drop and LMTD Nusselt number are plotted against the LMTD Reynolds number for the three models in Figures 39 and 40. Increasing the spiral corrugation depth has a greater effect on the heat transfer rate and pressure drop than decreasing the spiral pitch.

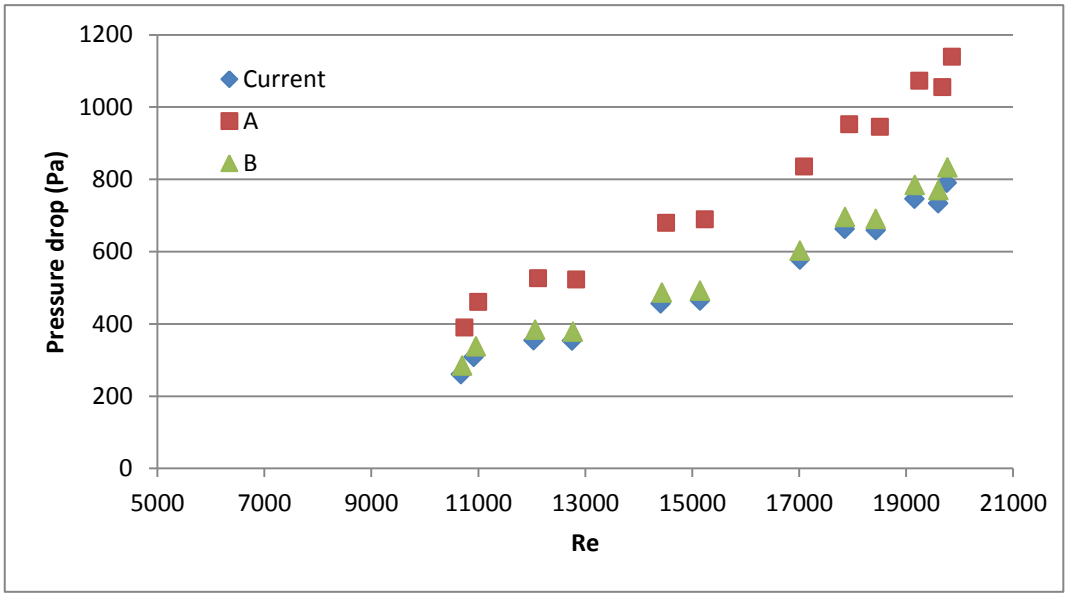

Figure 39: Pressure drop versus Reynolds number for current, A and B models

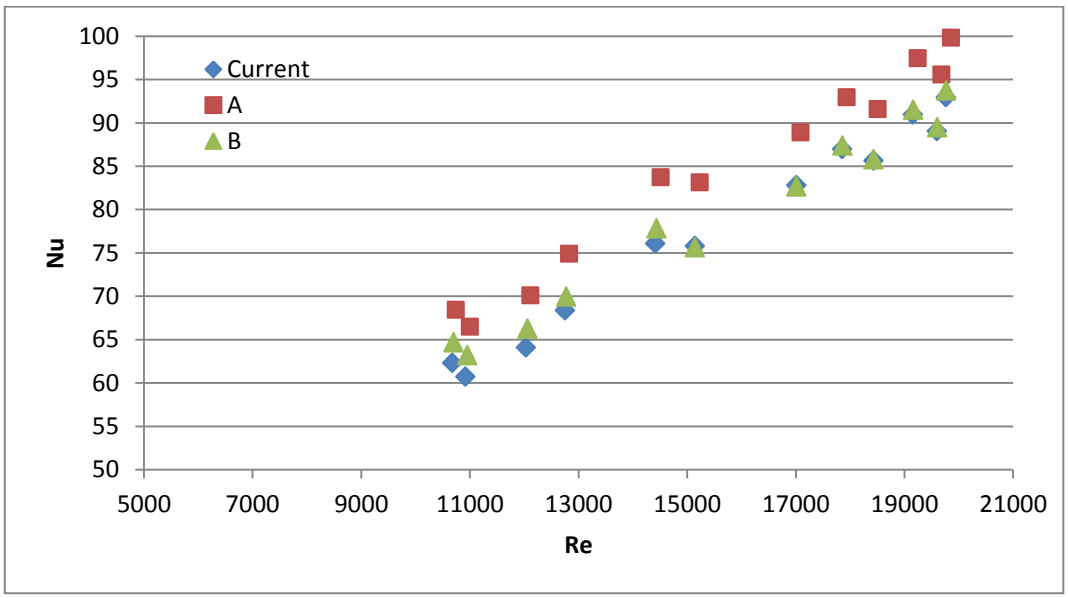

Figure 40: Nusselt number versus Reynolds number for current, A and B models

ξ_P and ξ_T between the current and adjusted models, A and B, are calculated and tabulated in Table 15. In both models a slight improvement of the heat transfer rate results in a substantial increase in the pressure drop across the tube length.

Table 15: Relative pressure drop and outlet temperature deviation compared to current spiral corrugated tube.

Model	ξ_P %	ξ_T %
A	31.7	1.4
B	5.9	0.3

5.2.2.1. Change in spiral depth

To determine what effect the change in spiral depth has on the flow characteristics, the flow around the indentations are examined between the current model and model A.

The pressure contours around one of the indentations are plotted over the range of zero to 80 Pa for test point 5 for both models. It is seen in Figures 41 and 42 that the pressure differential over the indentation for model A is almost double that of the current model.

This shows that the indentation depth has a significant effect on the pressure drag over the indentation where the increased depth increases the pressure drop over the indentation.

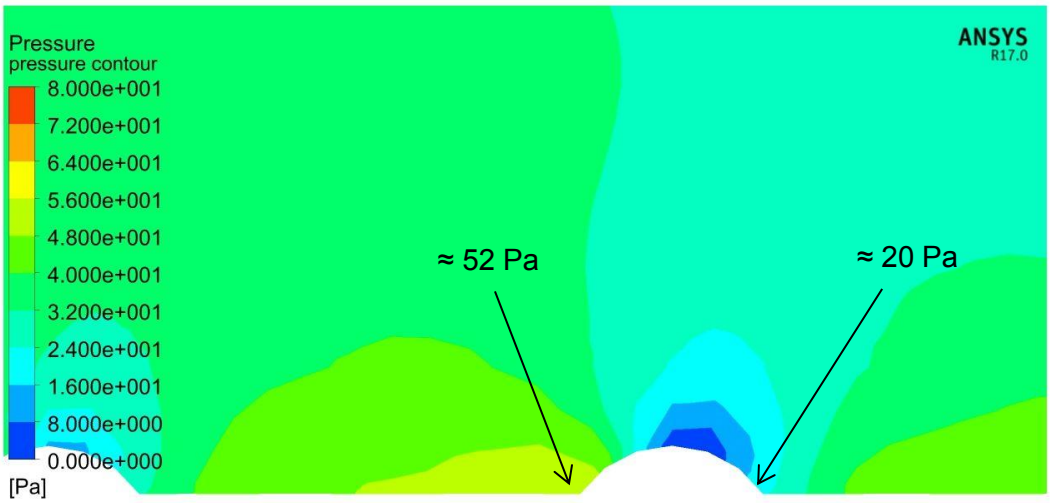

Figure 41: Pressure contours for test point 5 for current corrugation profile

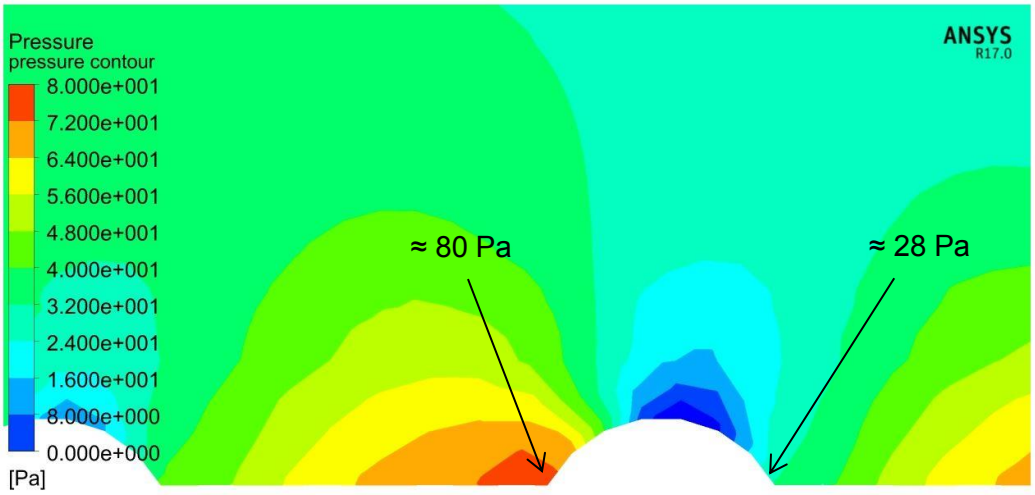

Figure 42: Pressure contours for test point 5 for Model A – increased spiral depth

The velocity contours are plotted around one of the indentations for test point 5 for the current and A models in Figures 43 and 44. Here it is seen that the thickness of the low velocity boundary layer close to the wall is thinner with the increased spiral depth of Model A than for the current model. As previously discussed the thinner the viscous sublayer is, the higher the heat transfer rate will be.

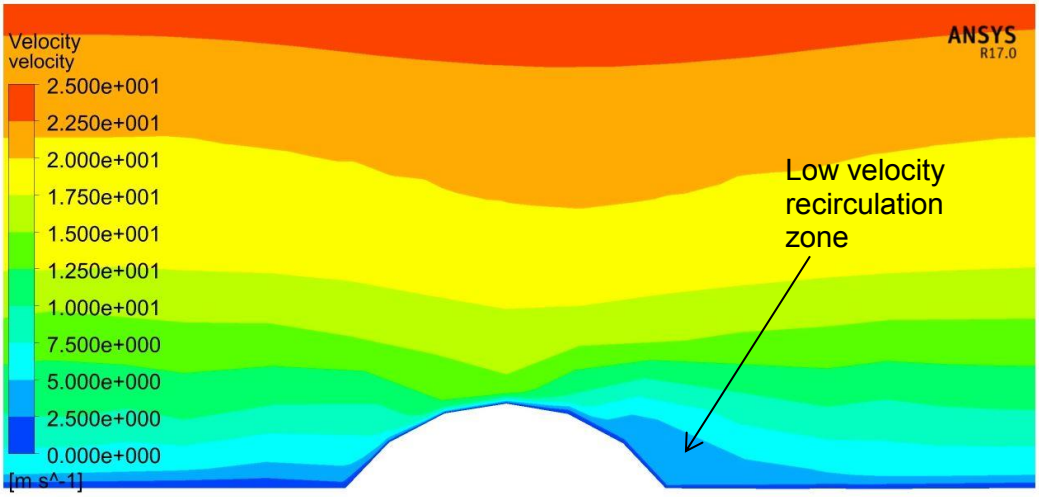

Figure 43: Velocity contours for test point 5 for current corrugation profile

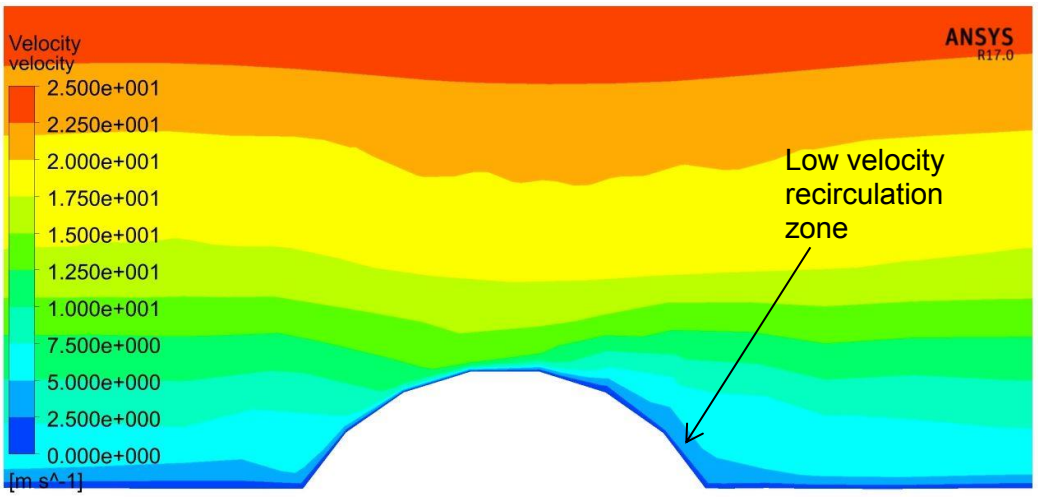

Figure 44: Velocity contours for test point 5 for Model A – increased spiral depth

The size of the low velocity recirculating region also decreases with increasing spiral depth. This may be contrary to what is expected however if the secondary swirl flow is taken into consideration this effect can be expected.

To understand this more clearly the velocity contours are plotted in Figures 45 and 46 for the current and A models at a distance of 1750 mm from the inlet boundary. The red region indicates the high velocity fluid. In the current model the high velocity fluid remains fairly symmetrical at the centre of the tube. In model A however, the high velocity fluid moves back and forth from the top to the bottom of the tube. This shows a high secondary swirl flow.

This swirl flow also occurs in the current model however it is only dominant in the last 30 % of the tube length where as in Model A it is dominant for 60 % of the tube length.

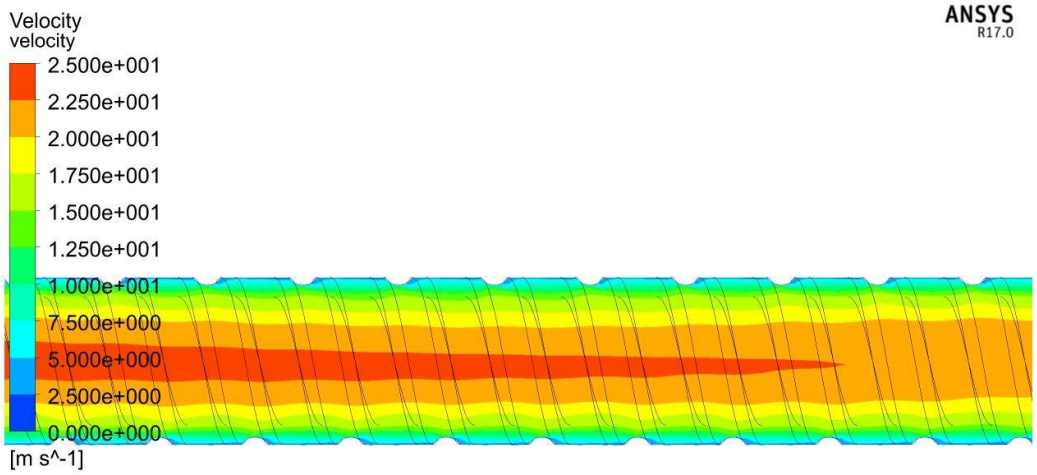

Figure 45: Velocity contours for test point 5 for current corrugation profile

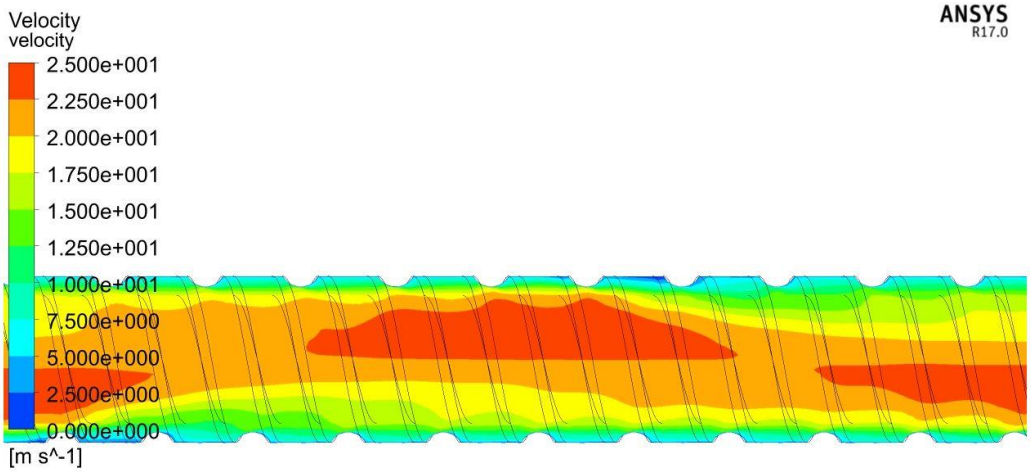

Figure 46: Velocity contours for test point 5 for Model A – increased spiral depth

By plotting the velocity streamlines in Figure 47 for Model A again at a distance of 1750 mm from the inlet boundary, this high level secondary swirl flow can be seen. The swirl flow continually promotes turbulence inside the tube and thereby increases the heat transfer rate. This corresponds to the results obtained from model A in Table 15.

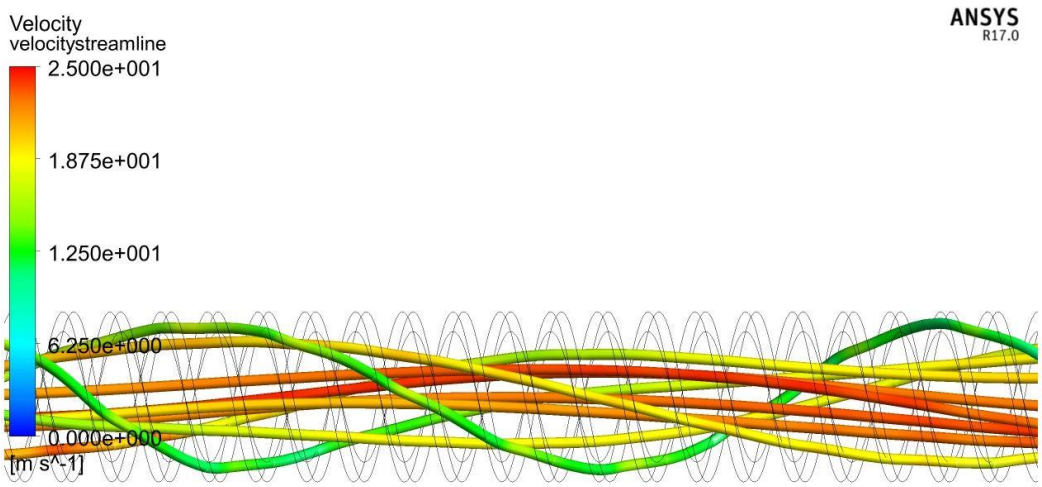

Figure 47: Velocity streamlines for test point 5 for Model A – increased spiral depth

5.2.2.2. Change in spiral pitch

The effect of changing the spiral pitch on the flow characteristics is investigated by comparing the results obtained from the current model and model B.

The velocity contours are plotted at a distance of 2300 mm from the inlet boundary in Figures 48 and 49. From this point onwards the velocity profiles differs significantly between the two models.

In the current model the high velocity zone oscillates between the top and the bottom of the tube. This is in line with the action of the secondary swirl motion. In model B however the high velocity zone is more symmetrical around the x-axis and seems to pulse along the length of the tube. It is therefore shown that by decreasing the pitch, the secondary swirl intensity does not increase as was seen when the spiral depth was increased.

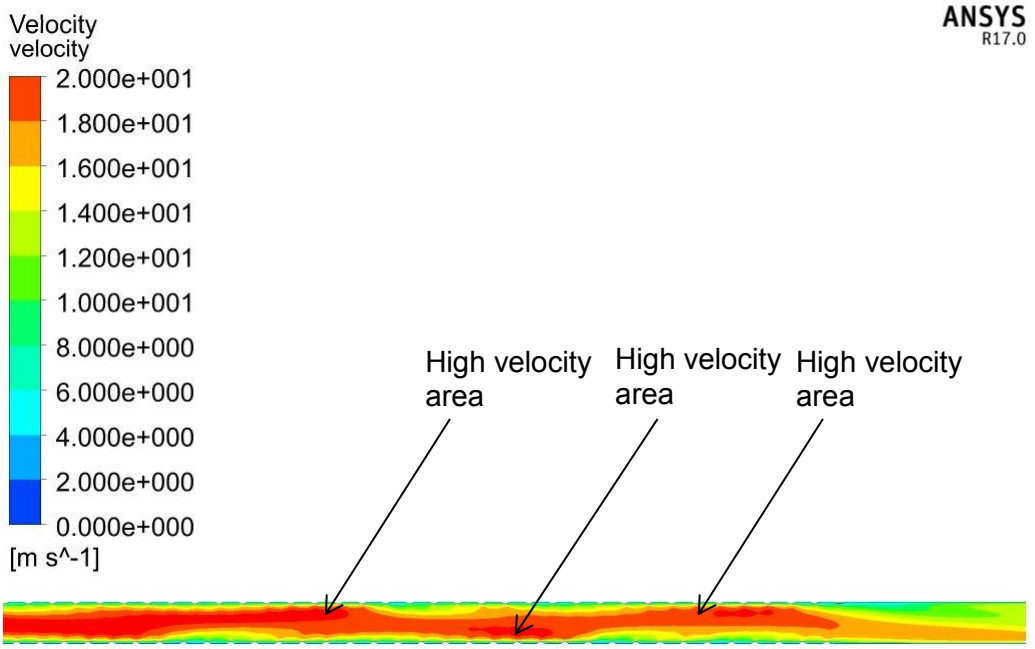

Figure 48: Velocity contours for test point 5 for current corrugation profile

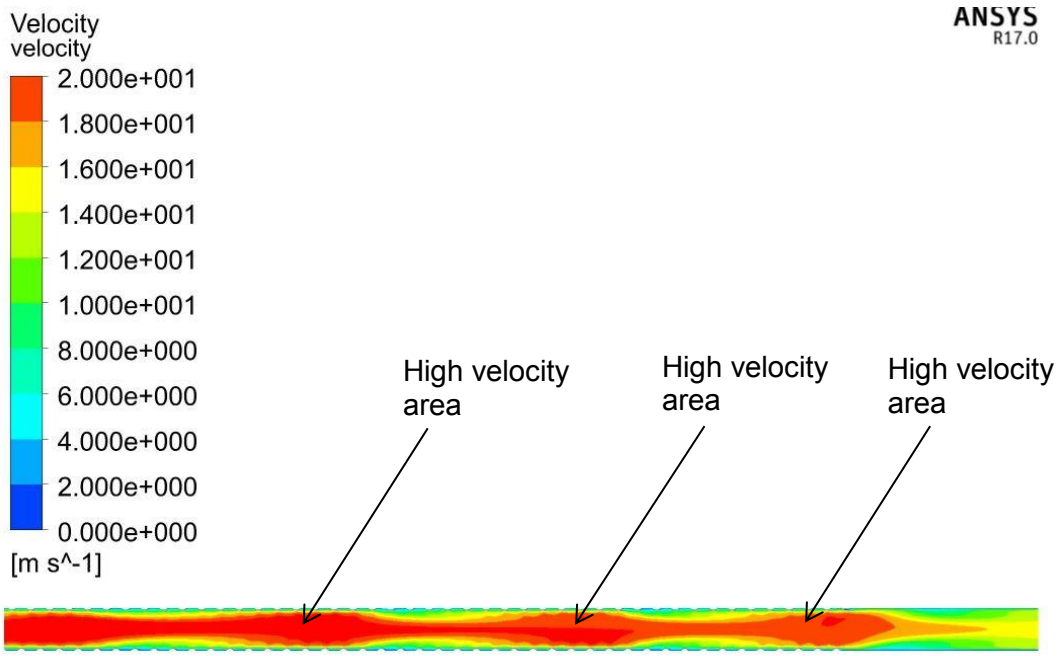

Figure 49: Velocity contours for test point 5 for Model B – decreased spiral pitch

To determine the extent of the effect the decreased spiral pitch has on the fluid flow close to the wall, the velocity contours at the indentations are investigated.

The velocity contours between consecutive indentations are shown in Figures 50 and 51. In the current model the low velocity boundary layer close to the wall

remains thin along the straight lengths between the indentations. This is due to the distance between the indentations being sufficient to allow the flow to return to a stable pattern where reattachment can occur as discussed in Section 2.5.2.

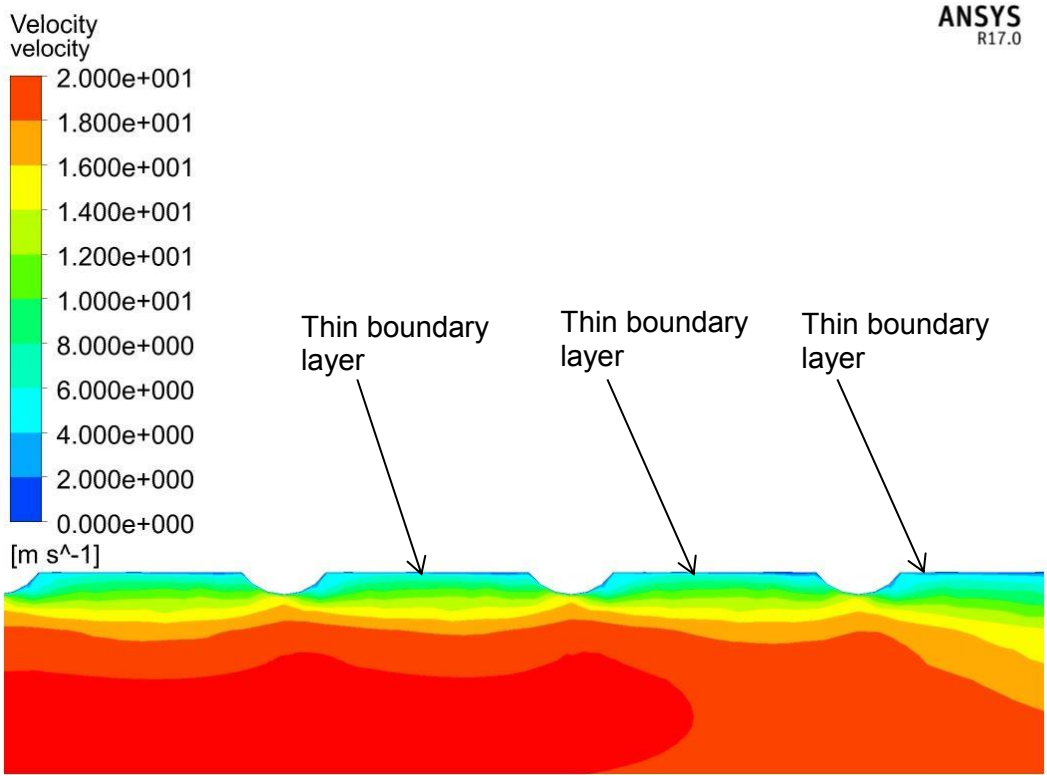

Figure 50: Velocity contour at wall for test point 5 for current corrugation profile

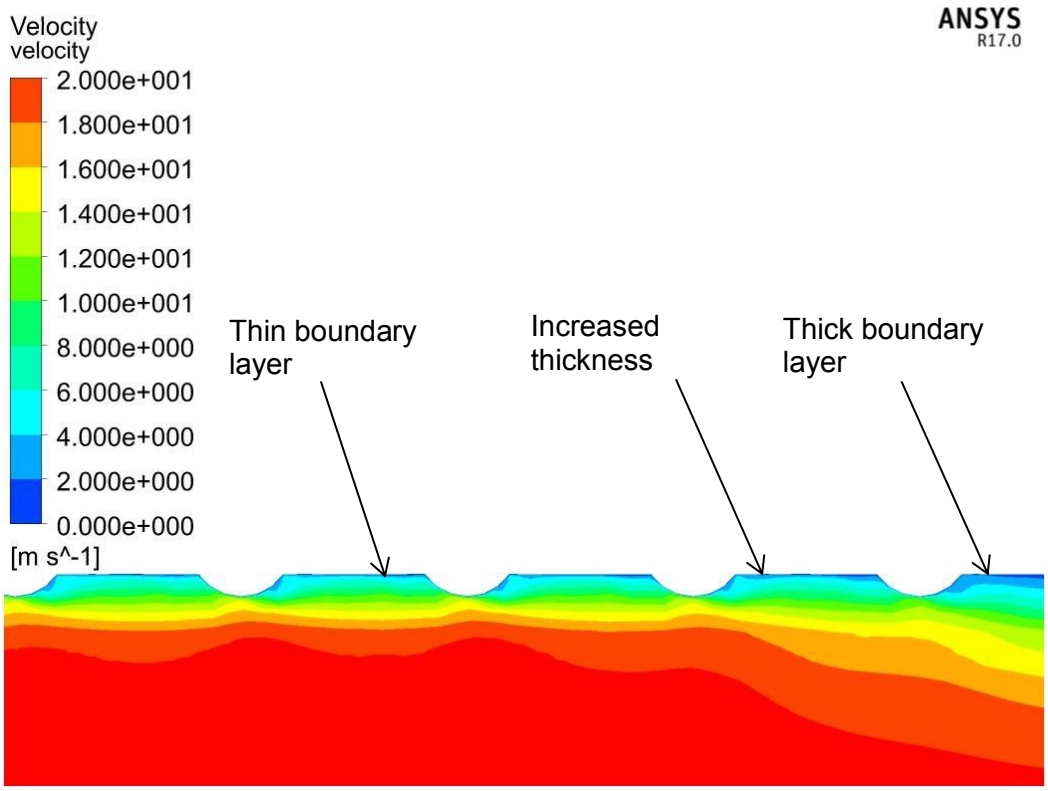

Figure 51: Velocity contour at wall at start of pulse for test point 5 for Model B – decreased spiral pitch

For Model B however it is seen that the low velocity boundary layer close to the wall increases down the length of the tube at the beginning of the "pulse" seen in Figure 49.

The pulse like flow is the result of interference between the indentations in the separation and reattachment zone of the boundary layer. The boundary layer separates from the wall at the separation point on the indentation where the viscous shear at the wall is zero. Beyond this point the viscous shear becomes negative creating a low velocity recirculation zone behind the indentation called an eddy.

The reverse flowing fluid pushes the boundary layer away from the wall creating the separation zone. Once the eddy destabilises the recirculation zone dampens out and reattachment of the boundary layer occurs.

However if the successive indentation occurs prior to the boundary layer reattaching, interference of the flow occurs in the separation region. This prevents reattachment from occurring and pushes the higher velocity fluid further away from the wall over a longer distance.

Once the fluid flow stabilises again, the higher velocity fluid moves back towards the wall as shown in Figure 52. However, the high velocity fluid will be pushed

away from the wall again once the low velocity boundary layer thickens as per Figure 51. This pulse like flow continues down the length of the spiral tube.

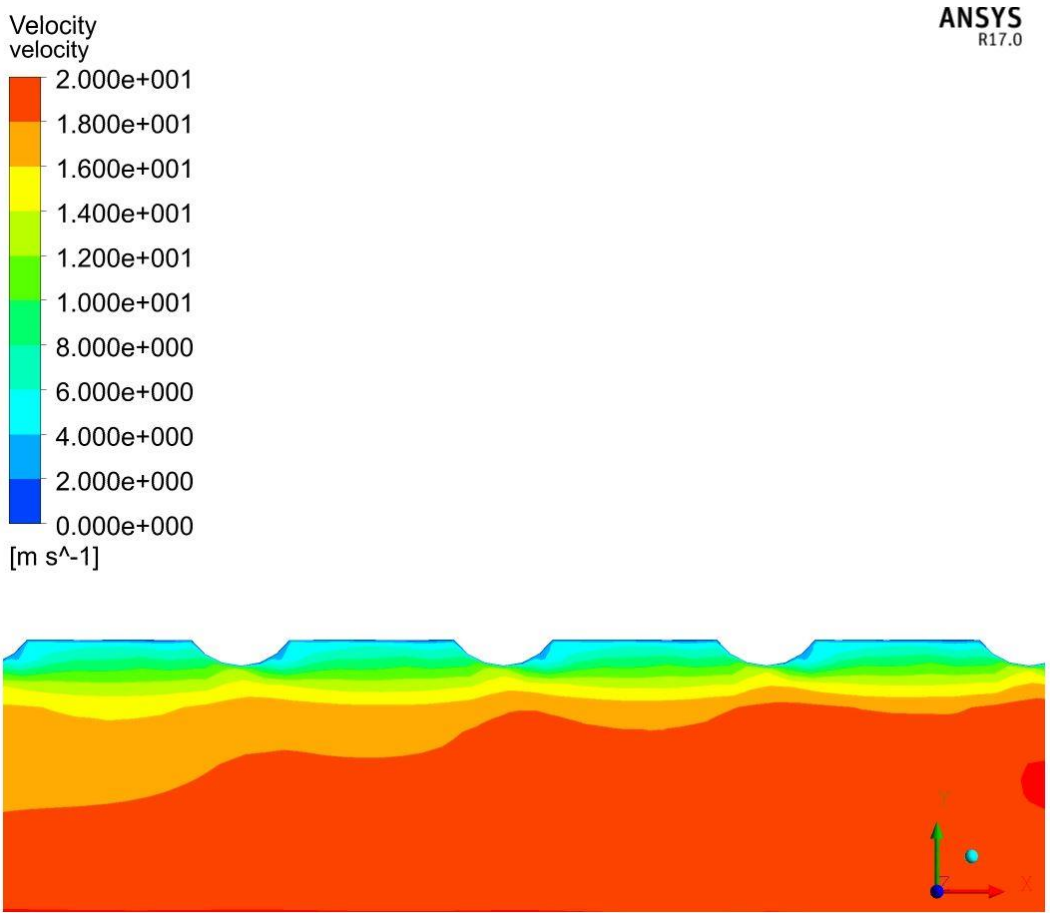

Figure 52: Velocity contour at wall at end of pulse for test point 5 for Model B – increased spiral pitch

The other factor, which may seem insignificant, that improves the heat transfer rate is the surface area. The surface area of the spiral indentation increases by 1.5 times when the pitch is decreased from 25 to 20 mm as shown in Table 16. This increase in surface area will also improve the heat transfer rate.

Table 16: Spiral heat transfer surface area

Model	p mm	N	A m^2
Current	25	119	0.082
B	20	151	0.123

5.2.3. Conclusion

Increasing the spiral depth significantly increases the heat transfer rate and pressure drop across the tube length. This is due to the increased indentation depth disrupting the fluid flow close to the wall and also by promoting secondary swirl flow which initialises turbulence inside the tube.

Decreasing the pitch, on the other hand, causes interference of the separation regions between the indentations resulting in a pulse like flow down the length of the spiral tube.

Therefore it can be concluded that both geometrical parameters have an influence on the fluid flow and can be changed and used to improve the heat transfer rate of the spiral corrugated tube.

5.3. Effects of change of spiral pitch and depth simultaneously

To determine what effect a change in both the spiral pitch and depth has on the heat transfer rate and pressure drop, model C is run. The two spiral characteristics are changed as per Table 17 below.

Table 17: Spiral characteristics of current, A, B and C models

Model	p mm	e mm
Current	25	2.0
A	25	2.8
B	20	2.0
C	22	2.4

Due to the drastic increase in pressure drop seen for model A, the spiral depth is increased by fifty percent less for model C. For model B no significant heat transfer rate was obtained by reducing the pitch by a 20 %, therefore for model C the pitch is only reduced to 22 mm instead of 20 mm as was done for model B.

All mesh and solver settings from Section 4 are used for model C and additional changes are found in Appendix C.

5.3.1. Y+ value

The average y^+ value at the wall is calculated at test point 5 and 7 and tabulated in Table 18. These are the two test points with the minimum and maximum inlet velocity conditions. Once again the y^+ values approach one for both test points, as is required for the enhanced wall treatment model for accurate results. It can therefore be assumed that the y^+ values for the remaining 10 test points are also within the required range.

Table 18: Average y+ values at the wall

Model	Test point	u_{in} m/s	y^+
C	5	12.2	0.8
	7	20.3	1.2

5.3.2. Results

The pressure drop and LMTD Nusselt number are plotted against the LMTD Reynolds number for the current, A, B and C models in Figure 53 and 54. It can be seen that the results obtained for model C fall between those obtained for models A and B.

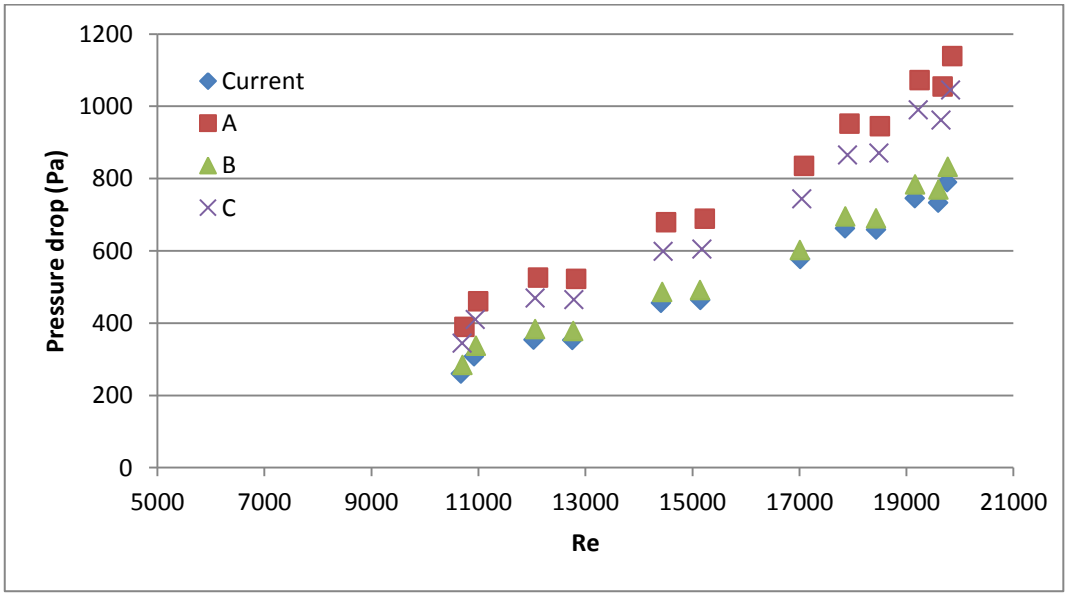

Figure 53: Pressure drop versus Reynolds number for current, A, B and C models

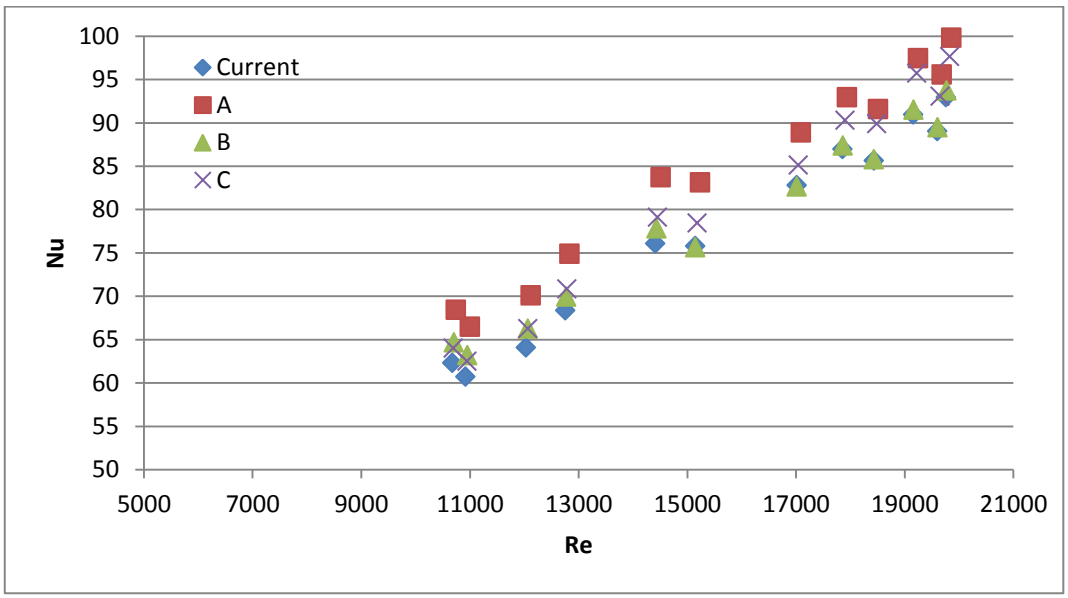

Figure 54: Nusselt number versus Reynolds number for current, A, B and C models

From the average relative deviation in pressure and temperature it is seen in Table 19 that the heat transfer rate improvement for model C is greater than for model B and the pressure drop is less than that obtained from model A.

Table 19: Relative deviation on pressure and temperature for models A, B & C

Model	p mm	e mm	ξ_P %	ξ_T %
Current	25	2.0	-	-
A	25	2.8	31.7	1.4
B	20	2.0	5.9	0.3
C	22	2.4	24.0	0.7

To determine what effects the change of the spiral pitch and depth has on the flow characteristics the velocity contours are plotted at 1400 mm from the inlet boundary for test point 5 in Figure 55.

It is seen that the pulse like flow discussed in Section 5.2.2.2 is present. It is dominant for around 53 % of the tube length for model C, whereas it was only dominant for around 40 % for model B. This shows that the pitch/depth combination of model C increases the effect the upstream indentation has on the fluid flow over the downstream indentation.

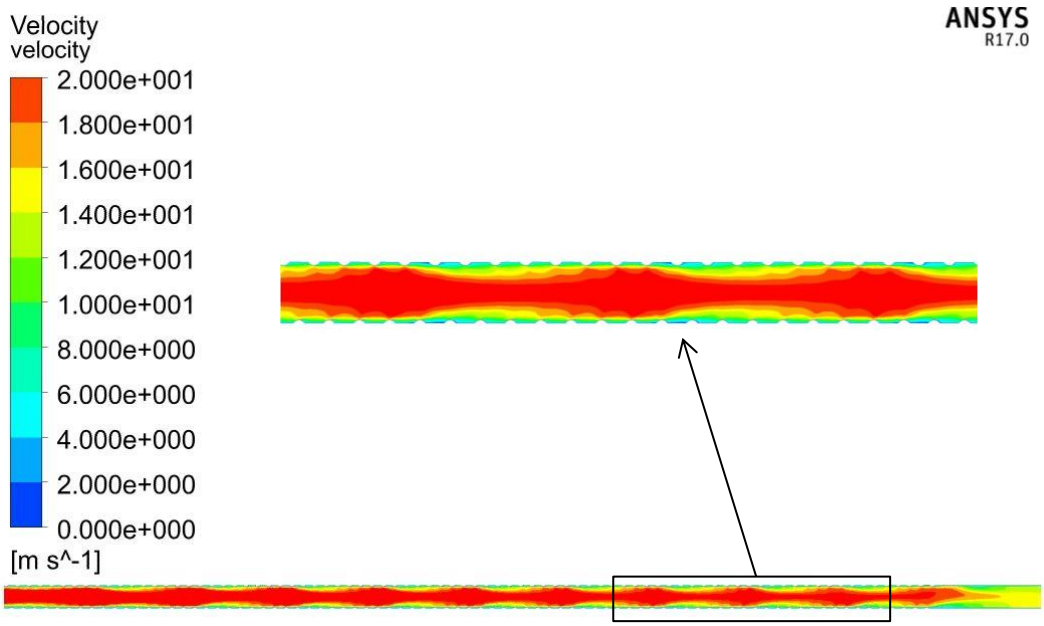

Figure 55: Velocity contours for test point 5 for Model C

The velocity contours are now plotted for test point 7, with an inlet velocity of 12.2 m/s, at 1400 mm from the inlet boundary in Figure 56. No pulse flow is seen and only a slight secondary swirl flow is present. This pulsing flow is therefore only dominant at the higher inlet velocity conditions.

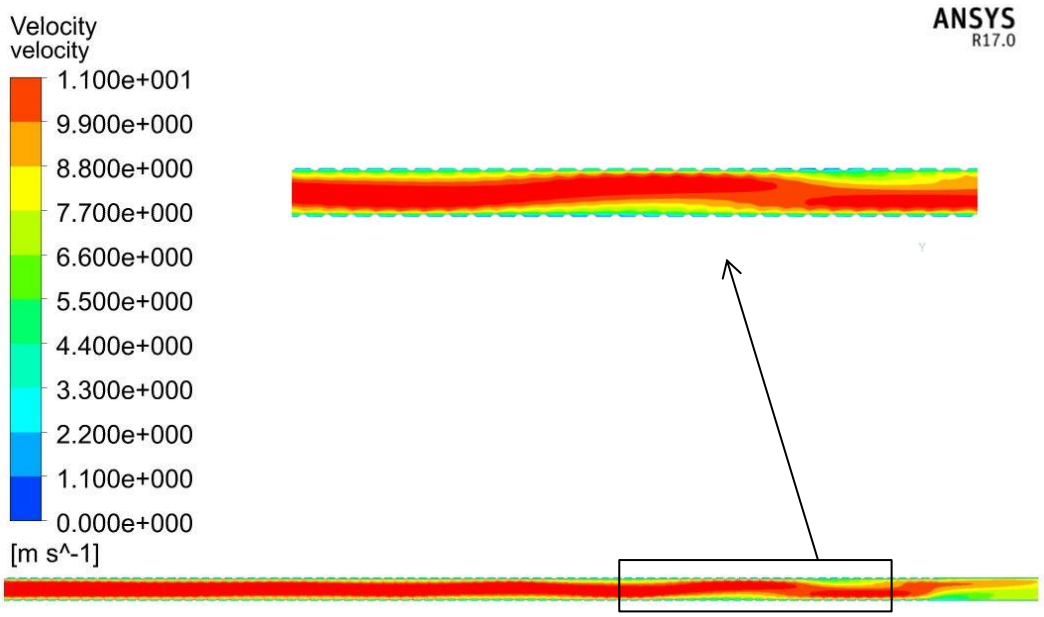

Figure 56: Velocity contours for test point 7 for Model C

The pressure contours over the first corrugation at 180 mm from the inlet boundary condition are plotted for the current, A, B and C models in Figure 57.

Here it can clearly be seen that model B results in the highest pressure drop over the corrugation.

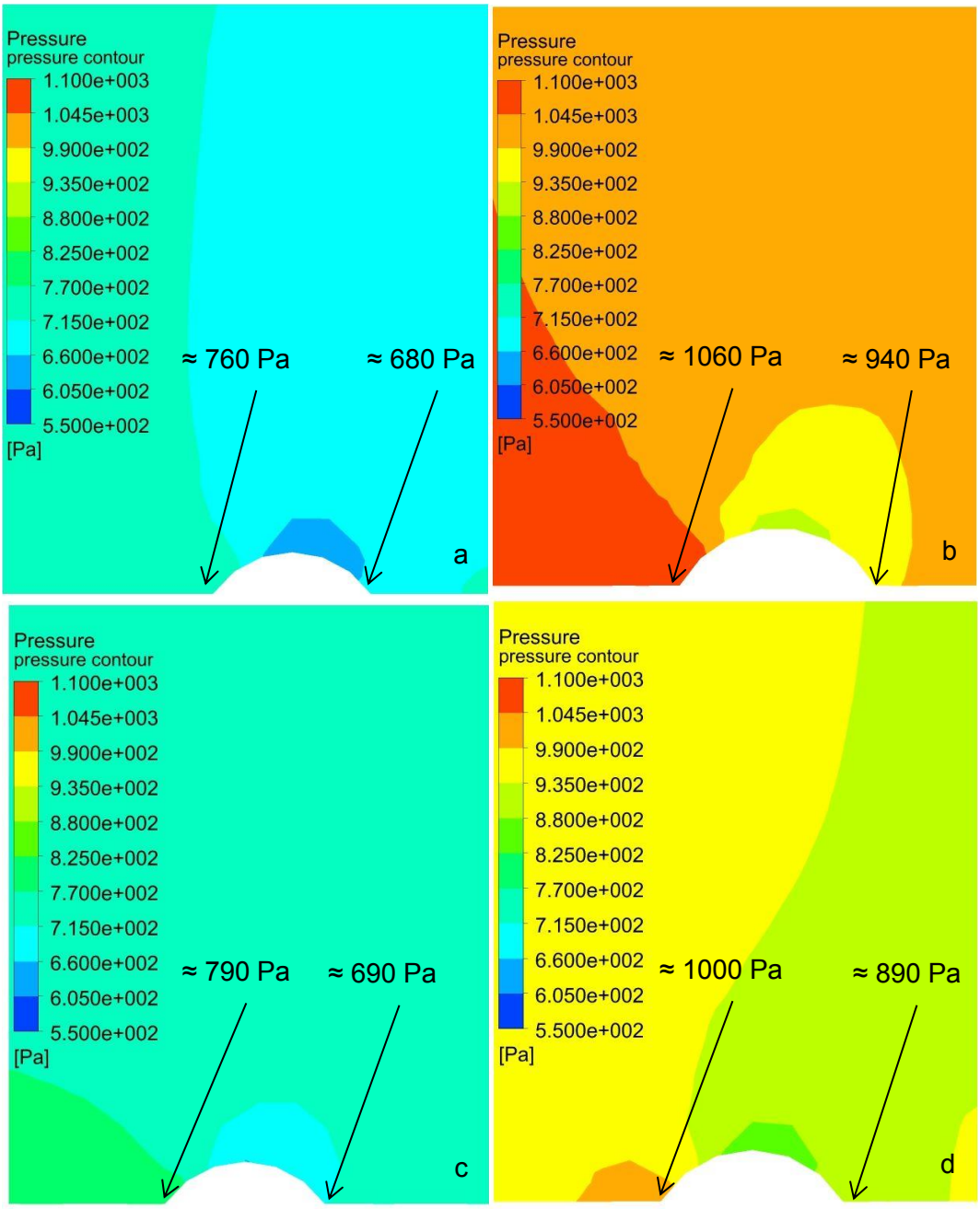

Figure 57: a – Pressure contours for current model. b – Pressure contours for model A. c – Pressure contours for model B. d – Pressure contours for model C.

5.3.3. Conclusion

Decreasing the pitch and increasing the depth of the spiral corrugation promotes the flow to have a pulse like action. This is due to the fact that when the indentations are deep enough and close enough to one another they influence the flow around the downstream adjacent indentations.

This interference disrupts the flow and prevents reattachment occurring and thereby increases the separation region. Once the flow stabilises again the high velocity fluid moves back towards the wall and reattachment occurs.

This interference is however also dependent on the velocity of the fluid. If the core fluid velocity is not high enough the fluid close to the wall remains stable and flows over the indentations. Therefore no flow disruptions occur and reattachment of the flow occurs after each indentation prior to the next downstream indentation.

This leads to the conclusion that at the right combination of the spiral pitch and depth, at a high enough fluid velocity, the pulse like flow is promoted. This pulse like flow increases the heat transfer rate and the pressure drop over the tube length.

5.4. Spiral pitch-to-depth ratio

The spiral pitch-to-depth ratio, $\left(\frac{p}{e}\right)$, is varied to determine what effect it has on the heat transfer rate and pressure drop across the tube length. The spiral pitch is kept constant and the spiral depth is varied to achieve a range of spiral pitch-to-depth ratios.

As discussed in Chapter 2, Kathait and Patil (2014) concluded that both the friction factor and Nusselt number increased at ratios below 10. Ratios greater than 14 resulted in a gradual decrease in both values. It is therefore decided to investigate this range of ratios.

Three inlet boundary conditions are investigated namely test points 7, 3 and 5 as per Table 20. These are the test points with the lowest, average and highest inlet velocity conditions. Nine models are simulated with geometrical parameters as per Table 21. Additional settings can be found in Appendix D.

Table 20: Test points inlet conditions

Test point	u_{in} m/s	T_{in} K
3	16.4	675
5	20.3	639
7	12.2	682

Table 21: Geometrical parameters for various pitch-to-depth ratios

Model	p mm	e mm	$\left(\frac{p}{e}\right)$
H	25	3.2	7.8
A	25	2.8	8.9
G	25	2.4	10.4
J	25	2.2	11.4
Current	25	2.0	12.5
I	25	1.9	13.2
E	25	1.8	13.9
D	25	1.6	15.6
F	25	1.4	17.9

5.4.1. Results

The pressure drop is plotted against the pitch-to-depth ratio for the three test points in Figure 58.

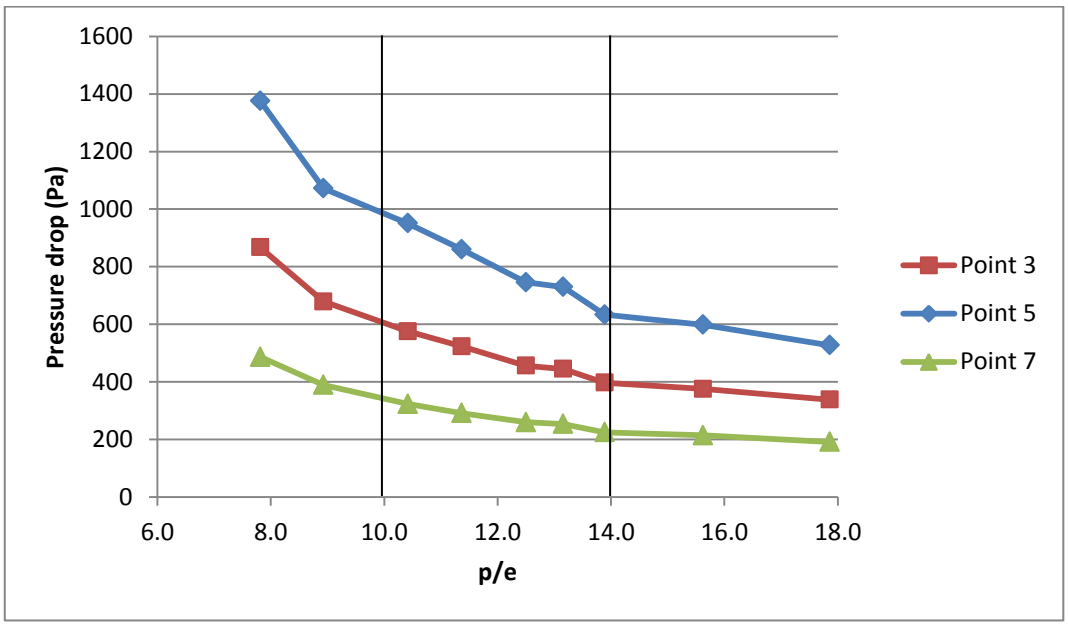

Figure 58: Pressure drop versus p/e for test points 3, 5 and 7

From the graph it is seen that as the indentation depth increases so the pressure drop increases. This is due to the fact that the greater the protrusion depth, the more it disrupts the flow of the fluid through the tube by breaking up the boundary layer and increasing the drag over the indentations.

At pitch-to-depth ratios smaller than 10 the pressure drop increases exponentially as the ratio decreases. At ratios greater than 14 the pressure drop gradually decreases as the ratio increases.

The LMTD Nusselt number is plotted against the pitch-to-depth ratio in Figure 59 for the three test points.

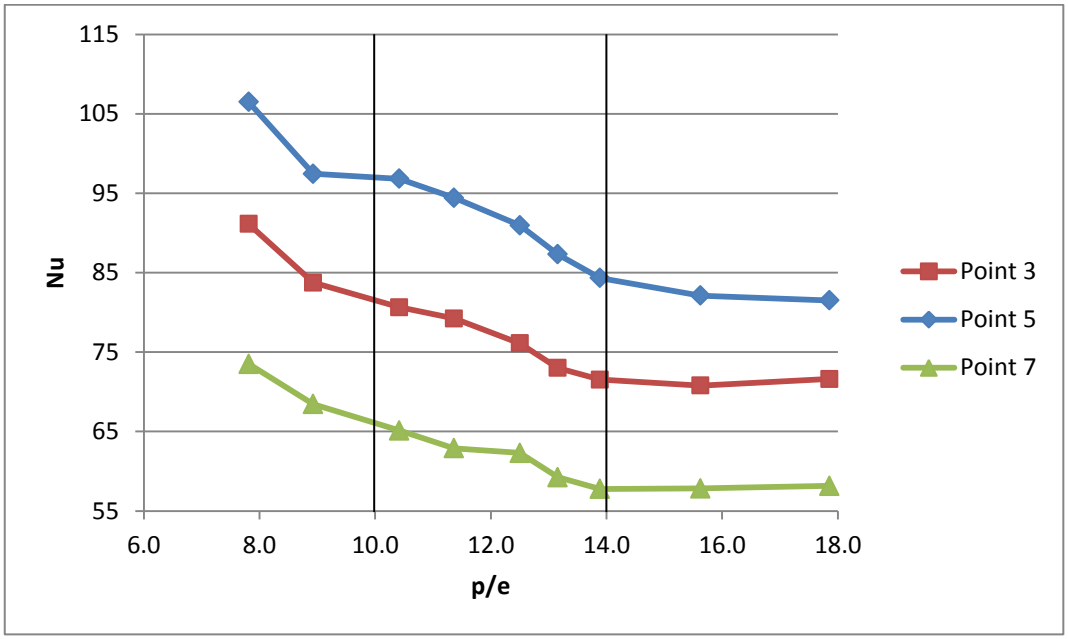

Figure 59: Nusselt number versus p/e for test points 3, 5 and 7

Similar results are seen for the Nusselt number as is observed for the pressure drop where the Nusselt number increases as the spiral depth increases. The Nusselt number is greatly affected at ratios below 10 but at ratios above 14 the effect is less apparent.

This phenomenon is observed for all three inlet velocity conditions for the Nusselt number and pressure drop.

By changing the spiral depth of the current spiral tube to obtain a pitch-to-depth ratio of 10, the heat transfer rate and pressure drop is increased as per Table 22. The actual pressure drop increases by an average of 129 Pa and the outlet temperature reduces by an average of 4.0 °C for the three test points.

Table 22: Relative deviation on pressure and temperature for model G

Model	p mm	e mm	$\left(\frac{p}{e}\right)$	ξP %	ξT %
G	25	2.4	10.4	20.7	1.0

5.4.2. Conclusion

The spiral pitch-to-depth ratio can be used to determine what the spiral depth should be for a specific pitch which will allow for an improved heat transfer at an acceptable increased pressure drop. This will prevent an excessive increase in the pressure drop.

The optimal range for the pitch-to-depth ratio is equal to or greater than 10 but smaller than 14. By ensuring it is not less than 10 will prevent an excessive increase in the pressure drop.

It is recommended that the spiral depth of the current spiral tube be increased to 2.4 mm to achieve a spiral pitch-to-depth ratio of 10. This should improve the heat transfer rate at an acceptable increased pressure drop. Future work should include the actual testing of the adjusted spiral corrugated tube to determine if the change does actually improved the heat transfer rate in an operational boiler.

5.5. Conclusion

The effect of the spiral pitch and depth on the heat transfer rate and pressure drop was investigated. It was found that when the spiral depth was increased to 2.8 mm, the pressure drop increased significantly by 31.7 % while the heat transfer rate increased by 1.4 %.

It was found that secondary swirl flow was promoted with the increased spiral depth and this was the main contributing factor to the increased pressure drop and heat transfer rate.

The secondary swirl promotes turbulence and thereby disrupts the fluid flow close to the wall, thinning the boundary layer. This allows higher temperature fluid closer to the wall and thereby increases the heat transfer rate.

More turbulence however increases the pressure drop across the tube length as the drag over the indentations is increased.

When the spiral pitch was decreased to 20 mm the pressure drop increased by 5.9 % and the heat transfer rate by 0.3 %. It was found that instead of a dominant secondary swirl flow as was seen with the increased spiral depth, the decreased spiral pitch promoted a pulse like flow.

This pulse like flow is caused by the interference of the upstream indentation on the flow over the downstream indentations. As the fluid passes over the indentation it separates from the wall and a recirculation zone is generated downstream of the indentation. This recirculation zone eventually disappears again as the fluid flow stabilises and reattachment occurs.

If the downstream indentation occurs within the area where reattachment hasn't occurred yet, the separation zone is increased. The high velocity fluid is pushed further away from the wall as the fluid passes over the next indentation.

This disrupted flow continues down the length of the tube until the fluid eventually stabilises again and reattachment occurs. This increased length of the separation and reattachment zone results in the pulse like flow.

When the spiral pitch is decreased to 22 mm and the spiral depth is increased to 2.4 mm, the heat transfer rate is increased by 0.7 % and the pressure drop by 24.0 %.

These results fall in between those obtained from increasing the spiral depth only and decreasing the spiral pitch only.

The fluid flow pattern in this scenario displays again the pulse like flow seen when only the spiral pitch was decreased. This leads to the conclusion that at the right combination of spiral depth and pitch the pulse like flow is promoted. The depth of the corrugations and the proximity to one another ensures that interference is caused by the upstream indentation on the flow over the downstream indentations.

It is noted however that this pulse like flow is also dependent on the velocity of the fluid. At lower velocities the fluid over the upstream indentation stabilises and reattaches before it reaches the downstream indentation and thereby no pulse like flow is created.

It can therefore be concluded that the change of the spiral depth and pitch have an effect on the fluid flow through the spiral tube. A decreased spiral pitch and an increased spiral depth both increase the pressure drop over the spiral tube length and improve the heat transfer rate of the convective tube.

The effect the spiral pitch-to-depth ratio has on the heat transfer rate and pressure drop is investigated. It is found that at a ratio of less than 10, both variables increase exponentially as the ratio decreases and at a ratio greater than 14 both variables decrease gradually as the ratio increases.

It is concluded that the spiral pitch-to-depth ratio can be used to determine the spiral depth at a specific pitch to improve the heat transfer rate at an acceptable increase in pressure drop across the tube length. It is therefore recommended that for the current spiral pitch of 25 mm the spiral depth is increased to 2.4 mm to achieve a spiral pitch-to-depth ratio of 10.

6. Conclusion

The single start spiral heat transfer enhancement technique was investigated on a boiler convective tube. The empirical correlations for the friction coefficient and Nusselt number for the spiral corrugated convective tube were validated against test results by du Toit (2002). It was found by du Toit (2002) that the results obtained correlated fairly accurately for the pressure drop while a correction factor was required for the Nusselt number in order to obtain accurate results from the empirical calculations.

This correction factor however was assumed to be valid for all Reynolds numbers across the total temperature range of the combustion gas inside the boiler.

An empirical comparison was done to compare the heat transfer rate and pressure drop obtained from a plain and a spiral corrugated tube. It was found that the heat transfer enhancement technique improved the heat transfer rate by an average of 104 % however it also significantly increased the pressure drop by an average of 270 %.

It is concluded that the addition of the single start spiral corrugation to the convective tube is a feasible option as a heat transfer enhancement technique. A more accurate means however is required to predict the heat transfer rate without the use of a correction factor.

This is achieved by simulating a CFD model of the spiral corrugated convective tube. To ensure that the CFD model yields accurate results a CFD model validation is done. When comparing the CFD results and the experimental results an average relative deviation of 8.5 % is achieved for pressure, 6.0 % for the Nusselt number and 0.3 % for the outlet gas temperature.

The average relative deviation for pressure improves compared to the relative deviation of 10.3 % attained between the empirical correlation and the experimental results. The average relative deviation on the Nusselt number however is fairly close to the 7.0 % obtained between the experimental results and the empirical correlation including the correction factor.

It is concluded that the CFD model is validated and can be used to predict the heat transfer rate without the use of a correction factor.

The flow characteristics of the CFD model are investigated. It is observed that the higher the inlet velocity, the thinner the boundary layer at the wall and the greater the pressure drag over the indentations becomes. These two observations result in an increased heat transfer rate and pressure drop at higher inlet velocity flows.

These observations correlate to the theory of turbulent flow and therefore it can be said that the flow characteristics observed in the CFD simulations reflect fairly accurately the actual flow patterns expected inside a spiral corrugated convective tube.

The validated CFD model is used to investigate what effect the change in the geometrical parameters of the spiral corrugation will have on the heat transfer rate and pressure drop.

The spiral depth is increased to 2.8 mm and it is found that the heat transfer rate increases by an average of 1.4 % while the pressure drop significantly increases by an average of 31.7 %.

This is due to the increased indentation depth disrupting the fluid flow close to the wall and initialising a secondary swirl flow. The secondary swirl flow promotes turbulence inside the tube thereby thinning the boundary layer close to the wall and increasing the pressure drag over the indentations. The secondary swirl flow is therefore the main contributing factor to the increased pressure drop and heat transfer rate found at the increased spiral depth.

The spiral pitch is decreased to 20 mm and an average increase in the pressure drop of 5.9 % and an average increase in the heat transfer rate of 0.3 % is achieved.

It is found that instead of a dominant secondary swirl flow as is seen with the increased spiral depth, the decreased spiral pitch initiates a pulse like flow. This pulse like flow is caused by interference of the upstream indentation on the fluid flow over the downstream indentations.

As the fluid flows over an indentation it separates from the wall forming a recirculation zone behind the indentation. The recirculation zone eventually dampens out again as the fluid flow stabilises and reattachment of the fluid boundary layer occurs.

When the downstream indentation is close enough to the upstream indentation and it occurs within the region where reattachment hasn't happened yet, the separation zone is increased.

The higher velocity fluid that was pushed away from the wall at the separation point by the reverse flow fluid downstream of the first indentation is pushed further away from the wall at the second indentation. This increasing separation zone will continue down the length of the convective tube until the recirculation zone becomes unstable and dampens out again, resulting in reattachment of the fluid boundary layer.

This disrupted flow of increased length of the separation and reattachment zone continues down the length of the spiral corrugated convective tube and results in the pulse like flow.

It is concluded that a change in either of the two geometrical parameters will have an effect on the fluid flow and thereby increase the heat transfer rate and pressure drop.

To determine what effect changing both geometrical parameters will have on the flow the spiral depth is increased to 2.4 mm and the spiral pitch is decreased to

22 mm. It is found that the average heat transfer rate is increased by 0.7 % and average pressure drop by 24.0 %. These results fall in between those obtained when only the spiral pitch was decreased and only the spiral depth was increased.

At this combination of spiral pitch and depth, a pulse like flow is obtained again. It is also noted that the pulse like flow is only present when the velocity of the fluid is high enough. At lower velocities the recirculation zones decrease in size and therefore reattachment occurs prior to the downstream indentation.

It is therefore deduced that at the right combination of spiral pitch, depth and fluid velocity, a pulse like flow will be promoted. This pulse like flow increases the heat transfer rate and pressure drop over the length of the spiral corrugated convective tube.

This leads to the conclusion that by changing either of the geometric parameters of the spiral corrugation or both simultaneously can have a significant effect on improving the thermal efficiency of a firetube boiler.

The geometric parameters however have a greater effect on the pressure drop over the tube length than on the heat transfer rate. It is therefore important that when the parameters are changed, the improvement in the thermal efficiency must be compared to the increased pressure drop obtained and thereby the feasibility should be investigated.

The spiral pitch-to-depth ratio is investigated and it is found that the pressure drop and Nusselt number increases drastically as the ratio decreases below 10. As the ratio increases beyond 14, the pressure drop and Nusselt number decreases gradually.

This leads to the conclusion that the spiral pitch-to-depth ratio can be used to determine the spiral depth at a specific pitch to allow improvement on the heat transfer rate but at an acceptable increase in pressure drop across the tube length.

It is therefore recommended that the spiral depth of the current spiral tube be increased to 2.4 mm to achieve a spiral pitch-to-depth ratio of 10. This will improve the heat transfer rate by an average of 1.0 % at an acceptable increased pressure drop at an average of 20.7 %. The adjusted spiral corrugated tube should be tested at a later stage to determine if a pitch-to-depth ratio of 10 is actually beneficial in an operational boiler.

For future work, a new equation can be found from the CFD simulations for the Nusselt number for a spiral corrugated tube. This will then replace the current Nusselt number correlation and eliminate the need for the correction factor.

The CFD model of the spiral corrugated convective tube can be remodelled using combustion air as the fluid and be incorporated into a model of the whole boiler. This will allow comparisons to be done to boilers in the field and allow design

refinements to be done in other areas of the boiler without having to do actual testing on site prior to design improvement implementation.

Appendix A: Fluent settings for Section 4: CFD model validation

A1. Geometry

Table A1: Geometry of spiral corrugated tube

Property	*Dimensions*	*Symbol*	*Value*
Tube length	mm	L	3394.6
Spiral length	mm		3022.6
Straight inlet length	mm		172
Straight outlet length	mm		200
Spiral pitch	mm	p	25.4
Spiral depth	mm	e	1.97
Spiral turns		N	119
Tube inside diameter	mm	d	44.3
Mean diameter of spiral	mm	d_m	49.4
Inner core diameter	mm		28
Outer core diameter	mm		34
Spiral diameter	mm		9.04
Number of bodies/domains			12

The geometry of the spiral corrugated tube is as per Table A1 and is setup in Design Modeller.

Table A2: Names of spiral tube geometry bodies

Domain	Name
1	Spiral-section
2	Non-spiral-section
3	Inlet-straight
4	Inlet-ring
5	Inlet-internal
6	Outlet-straight
7	Outlet-ring
8	Outlet-internal
9	Internal
10	Inlet-tet
11	Outlet-tet
12	Internal-ring

The part consists of 12 bodies that are labelled as per Table A2.

A2. Mesh

Table A3: Mesh A - method and inflation layer

Body	Name	Mesh method	Inflation layer
1	Spiral-section	Sweep	First layer – 0.06 mm
2	Non-spiral-section	Sweep	First layer – 0.06 mm
3	Inlet-straight	Body sizing – 1.5 mm Sweep	First layer – 0.06 mm
4	Inlet-ring	Sweep	-
5	Inlet-internal	Sweep	-
6	Outlet-straight	Body sizing – 1.5 mm Sweep	First layer – 0.06 mm
7	Outlet-ring	Sweep	-
8	Outlet-internal	Sweep	-
9	Internal	Body sizing – 1.5 mm Sweep	-
10	Inlet-tet	Patch conforming - tet	First layer – 0.06 mm
11	Outlet-tet	Patch conforming - tet	First layer – 0.06 mm
12	Internal-ring	Patch conforming - tet	-

The 12 bodies are meshed according to Table A3. Mesh A contains 5 471 249 elements.

For the mesh independent study the mesh setting as changed as per Table A4. A mesh size of 7 122 886 elements is obtained for mesh B.

Table A4: Mesh B - method and inflation layer

Body	Name	Mesh method	Inflation layer
1	Spiral-section	Sweep	First layer – 0.06 mm
2	Non-spiral-section	Sweep	First layer – 0.06 mm
3	Inlet-straight	Body sizing – 1.3 mm Sweep	First layer – 0.06 mm
4	Inlet-ring	Sweep	-
5	Inlet-internal	Sweep	-
6	Outlet-straight	Body sizing – 1.3 mm Sweep	First layer – 0.06 mm
7	Outlet-ring	Sweep	-
8	Outlet-internal	Sweep	-
9	Internal	Body sizing – 1.3 mm Sweep	-
10	Inlet-tet	Patch conforming - tet	First layer – 0.06 mm
11	Outlet-tet	Patch conforming - tet	First layer – 0.06 mm
12	Internal-ring	Patch conforming - tet	-

A3. Boundary types

Table A5: Boundaries of domains

Domain	Name	Boundary with domain	Type
1	Spiral-section	10	Interface
		11	Interface
		12	Interface
		2	Interface
		Exterior	Wall
2	Non-spiral-section	10	Interface
		11	Interface
		12	Interface
		1	Interface
		Exterior	Wall
3	Inlet-straight	4	Interface
		10	Interface
		Exterior	Wall
		Exterior	Inlet Velocity
4	Inlet-ring	3	Interface
		5	Interface
		12	Interface
		Exterior	Inlet Velocity
5	Inlet-internal	4	Interface
		9	Interface
		Exterior	Inlet Velocity
6	Outlet-straight	7	Interface
		11	Interface
		Exterior	Wall
		Exterior	Pressure Outlet
7	Outlet-ring	6	Interface
		8	Interface
		12	Interface
		Exterior	Pressure Outlet
8	Outlet-internal	7	Interface
		9	Interface
		Exterior	Pressure Outlet

Table A5 continued

Domain	Name	Boundary with domain	Type
9	Internal	5	Interface
		8	Interface
		12	Interface
10	Inlet-tet	3	Interface
		12	Interface
		2	Interface
		1	Interface
		Exterior	Wall
11	Outlet-tet	6	Interface
		12	Interface
		2	Interface
		1	Interface
		Exterior	Wall
12	Internal-ring	4	Interface
		7	Interface
		10	Interface
		11	Interface
		9	Interface
		2	Interface
		1	Interface

All domain boundaries are defined as per Table A5.

A4. Boundary conditions

The following boundary conditions are set in FLUENT.

Inlet

- Set velocity to u_{in} as per Table A9.
- Set turbulence specification method to “Intensity and hydraulic diameter”
- Set turbulent intensity to 5 % and hydraulic diameter to 44.3 mm
- Set temperature T_{in} as per Table A9.

Outlet

- Set turbulence specification method to “Intensity and hydraulic diameter”
- Set turbulent intensity to 5 % and hydraulic diameter to 44.3 mm

Wall

- Set thermal boundary condition to “Temperature”
- Set wall thickness to 3.25 mm
- Set wall temperature to 373 K

Table A6: Inlet and outlet flow conditions of test points for CFD validation

Test point	Inlet					Outlet		
	u_{in} m/s	T_{in} K	Re_{in}	x	I_{in} %	U_{out} m/s	Re_{out}	I_{out} %
1	14.6	764	8783	$6d$	5	7.9	13229	5
2	15.2	733	9818	$6d$	5	8.6	14409	5
3	16.4	675	12097	$7d$	5	9.9	16861	5
4	19.3	649	15207	$7d$	5	12.2	20615	5
5	20.3	639	16411	$7d$	5	13.0	22018	5
6	20.9	638	16948	$7d$	5	13.5	22679	5
7	12.2	682	8867	$6d$	5	7.2	12567	5
8	13.9	656	10756	$6d$	5	8.6	14830	5
9	15.7	631	12967	$7d$	5	10.0	17451	5
10	17.4	624	14636	$7d$	5	11.3	19519	5
11	18.4	613	15959	$7d$	5	12.2	21032	5
12	19.3	606	17042	$7d$	5	12.9	22289	5

A5. Materials

Set the fluid material to air and the solid material to P235GH with properties as per Tables A7, A8 and A9.

Table A7: Properties of air

Property	Symbol	Type
Density	ρ	Incompressible ideal gas
Specific heat	cp	Piecewise polynomial
Thermal conductivity	k_t	Piecewise linear (See table A6)
Viscosity	μ	Power-law

Table A8: Thermal conductivity of air

T		k_{air}
K	°C	W/m.K
373	100	0.03095
393	120	0.03235
413	140	0.03374
433	160	0.03511
453	180	0.03646
473	200	0.03779
523	250	0.04104
573	300	0.04418
623	350	0.04721
673	400	0.05015
773	500	0.05572
873	600	0.06093

Table A9: Properties of P235GH

Property	Symbol	Value
Density	ρ	7850
Specific heat	cp	479
Thermal conductivity	k_t	479

A6. Control parameters

- Enable gravity and set y: - 9.81 m/s^2
- Enable energy equation
- Set viscous model to “k-epsilon” and “realizable”
- Select “enhanced wall treatment”
- Activate full buoyancy effects
- Set spatial discretization scheme to “Second order upwind” for turbulent kinetic energy and turbulent dissipation rate

Appendix B: Fluent settings for Section 5.2: Effects of change of spiral pitch and depth individually

B1. Geometry

Table B1: Geometry of Model A spiral corrugated tube

Property	*Dimensions*	*Symbol*	*Value*
Tube length	mm	L	3394.6
Spiral length	mm		3022.6
Straight inlet length	mm		172
Straight outlet length	mm		200
Spiral pitch	mm	p	25.4
Spiral depth	mm	e	2.8
Spiral turns		N	119
Tube inside diameter	mm	d	44.3
Mean diameter of spiral	mm	d_m	49.4
Inner core diameter	mm		28
Outer core diameter	mm		34
Spiral diameter	mm		10.7
Number of bodies/domains			12

The geometry of the spiral corrugated tube Model A is as per Table B1 and is setup in Design Modeller.

Table B2: Geometry of Model B spiral corrugated tube

Property	*Dimensions*	*Symbol*	*Value*
Tube length	mm	L	3395
Spiral length	mm		3020
Straight inlet length	mm		172
Straight outlet length	mm		203
Spiral pitch	mm	p	20.0
Spiral depth	mm	e	1.97
Spiral turns		N	151
Tube inside diameter	mm	d	44.3
Mean diameter of spiral	mm	d_m	49.4
Inner core diameter	mm		28
Outer core diameter	mm		34
Spiral diameter	mm		9.04
Number of bodies/domains			12

The geometry of the spiral corrugated tube Model B is as per Table B2 and is setup in Design Modeller.

All additional settings are as per Appendix A. A mesh size of 5 311 249 for Model A and 5 823 469 for Model B is obtained.

Appendix C: Fluent settings for Section 5.3: Effects of change of spiral pitch and depth simultaneously

Table C1: Geometry of Model C spiral corrugated tube

Property	*Dimensions*	*Symbol*	*Value*
Tube length	mm	L	3395
Spiral length	mm		3014
Straight inlet length	mm		172
Straight outlet length	mm		209
Spiral pitch	mm	p	22.0
Spiral depth	mm	e	2.4
Spiral turns		N	137
Tube inside diameter	mm	d	44.3
Mean diameter of spiral	mm	d_m	49.4
Inner core diameter	mm		28
Outer core diameter	mm		34
Spiral diameter	mm		9.9
Number of bodies/domains			12

The geometry of the spiral corrugated tube Model C is as per Table C1 and is setup in Design Modeller.

Additional settings are as per Appendix A and a mesh size of 5 508 959 elements is achieved.

Appendix D: Fluent settings for Section 5.4: Spiral pitch-to-depth ratio

Table D1: Geometry of Model D spiral corrugated tube

Property	*Dimensions*	*Symbol*	*Value*
Tube length	mm	L	3394.6
Spiral length	mm		3022.6
Straight inlet length	mm		172
Straight outlet length	mm		200
Spiral pitch	mm	p	25.4
Spiral depth	mm	e	1.6
Spiral turns		N	119
Tube inside diameter	mm	d	44.3
Mean diameter of spiral	mm	d_m	49.4
Inner core diameter	mm		28
Outer core diameter	mm		34
Spiral diameter	mm		8.3
Number of bodies/domains			12

The geometry of the spiral corrugated tube Model D is as per Table D1 and is setup in Design Modeller.

Additional settings are as per Appendix A and a mesh size of 5 880 172 elements is achieved.

Table D2: Geometry of Model E spiral corrugated tube

Property	*Dimensions*	*Symbol*	*Value*
Tube length	mm	L	3394.6
Spiral length	mm		3022.6
Straight inlet length	mm		172
Straight outlet length	mm		200
Spiral pitch	mm	p	25.4
Spiral depth	mm	e	1.8
Spiral turns		N	119
Tube inside diameter	mm	d	44.3
Mean diameter of spiral	mm	d_m	49.4
Inner core diameter	mm		28
Outer core diameter	mm		34
Spiral diameter	mm		8.7
Number of bodies/domains			12

The geometry of the spiral corrugated tube Model E is as per Table D2 and is setup in Design Modeller.

Additional settings are as per Appendix A and a mesh size of 5 716 319 elements is achieved.

Table D3: Geometry of Model F spiral corrugated tube

Property	*Dimensions*	*Symbol*	*Value*
Tube length	mm	L	3394.6
Spiral length	mm		3022.6
Straight inlet length	mm		172
Straight outlet length	mm		200
Spiral pitch	mm	p	25.4
Spiral depth	mm	e	1.4
Spiral turns		N	119
Tube inside diameter	mm	d	44.3
Mean diameter of spiral	mm	d_m	49.4
Inner core diameter	mm		28
Outer core diameter	mm		34
Spiral diameter	mm		7.9
Number of bodies/domains			12

The geometry of the spiral corrugated tube Model F is as per Table D3 and is setup in Design Modeller.

Additional settings are as per Appendix A and a mesh size of 5 998 707 elements is achieved.

Table D4: Geometry of Model G spiral corrugated tube

Property	Dimensions	Symbol	Value
Tube length	mm	L	3394.6
Spiral length	mm		3022.6
Straight inlet length	mm		172
Straight outlet length	mm		200
Spiral pitch	mm	p	25.4
Spiral depth	mm	e	2.4
Spiral turns		N	119
Tube inside diameter	mm	d	44.3
Mean diameter of spiral	mm	d_m	49.4
Inner core diameter	mm		28
Outer core diameter	mm		34
Spiral diameter	mm		9.9
Number of bodies/domains			12

The geometry of the spiral corrugated tube Model G is as per Table D4 and is setup in Design Modeller.

Additional settings are as per Appendix A and a mesh size of 5 265 729 elements is achieved.

Table D5: Geometry of Model H spiral corrugated tube

Property	Dimensions	Symbol	Value
Tube length	mm	L	3394.6
Spiral length	mm		3022.6
Straight inlet length	mm		172
Straight outlet length	mm		200
Spiral pitch	mm	p	25.4
Spiral depth	mm	e	3.2
Spiral turns		N	119
Tube inside diameter	mm	d	44.3
Mean diameter of spiral	mm	d_m	49.4
Inner core diameter	mm		28
Outer core diameter	mm		34
Spiral diameter	mm		11.5
Number of bodies/domains			12

The geometry of the spiral corrugated tube Model H is as per Table D5 and is setup in Design Modeller.

Additional settings are as per Appendix A and a mesh size of 4 806 417 elements is achieved.

Table D6: Geometry of Model I spiral corrugated tube

Property	*Dimensions*	*Symbol*	*Value*
Tube length	mm	L	3394.6
Spiral length	mm		3022.6
Straight inlet length	mm		172
Straight outlet length	mm		200
Spiral pitch	mm	p	25.4
Spiral depth	mm	e	1.9
Spiral turns		N	119
Tube inside diameter	mm	d	44.3
Mean diameter of spiral	mm	d_m	49.4
Inner core diameter	mm		28
Outer core diameter	mm		34
Spiral diameter	mm		8.9
Number of bodies/domains			12

The geometry of the spiral corrugated tube Model I is as per Table D6 and is setup in Design Modeller.

Additional settings are as per Appendix A and a mesh size of 5 556 603 elements is achieved.

Table D7: Geometry of Model J spiral corrugated tube

Property	*Dimensions*	*Symbol*	*Value*
Tube length	mm	L	3394.6
Spiral length	mm		3022.6
Straight inlet length	mm		172
Straight outlet length	mm		200
Spiral pitch	mm	p	25.4
Spiral depth	mm	e	2.2
Spiral turns		N	119
Tube inside diameter	mm	d	44.3
Mean diameter of spiral	mm	d_m	49.4
Inner core diameter	mm		28
Outer core diameter	mm		34
Spiral diameter	mm		9.5
Number of bodies/domains			12

The geometry of the spiral corrugated tube Model J is as per Table D7 and is setup in Design Modeller.

Additional settings are as per Appendix A and a mesh size of 5 367 841 elements is achieved.

References

Ağra, Ö., Demir, H., Atayilmaz, Ş. Ö., Kantaş, F., & Dalkiliç, A. S. 2011. *Numerical investigation of heat transfer and pressure drop in enhanced tubes*. International Communications in Heat and Mass Transfer 38: 1384-1391.

Ahsan, M. 2014. *Numerical analysis of friction factor for a fully developed turbulent flow using k-ε turbulence model with enhanced wall treatment*. Beni-Suef University Journal of Basic and Applied Sciences 3: 269-277.

Brandt, L. 2014. *The lift-up effect: The linear mechanism behind transition and turbulence in shear flows*. European Journal of Mechanics B/Fluids 47: 80-96.

Budynas, R. G., Nisbett, J. K., & Shigley, J. E. 2008. *Shigley's mechanical engineering design*. New York, McGraw-Hill: 401-402.

Çengel, Y. A. 2006. *Heat and mass transfer: A practical approach*. New York, McGraw-Hill.

Dong, Y., Huixiong, L. & Tingkuan, C. 2001. *Pressure drop, heat transfer and performance of single phase turbulent flow in spirally corrugated tubes*. Experimental Thermal and Fluid Science 24: 131-138.

Du Toit, P. 2002. *Spiral tube test rig*. Report PBD91/2002. Actom John Thompson.

Ellingsen, T., & Palm, E. 1975. *Stability of linear flow*. Physics of Fluids 18: 487.

Fluent. 2015. *Ansys Fluent Theory Guide*. Version 16.1.

Garcia, A., Solano, J.P., Vicente, P.G. & Viedma, A. 2012. *The influence of artificial roughness shape on heat transfer enhancement: Corrugated tubes, dimpled tubes and wire coils*. Applied Thermal Engineering 35: 196-201.

Han, H.-Z., Li, B.-X., Yu, B.-Y., He, Y.-R., & Li, F.-C. 2012. *Numerical study of flow and heat transfer characteristics in outward convex corrugated tubes*. International Journal of Heat and Mass Transfer 55: 7782-7802.

Ji, W., Jacobi, A.M., He, Y. & Tao, W. 2015. *Summary and evaluation on single-phase heat transfer enhancement techniques of liquid laminar and turbulent pipe flow*. International Journal of Heat and Mass Transfer 88: 735-754.

Jiménez, J. 2013. *How linear is wall-bounded turbulence?* Physics of Fluids 25, 110814.

Kathait, P.S. & Patil, A.K. 2014. *Thermo-hydraulic performance of a heat exchanger tube with discrete corrugations*. Applied Thermal Engineering 66: 162-170.

Kays, W., Crawford, M. & Weigand. 2005. *Convective heat and mass transfer*. 4th Edition. McGraw Hill International.

Kitto, J. B., & Stultz, S. C. 2005. *Steam, its generation and use*. Barberton, OH, Babcock & Wilcox. 4-16.

Landahl, M. 1975. *Wave breakdown and turbulence*. SAIM Journal on Applied Mathematics, Vol. 28, No. 4: 735-756.

Laohalertdecha, S. & Wongwises, S. 2011a. *Condensation heat transfer and flow characteristics of R-134a flowing through corrugated tubes*. International Journal of Heat and Mass Transfer 54: 2673-2682.

Laohalertdecha, S. & Wongwises, S. 2011b. *An experimental study into the evaporation heat transfer and flow characteristics of R-134a refrigerant flowing through corrugated tubes*. International Journal of Refrigeration 34: 280-291.

Latzko, H. 1921. *Heat transfer in a turbulent liquid or gas stream*. Zeitschrift für angewandte Mathematik und Mechanik Vol. 1, No. 4.

Li, Y.-X., Wu, J.-H., Wang, H., Kou, L.-P., & Tian, X.-H. 2012. *Fluid flow and heat transfer characteristics in helical tubes cooperating with spiral corrugation*. Energy Procedia: Part A. 17: 791-800.

MIT OpenCourseWare. 2006. *Course textbook introduction to fluid motions, sediment transport, and current-generated sedimentary structures earth, atmospheric, and planetary sciences, MIT Opencourseware, Chapter 4 Flow in Channels* [Online]. Available: https://ocw.mit.edu/courses/earth-atmospheric-and-planetary-sciences/12-090-introduction-to-fluid-motions-sediment-transport-and-current-generated-sedimentary-structures-fall-2006/course-textbook/ch4.pdf. [2016, November 17].

Mohammed, H., Abbas, A. K., & Sheriff, J. 2013. *Influence of geometrical parameters and forced convective heat transfer in transversely corrugated circular tubes*. International Communications in Heat and Mass Transfer 44: 116-126.

Orr, W. M. 1907. *The stability or instability of the steady motions of a perfect liquid and of a viscous liquid. Part I: A perfect liquid*. Proceedings of the Royal Irish Academy. Section A: Mathematical and Physical Sciences, Vol 27 (1907-1909). 9-68.

Pethkool, S., Eiamsa-ard, S., Kwankaomeng, S. & Promvonge, P. 2011. *Turbulence heat transfer enhancement in a heat exchanger using helically corrugated tube*. International Communications in Heat and Mass Transfer 38: 340-347.

Sharwood, N. 2016. Personal interview. 17 November, John Thompson, Bellville South.

Shih, T. H., Liou, W.W., Shabbir, A., Yang, Z., and Zhu, J. 1994. *A new k-ε eddy viscosity model for high Reynolds number turbulent flows - Model development and validation*. NASA Technical Memorandum 106721.

Trading Economics. 2016. *South Africa GDP Growth Rate* [Online]. Available: http://www.tradingeconomics.com/south-africa/gdp-growth. [2016, November 17].

Vicente, P.G., Garcia, A. & Viedma, A. 2004. *Experimental investigation on heat transfer and frictional characteristics of spirally corrugated tubes in turbulent flow at different Prandtl numbers*. International Journal of Heat and Mass Transfer 47: 671-681.

Warren, R. 2000. *Spiral tubes for use in shell boilers final report*. Report 20060. Actom John Thompson.

Zimparov, V. 2002. *Enhancement of heat transfer by a combination of a single-start spirally corrugated tubes with a twisted tape*. Experimental Thermal and Fluid Science 25: 535-546.

Zimparov, V. 2004a. *Prediction of friction factors and heat transfer coefficients for turbulent flow in corrugated tubes combined with twisted tape inserts. Part 1: friction factors*. International Journal of Heat and Mass Transfer 47: 589-599.

Zimparov, V. 2004b. *Prediction of friction factors and heat transfer coefficients for turbulent flow in corrugated tubes combined with twisted tape inserts. Part 2: heat transfer coefficients.* International Journal of Heat and Mass Transfer 47: 385-393.